UNIVERSITÀ DELLA CALABRIA

UNIVERSITA' DELLA CALABRIA

Dipartimento di Fisica

Dottorato di Ricerca in

Scienze e Tecnologie Fisiche, Chimiche e dei Materiali

CICLO

XXXIII

TITOLO TESI

Archaeometric Studies by Means of Complementary and Non-Destructive Physical Methodologies with Micrometric Resolution

Settore Scientifico Disciplinare Fis/07

Coordinatore: Ch.mo Prof. (Gabriella Cipparrone)

Firma Firma oscurata in base alle linee guida del Garante della privacy

Supervisore/Tutor: Ch.mo Prof. (Vincenzo Formoso)

Firma Firma oscurata in base alle linee guida del Garante della privacy

Co-Supervisore: Prof. (Jan Kindberg Jacobsen)

Firma Firma oscurata in base alle linee guida del Garante della privacy

Dottorando: Dott. (Andrea Smeriglio)

Firma Firma oscurata in base alle linee guida del Garante della privacy

INDEX

ABSTRACT (English)

The approach to the study of cultural heritage and archaeology find is highly interdisciplinary. The archaeometry expert has to be a multidisciplinary figure with different skills in hard sciences (physical, chemical, biological, earth sciences and engineering), humanities (art historians, philologists, curators) and technical disciplines (restorers and conservators).

Today the archaeometry expert needs a palette of non-destructive and non-invasive techniques, to improve the understanding of the manufacture, the evolution and/or degradation during the time of the archaeological find.

The aims of this thesis is to display the result of archaeometric studies performed in my PhD research, and describe the non-destructive physical methodology and the approaches used to address archaeological questions and problems.

The X-ray µCT experimental apparatus implemented at the STAR-Lab facility realized under the PON MaTeRia project, at the University of Calabria (Italy), give us a possibility to acquire several images useful to inspecting the internal morphology of an object. It is a non-destructive diagnostic method used to characterize material microstructure in three dimensions with resolution of the order of micrometer.

Artax 400 is a portable µXRF developed by Bruker for archaeometric studies. µXRF is an analytical technique for elemental characterization that provides both qualitative and quantitative information. It's a non-destructive method which does not require a specific sample preparation, and it allows to carry out investigations in situ.

These complementary and non-destructive physical methodologies were used and implemented for the investigation of different archaeological finds from different archaeological contexts. In particular, five case studies are described below:

1. The aim of this case study is to determine the materials, the production process and the technological features of three silver plated coins (two Roman denarii and one Greek statere) preserved in the “Brettii and Enotri” museum in Cosenza.
2. The aim of this case study is to understand the oxidation processes, to know the constituent material and to find hidden signs or inscriptions of two completely oxidated coins preserved in the “Brettii and Enotri” museum in Cosenza.
3. The aim of the current case study is to determine the materials and technological features of a *unicum* object and to read possible inscriptions and decorations under the superficial encrustations of a bronze plaque. Both archaeological finds have been excavated in the archaeological site of Timpone della Motta, in Francavilla Marittima (CS).
4. In this case study the chemical composition of the bronze alloy and physical technical characteristics of two bronze anthropomorphic couples as pendants (dating to the Early Iron Age) have been studied. The first, called “type B”, were discovered in the archaeological site of Pietrapaola (CS), however the second, called “type A”, . were discovered in archaeological site of Bucita-Rossano (CS).
5. The aim of this case study is to investigate the conservation status and the chemical composition of 12 Magno-Greek bronze mirrors. These prestige goods are a clear example of the high level reached by the handicraft of Magna Graecia. They are preserved in the National Archaeological Museum of Locri Epizephyrii. They were discovered in the grave of the Contrada Lucifero Necropolis and they are dated between the second half of the VI century b.C. and the first half of the IV century b.C.

ABSTRACT (Italiano)

L'approccio allo studio del patrimonio culturale e dei reperti archeologici è altamente interdisciplinare. L'archeometrista è una figura multidisciplinare con diverse competenze nelle scienze dure (fisiche, chimiche, biologiche, scienze della terra e ingegneria), scienze umane (storici dell'arte, filologi, curatori) e discipline tecniche (restauratori e conservatori).

Oggi lo scienziato della conservazione ha a disposizione una serie di tecniche non distruttive e non invasive per migliorare la comprensione sui metodi di realizzazione e sullo stato di conservazione di reperti archeologici.

Scopo di questa tesi è mostrare il risultato degli studi archeometrici condotti durante la mia ricerca di dottorato e descrivere le metodologie fisiche non distruttive e gli approcci utilizzati per affrontare quesiti archeologici.

L'apparato sperimentale a raggi X utilizzato è stato realizzato presso la struttura STAR-Lab nell'ambito del progetto PON MaTeRia, presso l'Università della Calabria (Italia). La μCT a raggi X è una tecnica di *imaging* per l'ispezione della morfologia interna di un oggetto. È un metodo diagnostico non distruttivo utilizzato per caratterizzare la microstruttura del materiale in tre dimensioni, con risoluzione dell'ordine dei micrometri.

Artax 400 è uno spettrometro μXRF portatile sviluppato dall'azienda Bruker per studi archeometrici. La μXRF è una tecnica analitica utilizzata per la caratterizzazione elementale del campione di riferimento e fornisce informazioni sia qualitative che quantitative. È un metodo non distruttivo che non richiede una preparazione specifica del campione e permette di effettuare indagini *in situ*.

Queste metodologie fisiche complementari e non distruttive sono state utilizzate e implementate per l'indagine di diversi reperti archeologici provenienti da diversi

contesti. In particolare, sono stati affrontati e trattati nella tesi i seguenti cinque casi studio:

1. Scopo del primo caso studio è determinare i materiali, il processo produttivo e le caratteristiche tecnologiche di tre monete suberate (due denari romani e uno statere greco) conservate nel Museo Archeologico dei Brettii e degli Enotri di Cosenza.
2. Scopo di questo caso studio è comprendere i processi di ossidazione, conoscere il materiale costituente e trovare segni o iscrizioni nascoste in due monete completamente ossidate conservate nel Museo Archeologico dei Brettii e degli Enotri di Cosenza.
3. Scopo del presente caso studio è determinare i materiali e le caratteristiche tecnologiche di un oggetto definito come un *unicum* e leggere eventuali iscrizioni e decorazioni sotto le incrostazioni superficiali di una sottile lamina bronzea. Entrambi i reperti sono stati rinvenuti nel sito archeologico di Timpone della Motta a Francavilla Marittima (CC).
4. In questo caso studio sono state studiate la composizione chimica della lega di bronzo e le caratteristiche tecnico-fisiche di due coppie antropomorfe utilizzate come pendenti e risalenti alla prima età del ferro. La prima, denominata “tipo B”, è stata scoperta nel sito archeologico di Pietrapaola (CS), invece la seconda, denominata “tipo A”,. è stata scoperta nel sito archeologico di Bucita-Rossano (CS).
5. Nell’ultimo caso studio sono stati indagati lo stato di conservazione e la composizione chimica di 12 specchi in bronzo magno-greco. Questi eccezionali reperti sono un chiaro esempio dell'alto livello raggiunto dall'artigianato della Magna Grecia. Sono conservati nel Museo Archeologico Nazionale di Locri Epizefiri

e scoperti nella Necropoli di Contrada Lucifero. Sono datati tra la seconda metà del VI secolo a.C. e la prima metà del IV secolo a.C.

ACKNOWLEDGEMENTS

I would like to express my special appreciation and thanks to Professor Vincenzo Formoso and Professor Giuseppe Agostino, who have been formidable mentors and guides for me throughout the duration of this PhD course and the drawing up of my PhD thesis.

I'm grateful to the Danish Institute in Rome in the person of Jan Kindberg Jacobsen for sponsoring, in conjunction with the Physics Department of the University of Calabria, my tuition fees and allowances through scholarship.

I would also like to acknowledge the contribution of the following individuals who allowed me to study these archaeological finds, without which the work presented here would not have been possible.

- Gloria Paola Mittica, project director of Escavations on Timpone della Motta in Francavilla Marittima (Cs);
- Armando Taliano Grasso, professor of Ancient Topography and head of Ancient Topography laboratory of the University of Calabria;
- Maria Cerzoso, director and curator of "Brettii and Enotri" museum in Cosenza;
- Rossella Agostino, director of the National Archaeological Museum of Locri Epizefiri (Rc).

To my wonderful wife Sara and my lovely daughter Michela, thank you very much for your understanding, patience, unconditional love, support and encouragement. You are one of my sources of strength and the work presented here is dedicated to you.

INTRODUCTION

What is archaeometry?

Archaeometry is the application of scientific methods and technology to archaeological study.

However, archeometry is much more than a short definition, it is above all a formal field of study whose practitioners apply techniques and approaches from the physical, chemical and biological field, and also from earth sciences and engineering to address archaeological questions and problems. [1] Heritage Science encompasses different disciplines from the field of pure and applied sciences, engineering and humanities. Heritage Science aims to understand the composition, the technological processes, the conservation and preservation of Cultural and Archaelogical Heritage. It includes all forms of scientific research on artworks created by human beings and those that originate from the interaction between human beings and nature.

In the late eighteenth century, Friedrich Klaproth analysed the composition of ancient metal coins. This was the first manifestation of archaeometry, or better of the systematic application of scientific methods and studies in the field of archaeology. [2]

A lot has changed since then. Today the modern approach to the study of cultural heritage is highly interdisciplinary. The archaeometry expert, better called conservation scientist, has to be a multidisciplinary figure with different skills also in humanities (art historians, philologists, curators and conservators) and technical disciplines (restorers and conservation). So, this knowledge, allows conservation scientists to collaborate in teams with other specialists and professionals. The conservation scientist is one of the most important figures in the care, conservation, restoration and improvement of Cultural Heritage. He acts responsibly in accordance with the history, the protection and the integrity of the cultural heritage artefact.

Archaeometry is a research area which concerns the scientific study, by laboratory analysis of the artefacts based, usually, on the interaction radiation-matter, and it allows to get any kind of information on the artefacts. In recent years, technological applications, and in particular the fields of cultural heritage are evolving. With the technological advancement, the conservation scientists' needs for non-destructive and non-invasive techniques are increasing.

Materials of all types can be encountered, for instance: stones, gems, ceramics, terracotta, enamels, glasses, wood, paper, leather, textiles, bone, ivory, metals, jewellery, paint layers, canvas and wooden backings, pigments, oils, binding media, varnishes, and so on. [2]

Why is it important examine, characterize and analyse the cultural heritage artefacts? For instance, analysing and defining the natural origin of a material like gems, pigments, stones, metals allow us to understand commercial trade links and/or cultural exchanges which may have existed during the period of the artefact's creation; to evaluate the most likely age of an artefact enables us to understand if an object is a copy or fake. [2]

For the examination, characterisation and analysis of cultural heritage artefacts or art objects and their component materials, today the conservation scientist needs a palette of non-destructive and non-invasive techniques, to improve the understanding of their manufacture, their evolution and/or degradation during the time. [2]

The aim of my PhD research work is the use and implementation of X-ray computing microtomography (X-ray μCT) and the micro X-ray fluorescence spectroscopy (μXRF) in the portable version in order to characterize archaeological material, to study their conservation status and to find peculiarities to hypothesize their production process.

X-ray μCT is one of the most commonly used imaging techniques for inspecting the internal morphology of an object. It is a diagnostic method which is frequently used, in particular, in cultural heritage. X-ray μCT is a non-destructive method which does not require a specific sample preparation. It is used to characterize material microstructure in three dimensions with the resolution of the order of microns. The X-ray μCT experimental apparatus used in my PhD research work was implemented at the STAR-Lab facility realized under the PON MaTeRia project, at University of Calabria (Italy).

The portable μXRF is an analytical technique for elemental characterization that provides both qualitative and quantitative information. It is a non-destructive method which does not require a specific sample preparation and it allows to carry out investigations in situ. These features make it one of the most common and simple techniques in archaeometric studies. The XRF instrument used in my PhD research work is the Artax 400 by Bruker.

Archaeometric investigations were performed on different archaeological find from different archaeological contexts. They are:

- One silver plated Greek and two silver plated Roman coins from the “Brettii and Enotri” museum in Cosenza;
- Two fully oxidized copper coins found in Cave of the Nymphs, an ancient source of sulphurous water near Cerchiara di Calabria (Cs), and conserved in the “Brettii and Enotri” museum in Cosenza;
- An *unicum* object and a tin bronze plaque found in Archaeological site of Francavilla Marittima (Cs);
- Two bronze statuettes anthropomorphic couples as pendants depicting a couple of male and female found in Archaeological site of Pietrapaola (Cs) and Bucita of Rossano (Cs);

- Twelve Magno-Greek bronze mirrors conserved at the National Archaeological Museum of Locri Epizefiri.

These case studies are described in Chapter 4, however in Chapter 1 I introduced the X-ray theory and in Chapter 2 I described the non-destructive physical methodologies such as the X-ray computing microtomography and the portable X-ray fluorescence spectroscopy. The experimental instruments are described in Chapter 3.

1. CHAPTER: Background

1.1. X-ray introduction

X-rays were discovered in 1895 by Wilhelm Conrad Rontgen. For his discovery, Rontgen received the first Nobel Prize in physics, in 1901. X-ray is an electromagnetic radiation with wavelengths (λ) between 10^{-2} and 10^{2} Å, frequencies (ν) between 10^{16} and 10^{20} Hz and energy (*E*) between 10^{-1} and 10^{2} KeV. X-ray are subdivided in *Soft* (10^{-1} KeV < *E* < 10 KeV) and *Hard* (10^{1} KeV < *E* < 10^{2} KeV). These physical quantities are related by the following equations:

$$\mathbf{E} = \mathbf{h\nu} \tag{1.1}$$

$$\boldsymbol{\nu} = \frac{\mathbf{c}}{\boldsymbol{\lambda}} \tag{1.2}$$

where *c* is speed of light and *h* is a Planck constant

The following figure describes a portion of the electromagnetic spectrum with energy (E) between 1eV and 10 MeV.

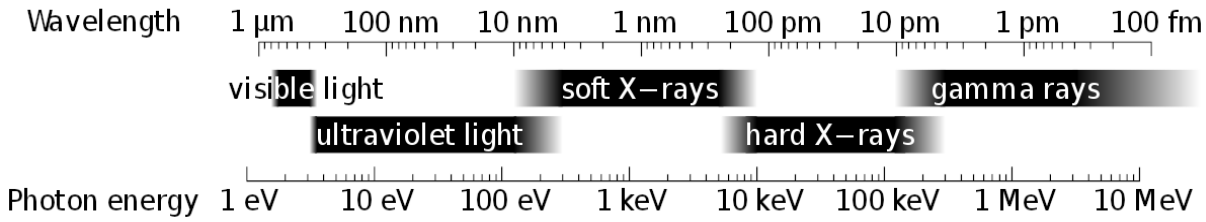

Fig. 1.1: portion of the electromagnetic spectrum with energy (*E*) between 1eV and 10 MeV

The main sources used to produce X-rays are:

- Linear accelerator
- Synchrotron sources
- X-ray tube: classical X-ray tube, rotating anode, microfocus

The X-ray tube contains two principal elements, cathode and anode that operate in an evacuated bulb.

The cathode is an electron gun that produces a collimated electron beam. The anode of the X-ray tube is frequently referred to as the target, while the cathode is sometimes called the filament. The metal filament, heated by electrical currents, produces electrons by thermionic emission. The electrons are accelerated to the anode by a positive potential. The X-ray energy result from collisional interactions between the accelerated electrons and the atoms of the target material being bombarded. Figure 2 shows a schematic of an X-ray Tube.

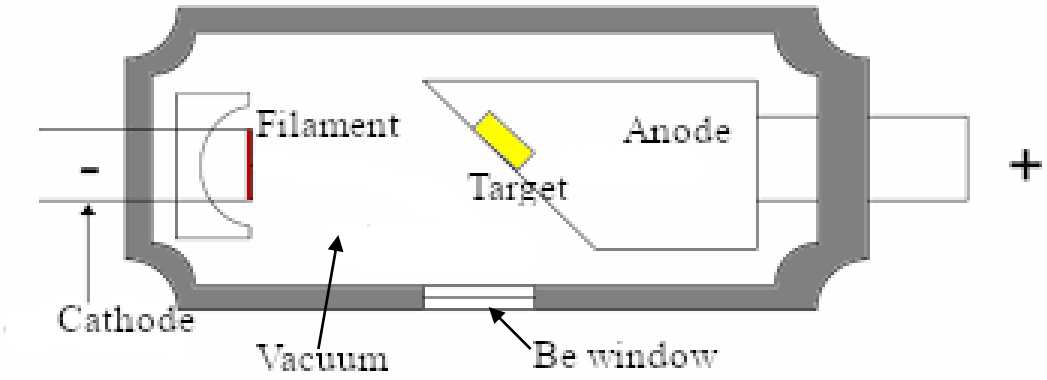

Figure 1.2: Schematic of X-ray tube

According to Bohr's model, an atom consists of a dense nucleus made of protons and neutrons at its centre and surrounded by clouds of negatively charged electrons located in their orbitals, also referred to as levels or shells. These levels are designated by the letters K, L, M, N and so on as they become further away from the nucleus.

Bohr's theory holds on three assumptions [3]:

- The electron moves along definite orbits without radiating energy;
- The stationary orbits are attained at distances for which the angular momentum of the revolving electron is an integer multiple of the reduced Planck constant:

$$\mathbf{mvr} = \mathbf{n}\hbar \tag{1.3}$$

where: *v* is the velocity of a particle, *r* is the orbit's radius, *n* is the entire number that is called the principal quantum number, *ħ* is the reduced Planck constant.

- ✓ The atom radiates energy only when an electron makes a transition from one stationary state to another. The frequency of the radiation is determined by the following equation:

$$\boldsymbol{\nu} = \frac{\mathbf{E_1} - \mathbf{E_0}}{\mathbf{h}} \tag{1.4}$$

Figures 3 show a schematic of the copper atom based on Bohr's model

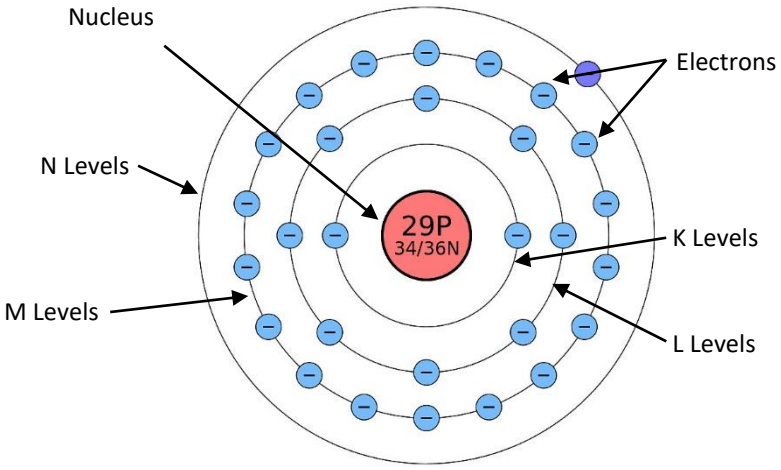

Fig. 1.3: Basic structure of copper atom in ground state

So, the highly energetic electrons interact with the x-ray tube anode (generally made of tungsten, which has 74 protons in the nucleus) cause electron-atom interaction phenomena that generate x-ray: bremsstrahlung and characteristic radiation [4], as shown in figure 4.

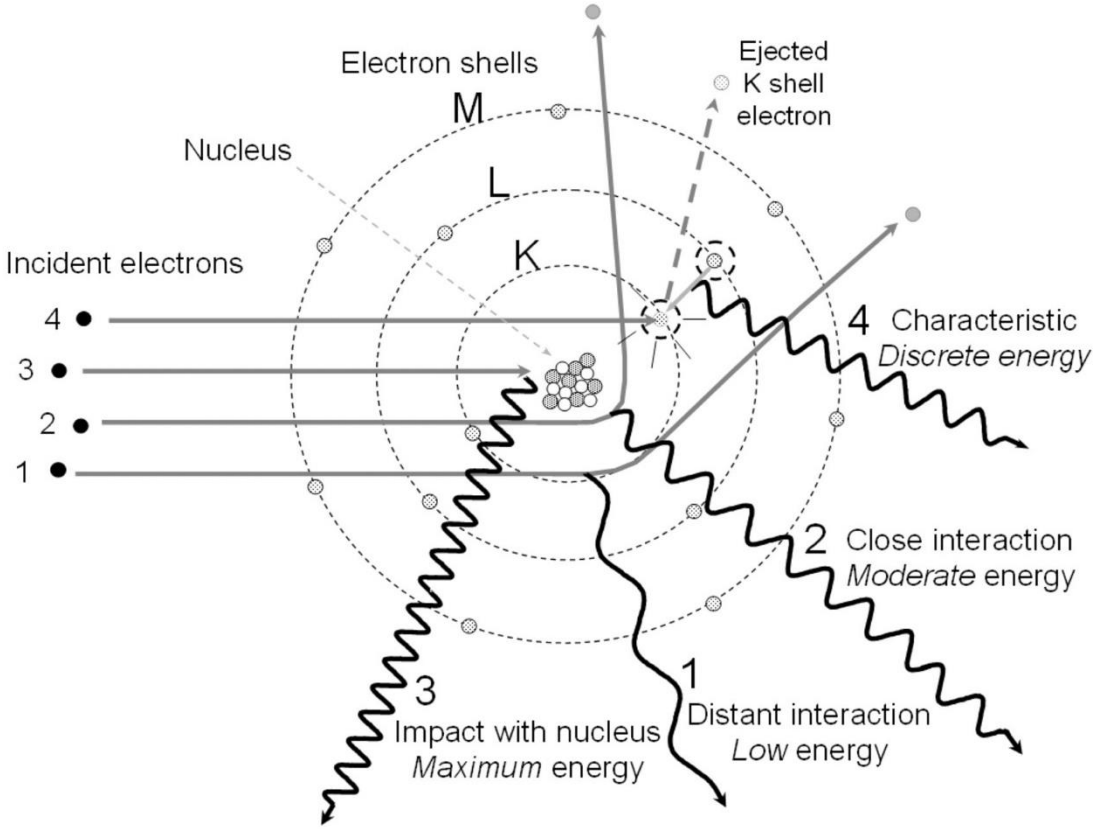

Fig. 1.4: Events 1, 2 and 3 depict incident electrons interacting in the vicinity of the target nucleus, resulting in bremsstrahlung production caused by the deceleration and change of momentum, with the emission of a continuous energy spectrum of x-ray photons. Event 4 demonstrates characteristic radiation emission, where an incident electron with energy greater than the K-shell binding energy collides with and ejects the inner electron creating an unstable vacancy. An outer shell electron transitions to the inner shell and emits an x-ray with energy equal to the difference in binding energies of the outer electron shell and K shell that are “characteristic” of tungsten

In rare events, an electron comes close to the nucleus of a target atom and experiences attractive forces due to the positive charge of the protons in the nucleus. This combined positive charge decelerates and changes the direction of the electron. Kinetic energy loss is converted into electromagnetic radiation with equivalent energy in a process known as bremsstrahlung. The interaction of the incident electron with the field of the atomic nucleus generates a Coulomb force:

$$\mathbf{F} = -\frac{\mathbf{Zq^2}}{\mathbf{4\pi\varepsilon_0 r(t)^2}} \tag{1.5}$$

where: Zq is the charged of an atomic nucleus; ε0 is the dielectric constant of vacuum; t is time; r is the distance between electron and atomic nucleus

The electrons-nucleus interaction causes modification of the electron trajectory and a greater deceleration a:

$$\mathbf{a} = \frac{\mathbf{F}}{\mathbf{m_e}} = -\frac{\mathbf{Zq^2}}{\mathbf{4\pi\varepsilon_0 r(t)^2 m_e}} \tag{1.6}$$

Power of a charged particle emitted radiation that is decelerated is defined by Larmor law as:

$$\mathbf{P} = \frac{\mathbf{q^2 a^2}}{\mathbf{6\pi\varepsilon_0 c^3}} \tag{1.7}$$

Kinetic energy loss as function of time is achieved by integrating the Larmor law:

$$\mathbf{E} = \frac{\mathbf{q^2}}{\mathbf{6\pi\varepsilon_0 c^3}} \int_{-\infty}^{+\infty} \mathbf{P}\,(\mathbf{t})\mathbf{dt} = \frac{\mathbf{q^2}}{\mathbf{6\pi\varepsilon_0 c^3}} \int_{-\infty}^{+\infty} \mathbf{a}\,(\mathbf{t})^{\mathbf{2}}\,\mathbf{dt} =$$
$$= -\frac{\mathbf{Z^2 q^6}}{\mathbf{96\pi^2 \varepsilon_0{}^2 c^3 m_e{}^2}} \int_{-\infty}^{+\infty} \mathbf{r}\,(\mathbf{t})^{-\mathbf{4}}\,\mathbf{dt} \tag{1.8}$$

If we consider that the electron-nucleus interaction takes place in a finite time and the radiation is emitted by pulses, the interaction time ($\boldsymbol{\tau}$) between electron and atomic nucleus, is definied by:

$$\boldsymbol{\tau} = \frac{\mathbf{2b}}{\mathbf{v_e}} \tag{1.9}$$

and the maximum value of acceleration (a_{max}) becomes:

$$\mathbf{a_{max}} = -\frac{\mathbf{Zq^2}}{\mathbf{4\pi\varepsilon_0 b^2 m_e}} \tag{1.10}$$

The equation (1.8) becomes [5]:

$$\mathbf{E} = -\frac{\mathbf{Z^2 q^6}}{\mathbf{96\pi^2\varepsilon_0{}^2 c^3 m_e{}^2 b^4}} \int_0^{\tau} \mathbf{dt} = -\frac{\mathbf{Z^2 q^6}}{\mathbf{48\pi^2\varepsilon_0{}^2 c^3 m_e{}^2 b^3 v_e}} \tag{1.11}$$

The loss of energy is compensated by the production of X photon:

$$\mathbf{E_{k1} - E_{k2} = h\nu} \tag{1.12}$$

where E_{k1} is the initial kinetic energy and E_{k2} is residual energy

The output is a continuous spectrum of x-ray energies with maximum x-ray energy (in keV) determined by the peak potential difference (in kVp):

$$\mathbf{E = qV} = \frac{\mathbf{hc}}{\boldsymbol{\lambda}} \tag{1.13}$$

where V potential difference applied to the electrodes

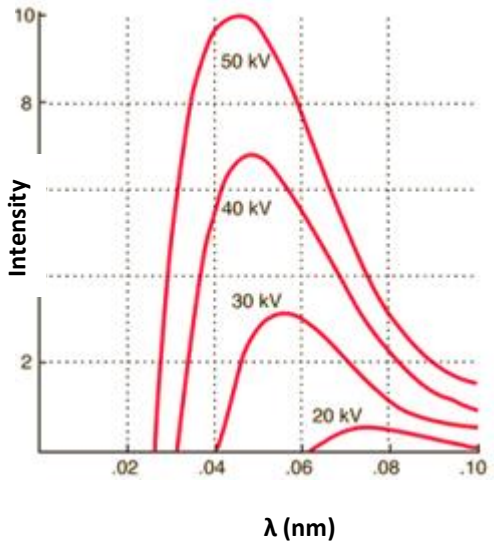

Fig. 1.5: continuous spectrum bremsstrahlung radiation with application of different potentials

Instead, the characteristic radiation is achieved by collision between electron and target atoms. When charged particles pass through matter, they interact with the atomic electrons and lose energy through excitation and ionization processes.

If the transferred energy exceeds the electron's binding energy, ionization occurs, resulting in the electron being ejected from the atom. Whenever a vacancy is created in an inner electronic shell, it is filled by an electron from a more distant (outer) shell. The vacancy moves in an outer shell, which is then filled by an electron (if available) from an even more distant outer shell, and the whole process repeats, producing a cascade of transitions. The energy of this radiation is a characteristic of the particular atom, since it is equal to the difference in the electron binding energies of the initial and final states for the particular transition, which depends on the atomic number.

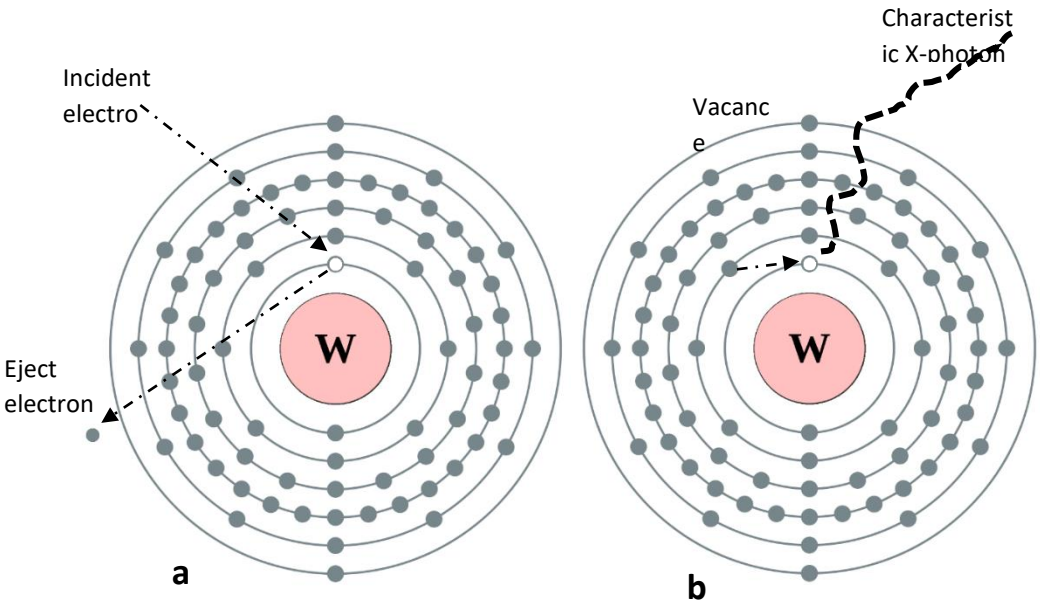

Figure 1.6: tungsten atomic structure (according to Bohr's model). In a the electron being ejected from the atom; in b electronic transition from L level to K shell vacancy, resulting in characteristic X-ray emission

The output is a discrete characteristic spectrum, in addition to bremsstrahlung radiation, as shown in figure 7.

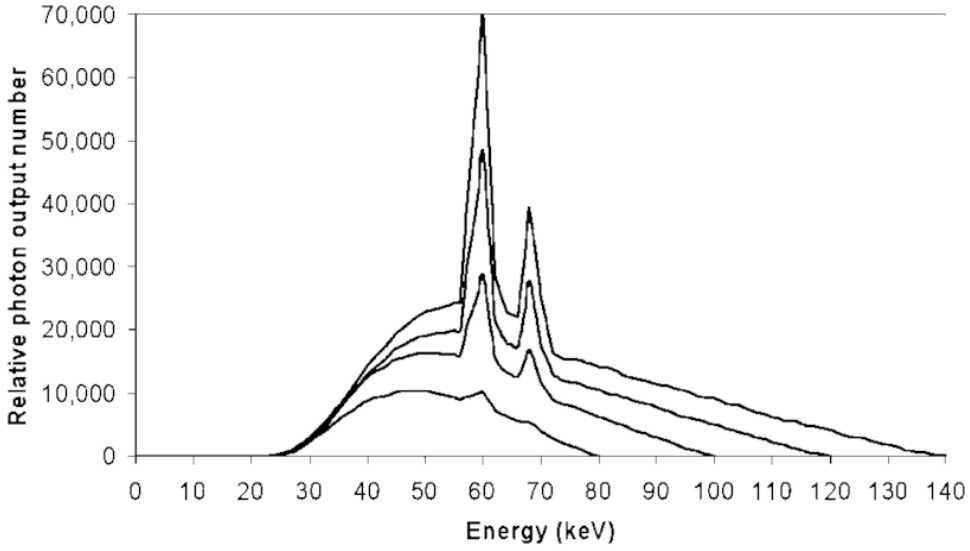

Figure 1.7: Bremsstrahlung and characteristic radiation spectra are shown for a tungsten anode with x-ray tube operation at 80, 100, 120, and 140 kVp and equal tube current

1.2. Radiation-matter interaction

In radiation-matter interaction a large number of processes have been postulated. The behaviour of matter is described by the sum of contributions of the single attenuation processes, main of which are described in 1.2.1 and 1.2.2 paragraph.

The nature of the different interaction processes between X-ray and matter may be described by corpuscular and wave point of view.

These two perspectives are described by the complex refraction index n that is given by:

$$\tilde{\mathbf{n}} = \mathbf{1} - \boldsymbol{\delta} + \mathbf{i}\boldsymbol{\beta} \tag{1.14}$$

The real part δ represents the refractive contribution (electromagnetic interaction) whereas the imaginary part β represents the photon attenuation [6],

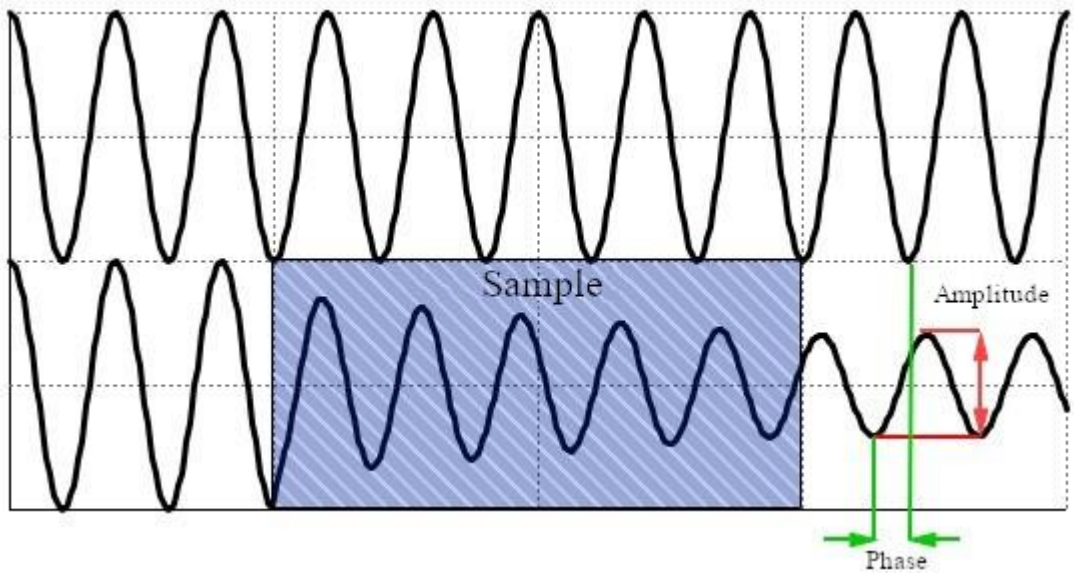

Figure 1.8: schematic representation of the wave phase and amplitude variation after matter interaction

The real and imaginary part are given by:

$$\boldsymbol{\delta = \frac{N r_e \lambda^2}{2\pi} f_1(\omega)} \quad (1.15)$$

$$\boldsymbol{\beta = \frac{N r_e \lambda^2}{2\pi} f_2(\omega)} \quad (1.16)$$

where r_e is the classical electron radius ($2{,}8 \cdot 10^{-15}$ m)

The real part δ and the imaginary part β are linked by Kramers-Kronig's analitic complex function [7]:

$$\boldsymbol{f_1(\omega) = Z - \frac{2}{\pi} \mathcal{P}_C \int_0^\infty \frac{u f_2}{u^2 - \omega^2} du} \quad (1.17)$$

$$\boldsymbol{f_2(\omega) = \frac{2\omega}{\pi} \mathcal{P}_C \int_0^\infty \frac{f_1 - Z}{u^2 - \omega^2} du} \quad (1.18)$$

where Z is the atomic number; $\mathcal{P}_C$ is the Cauchy principal value

The calculation of f_2 is linked to absorption cross-section (σ_A) by:

$$\boldsymbol{f_2 = \frac{\sigma_A}{2 r_e \lambda}} \quad (1.19)$$

Below in figure 1.9 is a graph of the real part and the imaginary part in function of the photon energy variation (lead atoms).

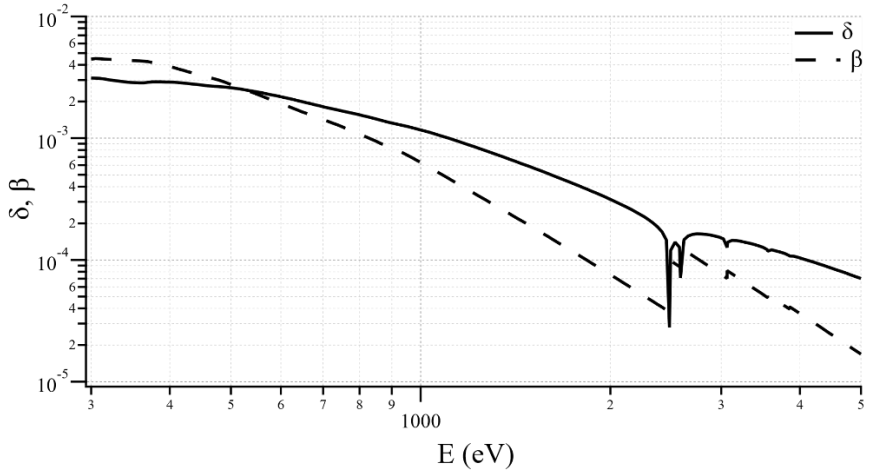

Figure 1.9: δ and β index to change photon energy, for lead

Electric field's equation of plane wave which propagates in an isotropic and homogeneous matter, is:

$$\vec{\mathbf{E}} = \overrightarrow{\mathbf{E_0}}\mathbf{e}^{\mathbf{i}(\tilde{\kappa}\mathbf{x}-\omega\mathbf{t})} \tag{1.20}$$

Where $\tilde{\kappa}$ is complex wave number, it is given by:

$$\tilde{\boldsymbol{\kappa}} = \frac{2\pi}{\lambda}\tilde{\mathbf{n}} \tag{1.21}$$

The intensity is obtained by electric field amplitude:

$$\mathbf{I} \propto \left|\vec{\mathbf{E}}\right|^2 \tag{1.22}$$

Lambert-Beer law relates electric field's equation to the refraction index:

$$\mathbf{I} = \left|\overrightarrow{\mathbf{E_0}}\mathbf{e}^{\mathbf{i}(\tilde{\kappa}\mathbf{x}-\omega\mathbf{t})}\right|^2 \tag{1.23}$$

$$\mathbf{I} = \left|\overrightarrow{\mathbf{E_0}}\right|^2 \mathbf{e}^{\frac{2\pi \mathbf{i}}{\lambda}(\mathbf{nx}-\mathbf{ikx}-\omega \mathbf{t})} \mathbf{e}^{-\frac{2\pi \mathbf{i}}{\lambda}(\mathbf{nx}+\mathbf{ikx}-\omega \mathbf{t})} \tag{1.24}$$

$$\mathbf{I} = \left|\overrightarrow{\mathbf{E_0}}\right|^2 \mathbf{e}^{-\frac{4\pi \mathbf{k}}{\lambda}\mathbf{x}} = \mathbf{I_0 e}^{-\mu_\mathbf{I}\mathbf{x}} \tag{1.25}$$

where I_0 is the incident radiation intensity; μ_I is attenuation coefficient; x is thickness

In a system with variable thickness and composition, the equation (1.25) became:

$$\mathbf{I} = \mathbf{I_0 e}^{-\int_\mathbf{A}^\mathbf{B} \mu_\mathbf{I} \mathbf{dx}} \tag{1.26}$$

Considering matter density (**ρ)**, the equation (1.26) became:

$$\mathbf{I} = \mathbf{I_0 e}^{-\rho \mu \mathbf{x}} \tag{1.27}$$

For a polychromatic X-ray source, the equation (1.27) became:

$$\mathbf{I} = \int_\mathbf{0}^{\mathbf{E_{max}}} \mathbf{I_0 e}^{-\int_\mathbf{A}^\mathbf{B} \rho \mu \mathbf{dx}} \, \mathbf{dE} \tag{1.28}$$

The attenuation coefficient (μ) depends on the absorption probability like:

$$\boldsymbol{\mu} = \frac{\mathbf{N_A}}{\mathbf{A}} \boldsymbol{\sigma}_\mathbf{A} \tag{1.29}$$

where: N_A is Avogadro number; A is the atomic weight

The absorption probability is described by the sum of contributions of the single interaction processes:

$$\boldsymbol{\mu} = \frac{\mathbf{N_A}}{\mathbf{A}} (\boldsymbol{\sigma}_\mathbf{pe} + \boldsymbol{\sigma}_\mathbf{Co} + \boldsymbol{\sigma}_\mathbf{Ra}) \tag{1.30}$$

The equation (1.30) can be rewritten in relation to the scattering factor f_2:

$$\boldsymbol{\mu = \frac{2r_e \lambda N_A}{A} f_2} \tag{1.31}$$

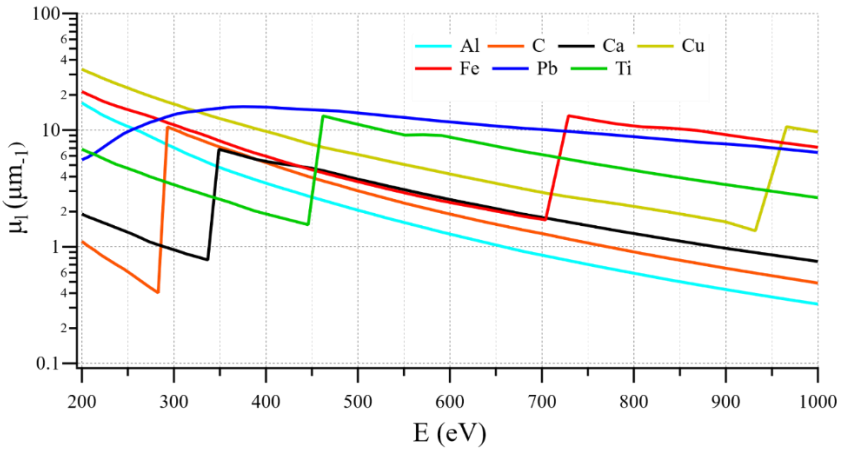

Figure 1.10: linear attenuation coefficient for different elements

1.2.1. Photoelectric and Auger effect

In the photoelectric effect, the incident photon interacts with an atom, which is left in an excited state. The excess energy is released by the ejection of one of the electrons bound to the nucleus. This electron, called a photoelectron, leaves the atom with kinetic energy:

$$\boldsymbol{E_{pe} = h\nu - E_s} \tag{1.32}$$

where: E_s is the binding energy of the electron shell from which the electron came; *h* is Planck's constant; *v* is the photon frequency

The energy transferred to the recoiling atom is very small and can be neglected. The photoelectric effect can only take place if the photon energy, hv, exceeds the binding energy of the electron in that shell. The most probable electron shell to lose an

electron is the one that satisfies this constraint and also has the highest binding energy.

The energy transferred to the recoiling atom is very small and can be neglected. The photoelectric effect can only occur if the photon energy, hν, exceeds the binding energy of the electron in that shell. The most probable electron shell to lose an electron is the one that satisfies this constraint and also has the highest binding energy.

Although this seems like a rather simple process, the calculation of the probability of the interaction is very complicated and quantum mechanics is required. This is because it involves the wave function of the whole atomic electron cloud and these functions are available only for relatively simple atoms.

In the energy range up to 150 keV, the photoelectric effect cross-section per atom, σ_{pe}, is given approximately by:

$$\boldsymbol{\sigma_{pe} \cong \frac{Z^4}{(h\nu)^3}} \qquad (1.33)$$

where: Z is atomic number; h is Planck's constant; ν is the photon frequency

This expression indicates a very strong dependence on the atomic number as well as a strong inverse dependence on photon energy.

The incident photon disappears in the photoelectric interaction. After the interaction, a vacancy is left in the atomic shell structure and this is filled by an electron from a higher shell, with the resulting energy difference being carried off either by a characteristic X-ray (also known as a fluorescent X-ray). After the initial vacancy is filled, the new vacancy or vacancies will themselves be filled and this process will continue with a cascade of events that may finally leave the atom in a highly ionized state. [8]

The Auger effect is a process by which electrons with characteristic energies are ejected from atoms in response to a downward transition by another electron in the atom.

The energy released by the downward transition is given to one of the outer electrons instead of to a photon, and this electron is then ejected from the atom with an energy equal to the energy lost by the electron which made the downward transition minus the binding energy of the electron that is ejected from the atom. Though more involved in interpretation than optical spectra, the analysis of the energy spectrum of these emitted electrons does give information about the atomic energy levels. The Auger effect bears some resemblance to the internal conversion of the nucleus, which also ejects an electron.

The kinetic energy of the Auger electron is equal to [9]:

$$\mathbf{E_{Aug} = E_1 - E_2 - E^*_3 - \Phi} \tag{1.34}$$

where E_1 and E_2 are energy of generic 1 and 2 level; E^*_3 is the binding energy of an electron in the level 3 in the presence of a hole in the level 1; Φ is work function

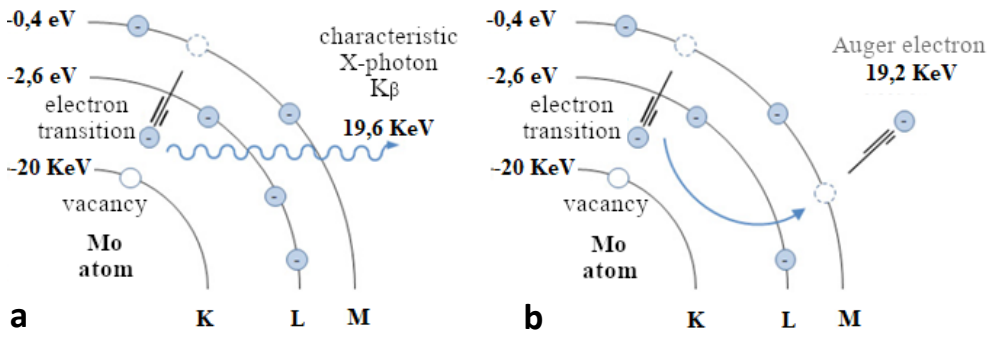

Figure 1.11: X-ray emission (a) and Auger electron ejection (b) after electron transition in K level vacancy

The predominance of the Auger effect or X-ray emission depends mainly on the atomic number of the chemical element and the binding energy of the level where there is the expulsion of the electron. Electron emission is generally more likely in

elements with low atomic numbers, while X-ray production is more pronounced in elements with high atomic numbers. [4]

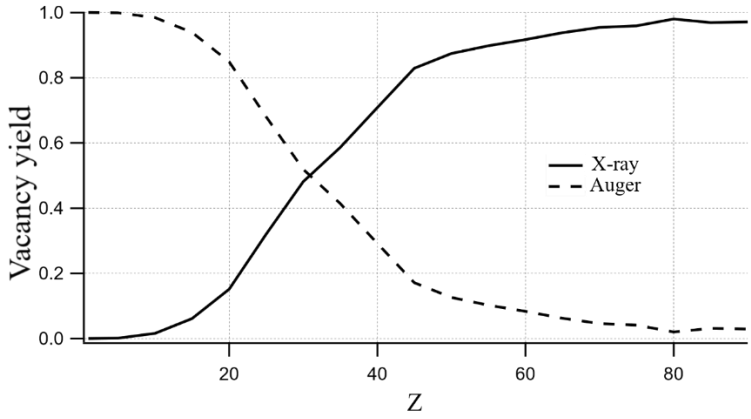

Figure 1.12: photoelectric and Auger effect as a function of the atomic number

1.2.2. Compton and Rayleigh scattering

The Compton effect is the result of the inelastic collision between a photon and an electron. Inelastic scatterings appear when the photon energy is equal to or greater than the electron's rest energy. The result is the diffusion of the photon at an angle θ and the expulsion of the electron that is deflected with an angle Φ. The kinetic energy of the scattered photon is less than incident photon. [5]

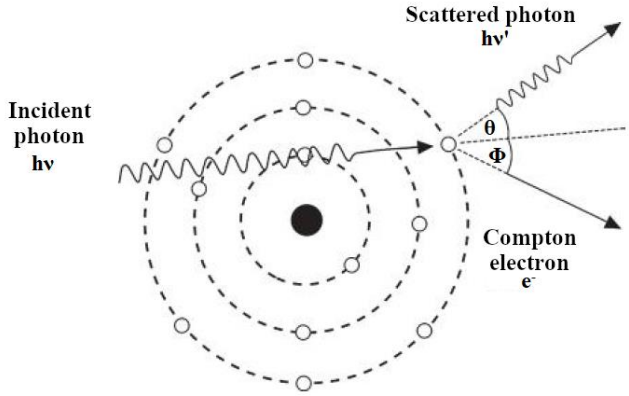

Figure 1.13: Compton scattering

Relationship between change in wavelength and X-ray scattering angle is:

$$\boldsymbol{\lambda' - \lambda = \frac{h}{m_e c}(1 - \cos\theta)} \quad (1.35)$$

where λ’ is scattered photon wavelength and λ is incident photon wavelength

Replacing wavelength with energy, equation (1.35) became:

$$\boldsymbol{\lambda' - \lambda = hc\frac{E - E'}{E'E} = \frac{h}{m_e c}(1 - \cos\theta)} \quad (1.36)$$

$$\boldsymbol{E' = \frac{E}{1 + \frac{E}{m_e c^2}(1 - \cos\theta)}} \quad (1.37)$$

where: E’ is energy after collision; E is energy before collision

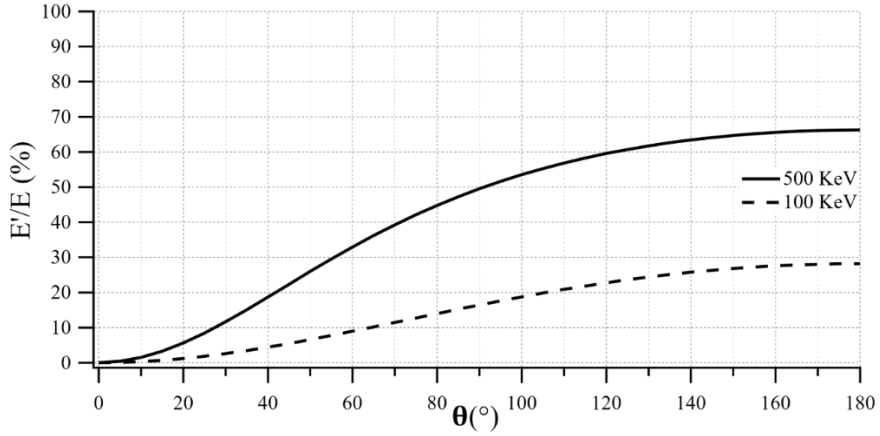

Figure 1.14: energy loss in percent for collision by photon with energy of 100 keV and 500 keV in Compton effect

The Rayleigh effect is the result of the elastic collision between a photon and an electron. When the energy of the incident photon is less than the charge bond, the electric field of the wave accelerates the charge. The scattered electron radiates energy with a frequency equal to the incident radiation. The scattered photon deflected by small angle θ without losing energy. [5]

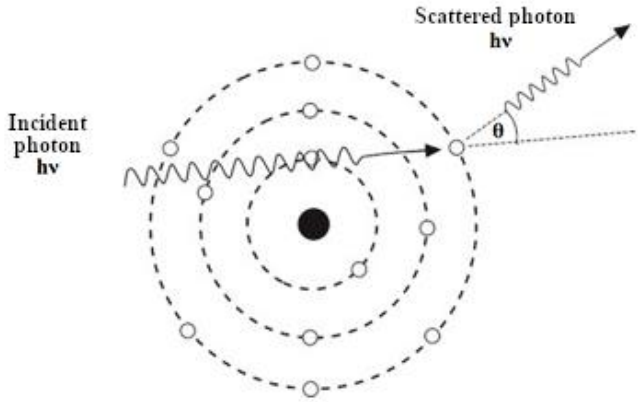

Figure 1.15: Rayleigh scattering

The Rayleigh effect cross-section per atom, σ_{Ra}, is given by:

$$\boldsymbol{\sigma_{Ra}} = \frac{\mathbf{Z^2}}{(\mathbf{h\nu^2})} \tag{1.38}$$

2. CHAPTER: Non-destructive physical methodologies

2.1. X-ray computed tomography

Since the 1970s, X-ray computed tomography (CT) has become a well-established and routinely used modality in modern diagnostic radiology. [10] Beyond that, since the late 1980s, X-ray CT has emerged as a very important and widespread tool in industrial inspection as well as in material sciences. [11]

X-ray computing tomography (CT) is one of the most commonly used imaging techniques for inspecting the internal morphology of an object. It is a diagnostic method which is frequently used, in particular, in cultural heritage. [12]–[15]

X-ray microtomography (μCT) is a non-destructive method which does not require a specific sample preparation. It is used to characterize material microstructure in three dimensions with resolution of the order of microns. [16]–[18]

The computing tomography apparatus setup consists essentially in:

- ✓ X-ray source;
- ✓ Rotating sample holder;
- ✓ Detector.

The sample is positioned between a suitable X-ray source and a detector. The sample is rotated by 360 degree around the vertical axis. At each degree of rotation a radiographic image is acquired. Starting from the radiographic image (projection set), the 3D tomographic slice (i.e., images of the internal structure of the object in a plane parallel to the beam propagation direction) are then reconstructed using appropriate reconstruction software using complex mathematical algorithms.

Figure 2.1 shows a schematic representation of the CT data acquisition principle of operation.

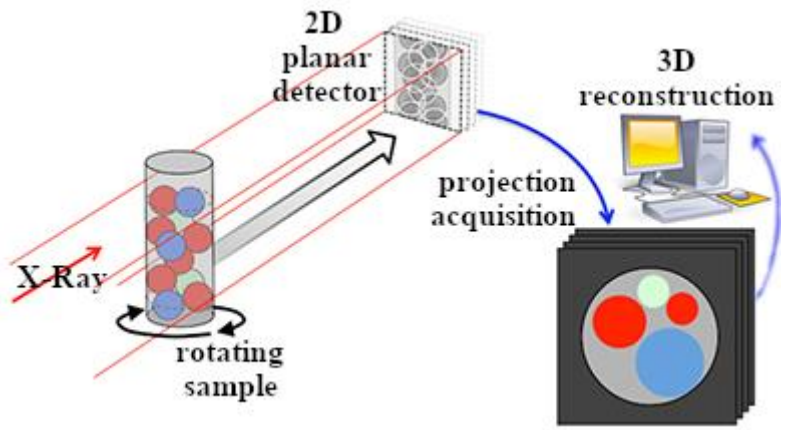

Figure 2.1: schematic representation of the CT data acquisition principle of operation

According to the x-ray production modality, we distinguish between conventional systems based on tubes emitting X-rays with a typical conic emission and synchrotron radiation setups typically fed with intense, and laminar X-ray beams with a nearby parallel beam geometry.

The first, which is the most common way to perform a µ-CT on samples, employs a conventional microfocus based X-ray tube. Like all X-ray tubes, these sources generate X-rays when highly energetic electrons are stopped in a solid metal anode: X-rays result from the conversion of the kinetic energy attained by electrons accelerated under a potential difference into electromagnetic radiation, as a result of collisional and radiative interactions. A divergent polychromatic beam is generated, from which a conical solid angle is selected. Many benchtop µ-CT systems are today able to reach very high-resolution levels, in the range of 1 µm with a voxel size below 0.1 µm. The position of the sample with respect to the source and the detector can be changed to adjust the magnification and the resolution; however the optimal position is always a compromise between sample size and spatial resolution. The detector cameras used for µ-CT systems can be grouped into two categories, according to their ability to discriminate X-ray energy or not. In the first case, we

speak about spectral CT, a promising technique recently introduced in last-generation μ-CT systems thanks to the progress achieved by single-photon counting detectors. In most cases, the detector simply integrates all the X-ray energies.

In general, μ-CT systems adopt digital flat 2D detectors; the most commonly used are charged-coupled device (CCD) systems using scintillator screens coupled via optical fibre bundles for conversion of x-rays into visible photons.

Synchrotron Radiation (SR) sources are based on particle accelerators, where an high-energy (GeV range) electron bunch traveling at relativistic speed in a storage ring. SR provide extremely high brightness and covers a large spectrum of electromagnetic waves, from infrared to hard x-rays. Its main characteristics are the high intensity (orders of magnitude higher than conventional x-ray tubes), the high brilliance, and the low-divergence emission. SR is produced in large accelerator-based facilities equipped with different magnetic structures (bending magnets and insertion devices) optimized to maximize radiation production for the different experimental purposes and user requirements. SR is extracted from the accelerators and transported to the experimental stations through the so-called beamlines. Imaging beamlines are made up of several components used for shaping, focusing/defocusing, filtering, and monochromatize the emitted beam. Experimental stations at hard x-ray imaging beamlines are generally located at a high distance from the source and are, usually, designed and equipped to handle specific experiments, according to the samples under study, taking into account the photon flux, the energy range, the focus, and the collimation of the x-rays. A high level of spatial coherence characterized the SR beam; this allows to exploitation of the phase shift effects occurring to transmitted x-ray waves as a further mechanism contributing to image formation. Contrary to the x-ray tubes, natively synchrotrons provide laminar, nearby parallel geometry, so there is a low magnification of the object on the detector, and scatter contribution to image

formation is negligible. The use of monochromatic x-rays makes negligible the beam hardening artifacts, which is fundamental to extract quantitative information about the sample (such as composition, density, morphology, etc.).

2.1.1. X-ray absorption-contrast computed tomography

Conventional tomographic methods all have the common feature that they rely solely on the absorption of X-rays as a mechanism of contrast formation.

As described in the first chapter, each material has a complex refractive index:

$$\tilde{\mathbf{n}} = \mathbf{1} - \boldsymbol{\delta} + \mathbf{i}\boldsymbol{\beta} \tag{2.1}$$

The imaginary part (β) is a wave amplitude variation, after the interaction with sample. In the absorption-contrast tomography method, imaginary part (β) used to reconstruct the images. The linear absorb coefficient is correlated to the imaginary part by: [19]

$$\boldsymbol{\beta} = \frac{\boldsymbol{\lambda\mu_l}}{\mathbf{4\pi}} \tag{2.2}$$

By measuring the transmitted wave intensity, we can calculate the β distribution in material.

The incident waves are attenuated when they cross the material. From Lambert-Beer's Law for a monochromatic X-ray beam trough a inhomogeneous material, if we know the photon beam intensity before and after sample crossing, we can calculate the linear attenuation coefficient:

$$\mathbf{I} = \mathbf{I_0} \boldsymbol{exp}[\sum_{\boldsymbol{i}}(-\boldsymbol{\mu_i x_i})] \tag{2.3}$$

where: μ_i is the linear attenuation coefficient; x is the thickness of different materials.

Figure 2.2 shows a schematic representation of X-ray radiography: [20]

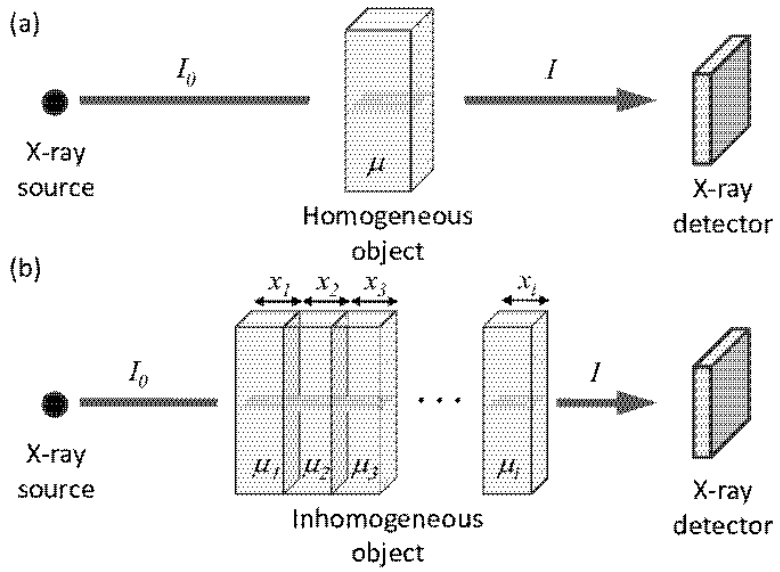

Figure 2.2: Schematic of X-ray radiography: (a) attenuation through homogenous medium and (b) summation of attenuation through heterogenous medium

In a well-calibrated system using a monochromatic X-ray source (i.e. synchrotron) this equation can be solved directly. If a polychromatic X-ray source is used, as is the case of microfocus tube systems, to take into account the fact that the attenuation coefficient is a strong function of X-ray energy. In a continuous and non-homogeneous medium, the complete solution would require solving the equation over the range of the X-ray energy (E) spectrum utilized:

$$\mathbf{I} = \int \mathbf{I_0}(\boldsymbol{E}) \boldsymbol{exp}[-\int_{\boldsymbol{\mathcal{L}}} \mu\,(\boldsymbol{s}, \boldsymbol{E}) \boldsymbol{ds}] \boldsymbol{ds} \tag{2.4}$$

The following expression correlates the number of X-ray photons I_0 that enter the investigated object to the number I of those that leave after traversing a path long $\mathcal{L}$ inside the object thickness.

Under the assumption that a monochromatic X-ray beam is emitted equation (2.4) can be simplified. In such a case the Beer-Lambert law states that:

$$\mathbf{I} = \mathbf{I_0}\, \boldsymbol{exp}[-\int_{\mathcal{L}} \mu\ (\boldsymbol{s})\, \boldsymbol{ds}] \tag{2.5}$$

As one can observe rearranging equation (2.5) a line integral of X-ray attenuation is:

$$\boldsymbol{P} = \boldsymbol{ln}\left(\frac{\boldsymbol{I}}{\boldsymbol{I_0}}\right) = -\int_{\mathcal{L}} \mu\ (\boldsymbol{s})\, \boldsymbol{ds} \tag{2.6}$$

This equation shows that the logarithm of the ratio of the entrance X-ray intensity over the transmitted x-ray intensity represents the line integral of the absorption coefficient along the x-ray path. The term P in CT is usually known as projection. [21] Figure 2.3 shows a schematic illustration of the incident and acquired X-ray represented as a ray passing through the object. [18]

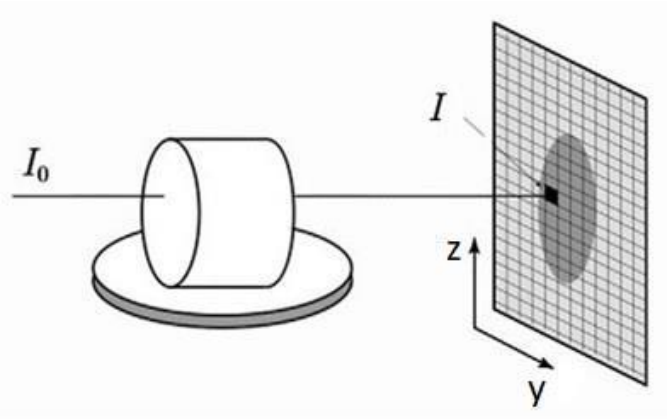

Figure 2.3: Schematic illustration of the incident and acquired X-ray represented as a ray passing through the object

Each radiography image consist of a pixel matrix. Each pixel corresponds to a value of linear attenuation coefficient. The reconstruction images can be represented as a two-dimensional distribution of attenuation coefficients, as shown in figure 2.4:

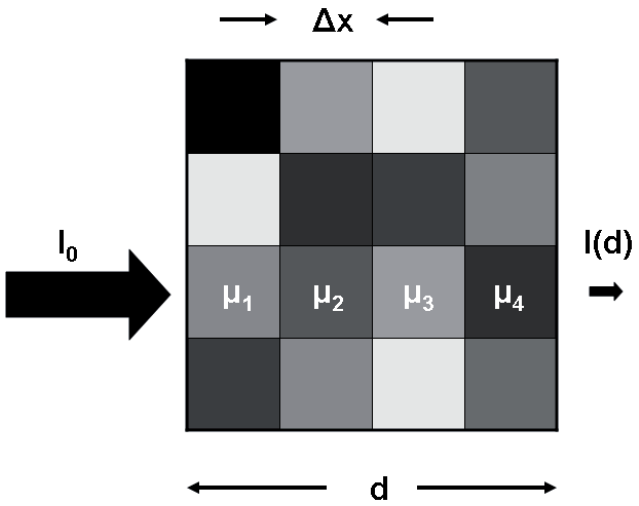

Figure 2.5: Reconstruction images represented as a two-dimensional distribution of attenuation coefficients

The acquired intensity I is modeled as a line integral of X-ray absorption along the ray path. The projection of an object, resulting from the tomographic measurement process at a given angle θ, is made up of a set of line integrals. Such a projection can be defined by:

$$\boldsymbol{P}_{\theta}(\boldsymbol{t}) = \boldsymbol{ln}\left(\frac{\boldsymbol{I}}{\boldsymbol{I_0}}\right) = -\int_{\boldsymbol{path}} \mu\ (\boldsymbol{x},\boldsymbol{y})\ \boldsymbol{ds} \qquad (2.7)$$

Figure 2.5 shows the scanning of a single layer in the plane (x,y). [22]

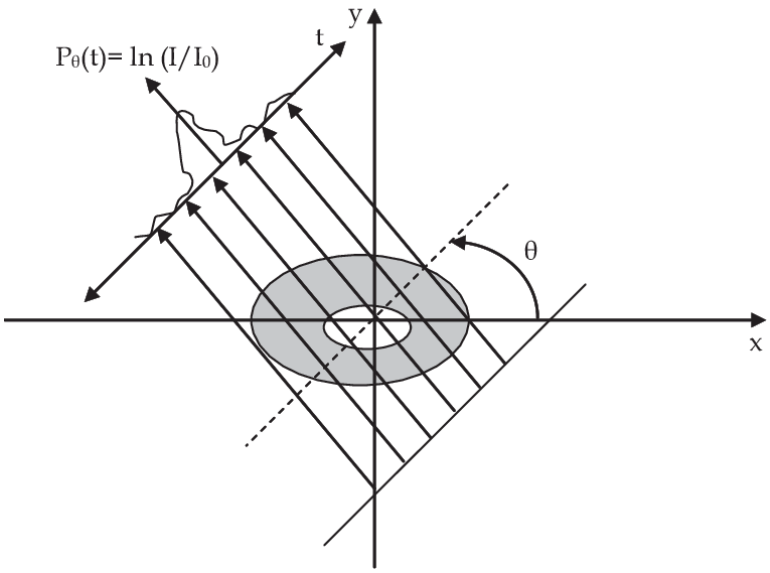

Figure 2.5: Scanning of a single layer in the plane (x, y)

Using complex mathematical algorithms (described in paragraph 2.1.3), the projections sets are reconstructed.

2.1.2. X-ray phase-contrast computed tomography

Around the time of the development of lab-based micro-CT systems, the first steps were being taken to create X-ray images using the refraction of X-rays by matter, in addition to absorption. These imaging methods (so called X-ray phase-contrast tomography) enable the visualization of features in weakly absorbing objects such as polymers, or indeed objects that barely absorb X-rays at all. They also greatly enhance the visibility of weakly absorbing features in the presence of more strongly absorbing sample components. X-ray phase-contrast tomography has particular value in the 2D and 3D characterization of the analysis of composites and multiphase materials where the different components have similar X-ray attenuation coefficients. [23]

In the complex refractive index (see equation 2.1) the real part (δ) is a phase variation of the light.

After the interaction with sample, the incident photon undergoes a phase shift (Φ) which is given by: [24]

$$\boldsymbol{\Phi}\,(\mathbf{x},\mathbf{y}) = \frac{\mathbf{2\pi}}{\boldsymbol{\lambda}} \int_{-\infty}^{+\infty} \boldsymbol{\delta}(\mathbf{x},\mathbf{y},\mathbf{z})\,\mathbf{dz} \tag{2.8}$$

The Φ function represents the development of the δ value in a specific propagation direction.

The parameter δ can be expressed by the equation: [25]

$$\boldsymbol{\delta} = \frac{\boldsymbol{\rho_e}}{\mathbf{E^2}} \cdot \frac{\mathbf{r_e h^2 c^2}}{\mathbf{2\pi}} \tag{2.9}$$

The equation (2.9) shows that the real part of the refraction index (δ) is dependent on electron density (ρ), like the imaginary part (β). However, β is independent by atomic number, as shown in figure 2.6.

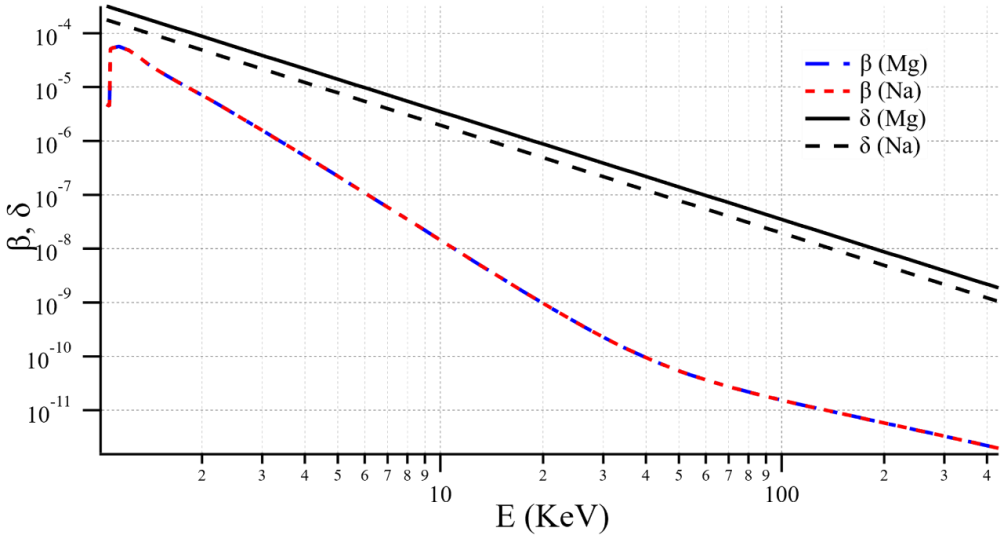

Figure 2.6: Comparison between real and imaginary part for Na and Mg element

The phase shift (δ) value is greater than the amplitude variance (β) value. Thus, in phase-contrast method, the images contrast and signal-to-noise ratio are better.

In this research work, phase contrast was not used, but it is important to know that this technique will be the spearhead when the STAR source is in operation (for more details see Introduction).

2.1.3. X-Ray cone beam microtomography

It is advantageous to perform microfocal CT (microtomography) whereby 3D images are directly reconstructed from a set of 2D projection images recorded with an area detector. [26]

If a volume segment needs to be reconstructed, the complete procedure must be performed slice-by-slice with a small movement of the object or of the source-detector system between each slice. [27]

Figure 2.7 describes the cone beam CT geometry. It is convenient to assume that the X-ray source and detector system are stationary and that the object rotates around the rotation centre. [28] The setup for filtered image acquisition is shown in a. The top view of the setup is shown in (b). For filtered image acquisition a collimator permit focus of FOV (field of view) in the x-ray beam geometry. The ROI (region of interest) filter permits focus the region of interest in the sample. [29]

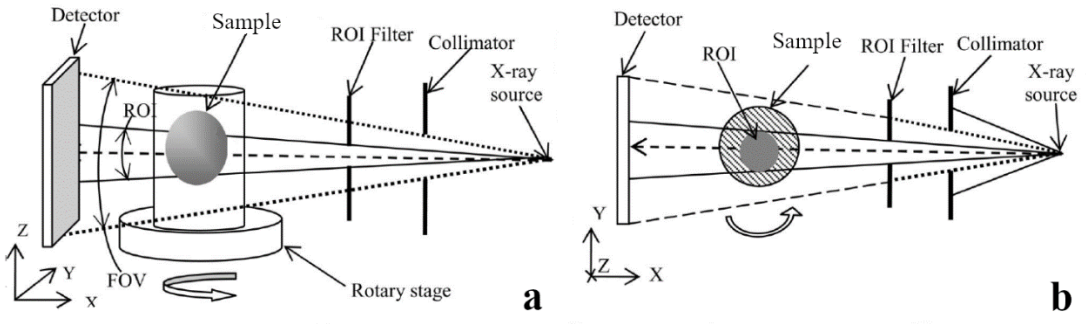

Figure 2.7: Cone beam CT geometry. (a) Setup for filtered image acquisition. (b) The top view of the setup is shown

A schematic diagram of the sequence of the operations to perform an X-ray microtomography measurement is shown in figure 2.8.

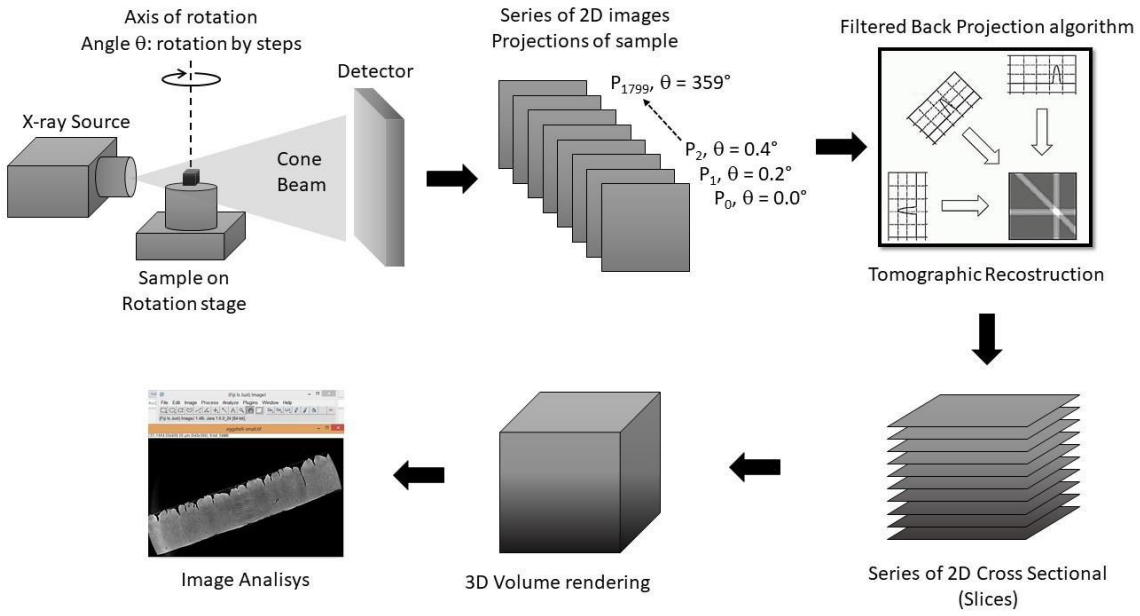

Figure 2.8: Schematic diagram of the sequence of the operations to perform an X-ray microtomography measurement

Cone beam microtomography system is shown in figure 2.9. Among the main physical factors which affect the performance of CBCT (cone beam computed tomography) are system geometry in find the suitable distances such as the SOD (source to object distance) and SDD (source to detector distance), for reducing the scatter artifacts while maintaining high signal difference to noise ratio. [30], [31]

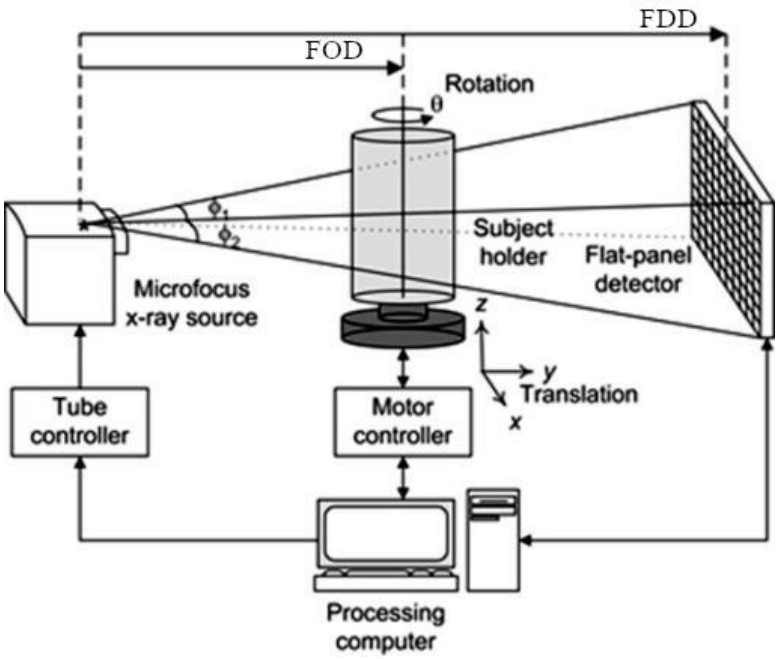

Figure 2.9: Cone beam microtomography system

The head of an X-ray transmission tube contains a slide-like "target", which is covered with a very thin layer of tungsten. This layer has a thickness of 1-10 microns, depending on the application of the X-ray tube. For special tasks different materials can be used for this layer. The transmission target is hit by a focused electron beam in the so-called focal spot. In figure 2.10 a cross section of microfocus transmission X-ray tube is shown.

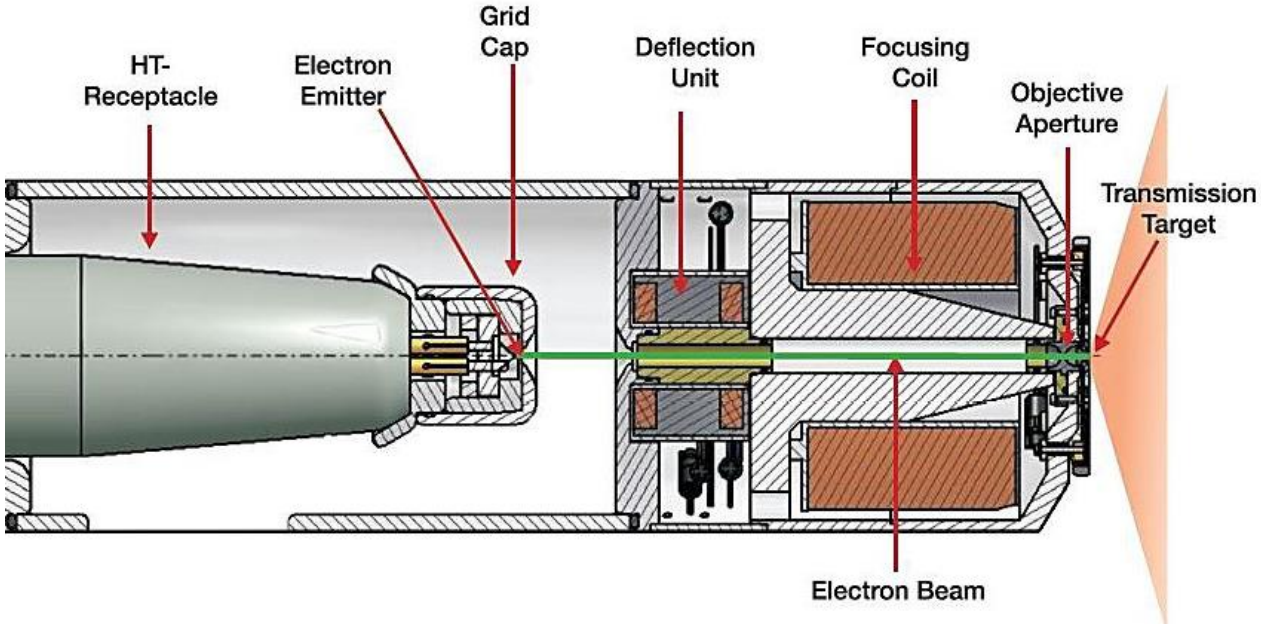

Figure 2.10: Cross section of microfocus transmission X-ray tube

The focal spot size affects the spatial resolution and defines the sharpness of the resulting X-ray image. The object is near the focal spot (the smaller the value of FOD), there is the higher magnification. A bigger focal spot size (F) leads to higher unsharpness by generating a wider half shadow (penumbra) of the object, as shown in figure 2.11. [30]

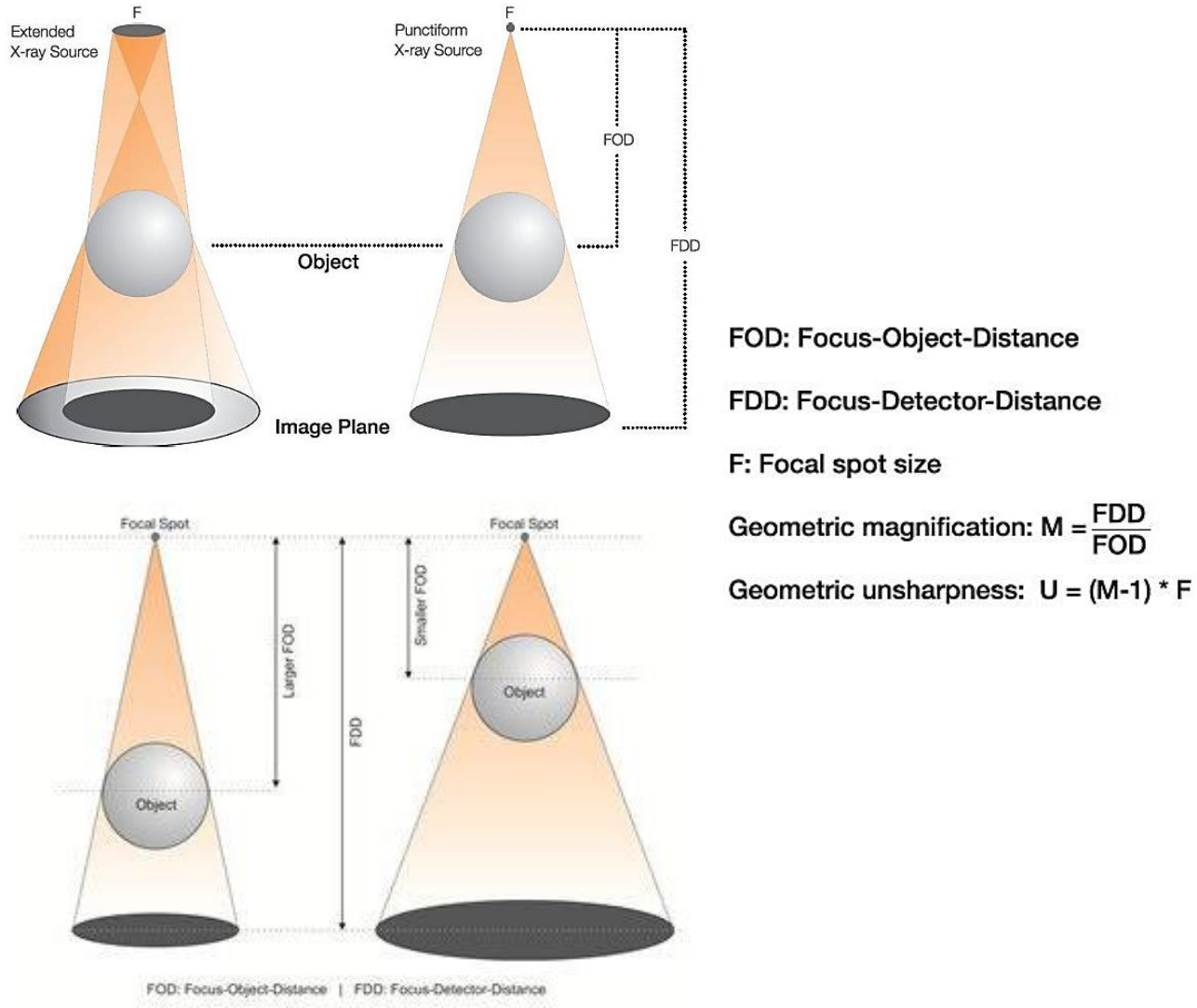

Figure 2.11: Cone beam geometric magnification and geometric unsharpness

The field of view (FOV) affects a loss in contrast and an increase in artifacts. [30] Methods for reducing noise and out-of-field artifacts may enable ultra-high resolution limited-field-of-view imaging. [32]

We can define the dynamic range simply by the ratio of the maximum and the minimum detectable signal, measured in grey level or can also refer to an effective number of bits in the detector. The dynamic range of the acquisition system is the relevant quantity which determines the maximum material thickness which can be

inspected. [33] When we increase the object size for fixed FOV and geometric system we increase noise, contrast and artifacts. [30]

A higher energy beam KVp reduces the contrast, and increases the noise. A softer beam with a broader spectrum increases the artifacts. [30]

The mAs per projection is the product of tube current (mA) and detector exposure time. Decreasing the mAs per projection implies increasing the number of projections ,but the exposure to the detector may become so low that the electronic noise contributes to the total noise. Instead increasing the mAs per projection implies the reduction of the number of projections. [30]

The most widely used **detectors** in X-ray cone-beam microtomography are planar type (FPI). [30] The principal components consist essentially in: X-ray sensitive layer and active matrix in amorphous silicon. The X-ray radiation is converted into a digital signal through direct or indirect conversion. The first utilize photoconductor, such as amorphous selenium (a-Se), to capture and convert incident X-ray photons directly into electric charge. X-ray photon incident upon a layer of a-Se generate electron-hole pairs via the internal photoelectric effect. A bias voltage applied to the depth of the selenium layer draw the electrons and holes to corresponding electrodes; the generated current is thus proportional to the intensity of the irradiation. Signal is then read out using underlying readout electronics, typically by a thin-film transistor (TFT) array. [34], [35]

An indirect detector contain a layer of scintillator material, typically either gadolinium oxysulfide or cesium iodide, which converts the X-ray into light. Directly behind the scintillator layer is an amorphous silicon detector array. Millions of pixels each containing a thin-film transistor, form a grid patterned in amorphous silicon on the glass substrate. Each pixel also contains a photodiode which generates an electrical signal in proportion to the light produced by the portion of scintillator layer in front

of the pixel. The signals from the photodiodes are amplified and encoded by additional electronics positioned at the edges or behind the sensor array to produce an accurate and sensitive digital representation of the x-ray image. [36], [37]

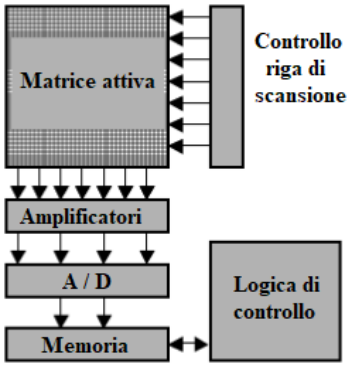

Figure 2.12: Detector electronic

The following parameters define the detector's performance and sensibility: [38]

- Quantum efficiency of scintillator and photodiode;
- Ratio of emitted and absorbed photon;
- Pixel area occupied by the photodiode.

During a µCT scans different kinds of artifacts can occur. Artifact is an artificial feature appearing in an image that is not present in the original investigative object. Typically, artifacts are due to: [39]

- physical processes involved in the obtaining of µCT scans;
- hardware malfunction;
- unintentional sample movements
- image reconstruction process

Some of the µCT artifacts are described below:

✓ **Ring artefact**: that appears as rings centred on the rotation axis. These ring artifacts are mainly caused by the poor performance of the flat panel detector.

Generally the signal responses of all pixels cannot vary smoothly. Defective or badly calibrated pixels in a flat panel detector can be changed dramatically different from their neighbourhood by a nonlinear response to overcoming intensity. As a result they form sharp rings in the reconstructed images. On the other hand, it can also be due to variations or imperfections in the incoming beam. Due to the data, the constructed images are corrupted by these ring artifacts, qualitative and quantitative analysis of CBCT images will be compromised as well. Post processing such as noise reduction, image segmentation and image registration also become more complex due to the presence of such artifacts. [40]

The generation process of the ring artifacts and a ring artifacts in a X-ray image are shown in figure 2.13:

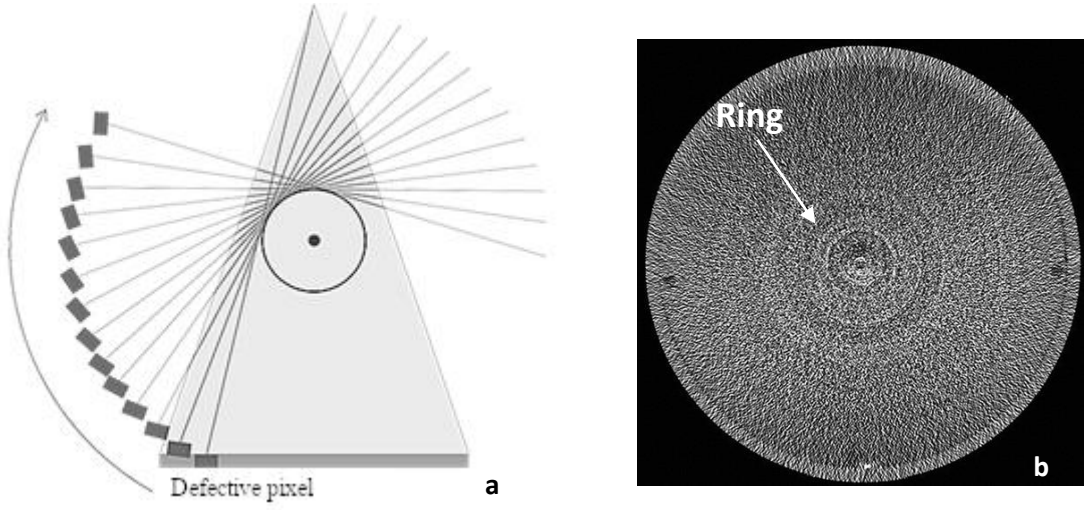

Figure 2.13: Generation process of the ring artifacts (a); ring artifact in a X-ray image (b)

- ✓ **Beam hardening artifact:** that occurs when an x-ray beam comprised of polychromatic energies passes through an object, resulting in selective attenuation of lower energy photons. The effect is conceptually similar to a high-pass filter, in that only higher energy photons are left to contribute to the beam

and thus the mean beam energy is increased. The result is a falsely bright appearance along the periphery of an object. Because the x-ray beam is "hardened" by passing through the sample, the mean photon energy will be higher near the sample border. If uncorrected during µCT reconstruction, these differences in the expected attenuation profile lead to a peripherally dense appearance. A filter may be used to absorb low-energy in an attempt to overcome beam hardening. [41]

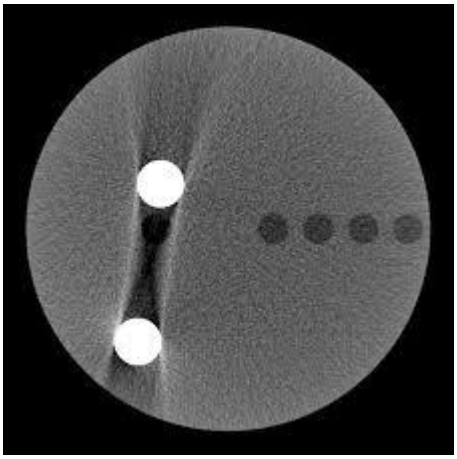

Figure 2.14: Beam hardening artifact in a X-ray image

- ✓ **Sample movements artifact:** is due to unintentional sample movements during µCT scan. This will cause a reduction of the sharpness of the image, as shown in figure 2.15. [42]

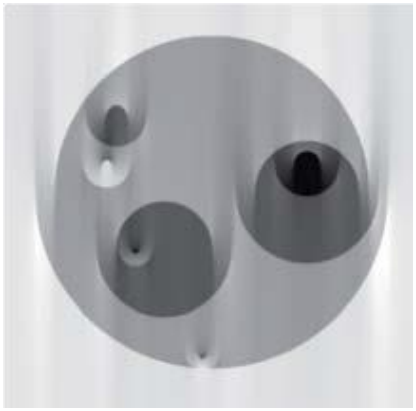

Figure 2.15: Reduction of the sharpness of the image due to sample movements artifact

- ✓ **Aliasing artifact:** occurs when the Nyquist theorem is not applied. [43]

$$Np \geq d_{max} \, {}^{\pi}/_{2}$$

Where: Np is projection number; dmax is the sample size in pixel

Figure 2.16 shows a µCT image reconstruction by increasing number of projections.

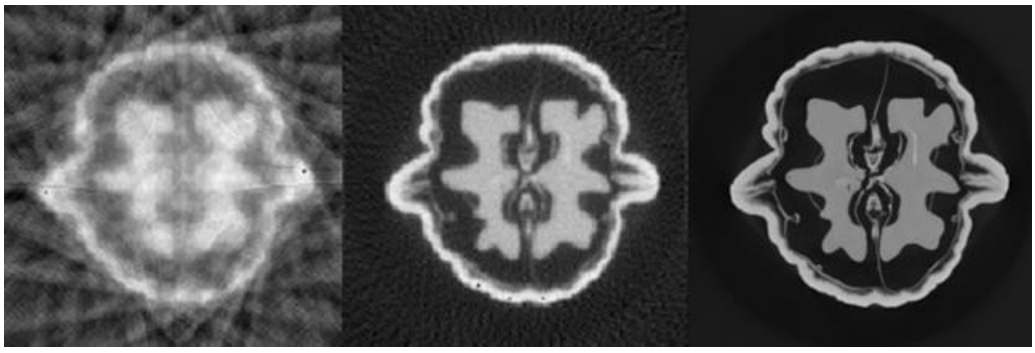

Figure 2.16: µCT image reconstruction by increasing number of projections.

The image reconstruction process involves generating images from the x-ray data collected during the CT scan process, improving image quality through intense mathematical computation. Among the most popular algorithms used for X-ray cone-

beam μCT image reconstruction is Feldkamp et al. (FDK algorithm). This algorithm uses filtered back projection, however, due to the use of a circular trajectory, it cannot provide exact reconstructions.

The general algorithm is described as:

1. Scale projections by cosine of the cone angle.
2. Apply ramp filtering to the data.
3. Apply weighted-filtered back projection.

The FDK algorithm implements the core of the fan-beam algorithm, with a few additions to ensure it applies to three-dimensional reconstruction. To ensure understanding of the differences and additions to this algorithm, let us analyze the coordinate system for the FDK algorithm as pictures in figure 2.17. [44]

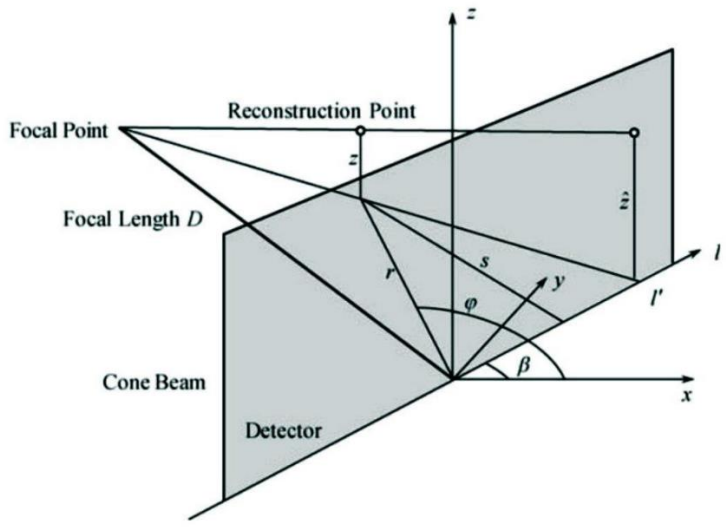

Figure 2.17: The coordinate system for Feldkamp's cone-beam algorithm.

The mathematical equation is expressed as follows:

$$\mathbf{f}(\boldsymbol{r},\boldsymbol{\varphi},\boldsymbol{z}) = \frac{\mathbf{1}}{\mathbf{2}}\int_{\mathbf{0}}^{\mathbf{2\pi}} \frac{\mathbf{D}}{\mathbf{D-s}} \int_{-\infty}^{+\infty} \frac{\mathbf{D}}{\sqrt{\mathbf{D^2}+\boldsymbol{l}^2+\hat{z}^2}}\mathbf{g}\,(\boldsymbol{l},\hat{z},\boldsymbol{\beta})\mathbf{h}(\boldsymbol{l}'-\boldsymbol{l})\mathbf{d}\boldsymbol{l}\mathbf{d}\boldsymbol{\beta} \qquad (2.10)$$

$$s = r \sin(\varphi - \beta) \tag{2.11}$$

$$l' = \frac{Dr \cos(\varphi - \beta)}{D - r \sin(\varphi - \beta)} \tag{2.12}$$

D represents the focal length, and l is the linear coordinate on the detector. This equation is performed by weighting, ramp filtering (including the inverse Fourier Transform), and then performing back projection to reconstruct the three dimensional image.

2.2. Portable μX-ray fluorescence spectroscopy

X-ray fluorescence spectroscopy (XRF) is an analytical technique for elemental characterization that provides both qualitative and quantitative information. [45], [46]

It can be set on a portable instrument, and that allows to carry out investigations in situ. It is a non-destructive method which does not require a specific sample preparation. These features make it one of the most common and simple techniques in archaeometric studies. [47]–[50]

As we saw in chapter 1, the energy of X-rays is of the same order of magnitude as the binding energies of inner shell electrons and can, therefore, be used to excite or probe these atomic levels. [46] The electromagnetic wave is emitted and absorbed in a package of discrete energy called photons where energy is proportional to the frequency of radiation. The atom described as Bohr atomic model is composed of a nucleus containing protons and the electrons occupying discrete energy shells.

If the sample is irradiated by incoming X-ray of energy EO that is equal to or higher than the binding energy of, for example an electron in the K shell, the electron will be ejected from the atom leaving it in an ionised or excited state. An atom in ionised

state is unstable and electrons from higher shell level will fill in the vacancy created by the ejected electron. For example, if a K shell electron is ejected, the vacancy will be filled by an electron from one L, M, or N sub-shells. Each transition constitutes an energy loss resulting in emission of characteristic X-ray with energy equal to the difference between the energy levels involved. This process is called X-ray fluorescence.

The emission of this characteristic radiation allows the identification of elements. The elements can be quantified by measurement of the energy of characteristic X-ray photons emitted from the sample from the line spectra with all the characteristic lines superimposed above a certain fluctuating background. [51]

Additional notions such as α, β and γ indicate which higher energy sub-shell the electron originated from. For example, Kα1 and Kα2 indicate the transitions from L3 and L2 subshells, whereas, K β1, K β2, K β3 lines are produced during the transitions from M3, N2 and M2 subshells. [51] Each electron is defined by four quantum numbers, principal quantum number n, which can take all integral values (for K level n=1, for L level n=2 and so on), angular quantum number l that can take all values from (n−1) to 0, m is the magnetic quantum number take values from +l to −l and last is spin quantum number s, with a value of ±1/2. Total momentum J of an electron is given by the vector sum of l+s. [51]

For production of normal lines, according to selection rules, the principal quantum number must change by at least one, the angular quantum number must change by only one, and total momentum must change by 0 or 1. [46] Certain lines that do not abide by the basic selection rules and arise from outer orbital levels may also occur in X-ray spectra which are known as forbidden lines. After the ejection of initial electron, the atom can remain in the excited state to such an extent that during this period there is a significant probability of ejection of another electron before the vacancy is

filled. The loss of an electron modifies the energies of surrounding electrons and thus X-rays with other energies are emitted. These weak lines, known as satellite lines, are not analytically significant and may cause confusion in interpretation of spectra. [45]

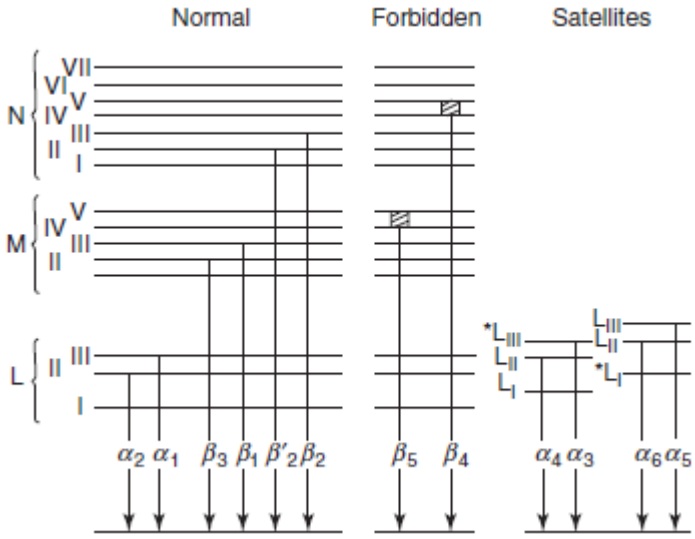

Figure 2.18: Observed characteristic lines in K series for X-ray Fluorescence

The **portable XRF instruments** fall into the energy-dispersive (ED) category. Figure 2.19 shown the block diagram of an ED X-rays fluorescence spectrometer apparatus.

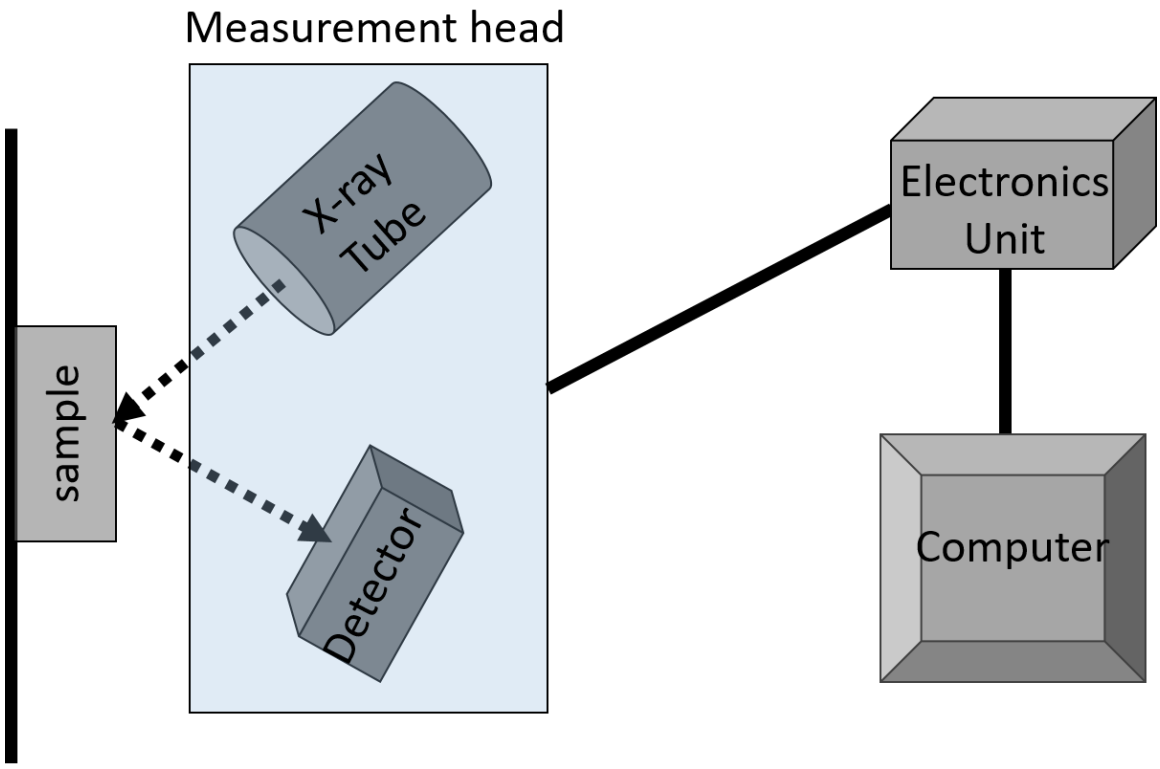

Figure 2.19: Block diagram of a typical energy dispersive X-ray fluorescence EDXRF Spectrometer

The technological developments of the X-ray tubes' miniaturization and of the detector's cooling system allowed the portable XRF development, which are largely used in archaeometry and conservation science. Different X-ray tubes are available for different fields and for different materials to be analysed, according to anode's material present, and to max voltage and max current applicable. These features make this methodology extremely versatile. Different typology of X-ray tubes can be used in pXRF depending on the sample features. [52]

Table 2.1 shows any typology of X-ray tube suitable in the archaeometry and conservation science fields.

Groups of elements that can be identified	Anode features			
	Element	Voltage (kV)	Current (mA)	Characteristic line
P, S, Cl	Ca (*K* line)	8 - 10	0.1 - 1	3.7 keV + *B*
P, S, Cl	Pd (*L* line)	3 – 5	0.1 – 1	2.8 keV + *B*
Cl, K, Ca	Ti (*K* line)	10	0.1 – 1	4.5 keV + *B*
K ÷ Y (*K* line)	Mo (*K* line)	30	0.1 - 1	17.5 keV + *B*
Cd ÷ U (*L* line)				
K ÷ Sn (*K* line)	Pd (*L* line)	35	0.1 – 1	21.1 keV + *B*
Cd ÷ U (*L* line)				
K ÷ Y (*K* line)	W	35	0.1 – 1	*B*
Tb ÷ U (*L* line)				
Zn ÷ Ba (*K* line)	W	50	0.1 - 1	*B*
Tb ÷ U (*L* line)				

Table 2.1: different typology of X-ray tube in pXRF used in archeometry field. For each group of elements that can be identified anode typology, max voltage (kV), current (mA), characteristic line and *Bremsstrahlung* radiation (*B*) are shown.

In **μXRF spectrometer,** the primary difference is the X-ray beam spot size. In XRF spectrometer the primary beam has dimensions of millimetres to centimetres, limiting its spatial resolution. In μXRF spectrometer the X-ray beam spot size that can be collimated up to micrometric size.

Usually, two types of detectors are used to analyse characteristic fluorescence X-ray: the first one, cooled by liquid nitrogen, are used in benchtop XRF spectrometry; the other, with thermoelectric cooling system, are used in portable XRF spectrometry. [52], [53]

A silicon drift detector (SDD) with Peltier cooling system, is usually used in portable μXRF spectrometer. The SDD concept is of great flexibility in the choice of anode arrangements and drift directions. This detector can be achieved good energy efficiency even at room temperature (150 eV FWHM to 5.9 KeV), their features are excellent performance and extreme compactness.

Silicon Drift Detectors (SDDs) are based on the principle of sideward depletion introduced by Gatti and Rehak in 1984: [54] a large volume of a high-resistivity semiconductor, in our case *n*- type silicon, is depleted by a small-sized *n*+ ohmic substrate contact reverse-biased with respect to rectifying p+ junctions covering both surfaces of the structure. In an SDD, the p+ junctions are segmented strip-like and biased in such a way that an electric field parallel to the surface exists. Electrons released within the depleted volume by the absorption of ionising radiation or by thermal generation drift in the field towards the n+ substrate contact, which acts collecting anode and is connected to an amplifier. The generated holes are taken away by the p+ junctions. [55]

In an advanced SDD design optimised for applications in X-ray spectroscopy, the concentric ring-shaped p^+ strip system for the generation of the drift field and the collecting anode in their centre are placed on one side of the structure, while the opposite surface is covered by a non-structured p^+ junction acting as homogeneous radiation entrance window. Figure 2.20 shows a cross-section of a cylindrical Silicon Drift Detector (SDD) for X-ray spectroscopy. In the back, there is the equipotential of the entrance window. The field strips with their step-like increasing negative potential are shown in the front. The voltage of the field strips is defined by an integrated voltage divider, only the first and the last ring must be biased externally. There is no field-free region in the device, i.e. the whole volume is sensitive to the absorption of ionising radiation and each generated electron has to fall down to the point of lowest potential energy, which is the anode in the center of the front side. SDDs of this type are not used as position sensors, but as energy dispersive detectors for X-rays and charged particles, taking advantage of the small value of the anode capacitance, which is almost independent of the detector area. For a given number of collected electrons this quality translates to a large amplitude and a short rise time of the

output signal. Compared to a conventional photodiode of equal size which is operated under the same conditions (e.g. temperature, noise of readout electronics) the SDD can be operated at higher count rates and it yields a substantially better energy resolution, because the signal is less sensitive to the noise contribution of the subsequent amplifying electronics. [55]

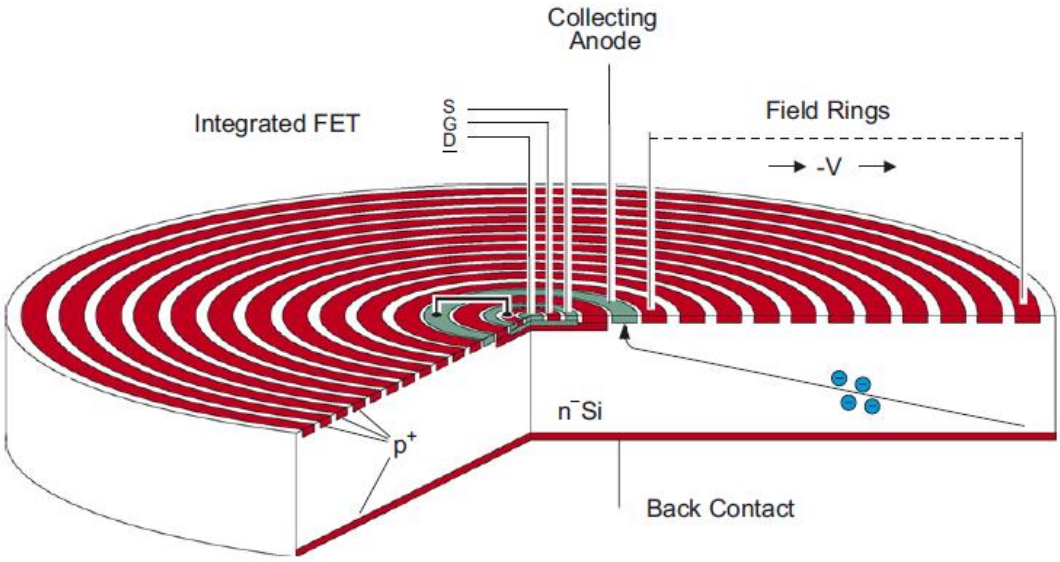

Figure 2.20: Cross-section of a cylindrical Silicon Drift Detector (SDD) for X-ray spectroscopy

Quantitative analysis are available in XRF spectrometry. It refers to the conversion of measured intensities of characteristic X-rays to mass or concentration values. [56] In EDXRF, the intensity is equal to the area of a peak. In order to ensure that the net intensity used for quantitative analysis emanates from the element of interest only, the background spectrum and peak overlaps must be subtracted from the raw spectrum.

The basic procedure for quantitative analysis is to calibrate the spectrometer by measuring one or more reference material of known composition. A calibration graph is then produced which shows a relationship between the measured intensity of a

particular characteristic line and the concentration of the corresponding element in the reference material. The calibration graph is then used to determine the composition of the element of interest in unknown samples.

As a result of matrix effects, net intensities measured in XRF are not always linearly related to actual concentration [57] except in thin samples where matrix effects can be neglected. [58] Intensity does not only depend of the concentration of the originating element but also of the presence and concentration of other elements in the sample. [59], [60] This is known as the inter-element or matrix effects, which consist of absorption and enhancement effects. Incoming X-rays penetrate the sample and a portion of which is absorbed by layers of atoms above those of the element of interest. Characteristic X-rays emitted by the ionised atoms must also pass these overlying atoms in order to escape the sample, during which a part of the fluorescence is absorbed. The absorption effect relies on which elements are present and their concentrations. Generally, heavy elements absorb more than light elements.

The emission of characteristic X-rays is not only caused by the primary X-ray beam, but also by characteristic fluorescence X-rays of other atoms. Characteristic X-rays generated by the primary beam is denoted as primary fluorescence. If the primary fluorescence has sufficiently high energy, it can ionise other atoms, induce secondary fluorescence and thus, the observed X-ray intensity will be higher than expected [70].This is known as the enhancement effect. Figure 2.21 shows how matrix effects can influence the calibration curve of binary systems, i.e. samples with only two elements or compounds. Curve 1 in figure 2.21 shown an ideal linear relationship between relative intensity and weight fraction (no matrix effects). Curve 2 and 3 indicate positive and negative absorption respectively, while Curve 4 shows the effect of enhancement on the calibration graph. [61]

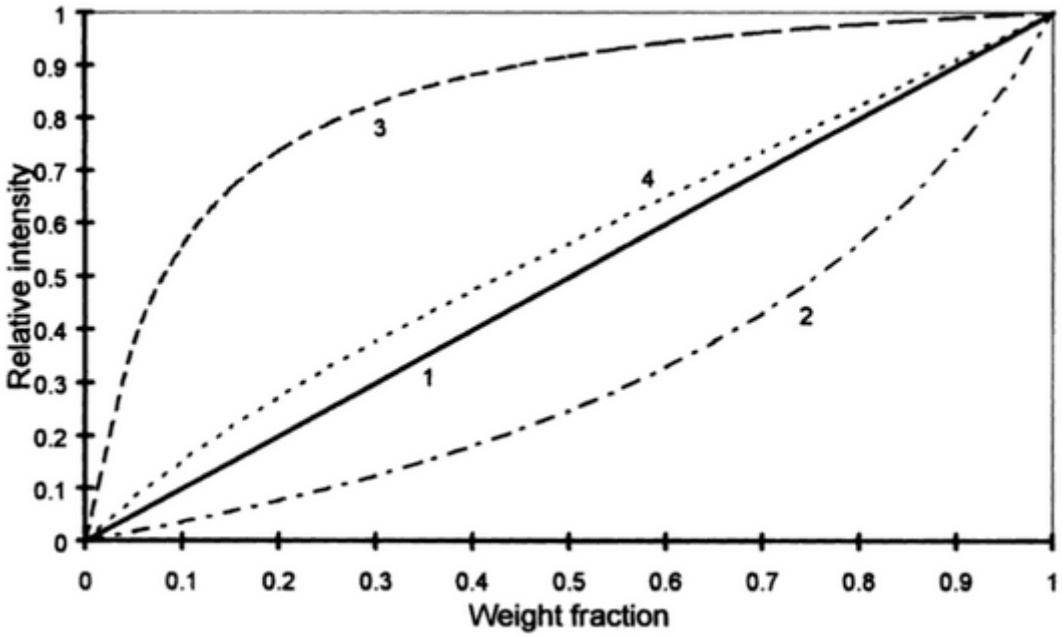

Figure 2.21: Calibration curves for binaries illustrating matrix effects in XRF

Since the early fifties, many approaches have been proposed to correct matrix effects. [62] Two popular methods are the influence coefficients method and fundamental parameters (FP) method. [63] Influence coefficients are mathematical expressions that quantify the matrix effects of a particular element and their combined net effect in a single value. [57] These coefficients can be obtained from empirical relationships or theoretical calculations. In contrast, FP is a fully theoretical quantification method which consists of calibration and iteration steps. Calibration involves calculating intensities relative to that of pure element or multi-component specimen of known composition. Iteration involves the conversion of the calculated relative intensities into concentration. The main limitation of this approach is the need to estimate the composition of each element present in a sample in order to start the iteration procedure and to normalise the concentrations prior to each iteration.

3. CHAPTER: Material and Methods

3.1. X-ray µTomo STAR-Lab

In my research work I used an X-ray microtomography station implemented at the STAR-Lab facility realized under the PON MaTeRia project, at the University of Calabria (Italy). MaTeRia is a multidisciplinary research infrastructure for services in advanced materials research. The core of this project is the Southern Europe Thomson Backscattering Source for Applied Research (STAR). It's a compact hard X-ray source for advanced applied materials-science research. Emitted from a 10 µm source, the X-rays are tunable in the 10 – 200 keV range, monochromatic and collimated. STAR has been designed for maximum adaptability, easily upgraded in terms of energy range (towards the MeV), photon flux, beam divergence and the ability to accommodate multiple simultaneously running beamlines. Compared to standard synchrotron radiation facilities, STAR offers a complementary source with high X-ray energy but at lower running costs. STAR X-rays support BEAMLINES which are custom-designed to meet specific investigation methodologies and purposes.
Currently, STAR-Lab is has been coupled with an innovative X-ray µTomo station. Its design is shown in figure 3.1, while figure 3.2 shows a picture of same apparatus.

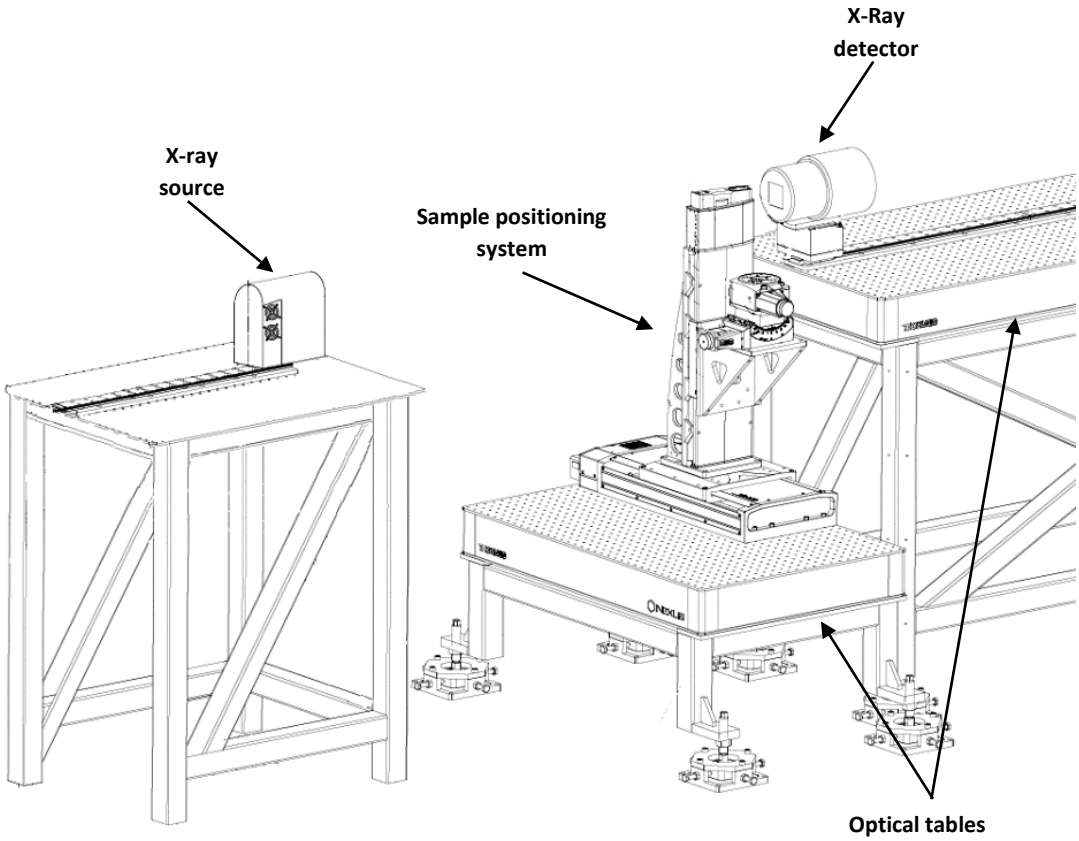

Figure 3.1: X-ray µTomo station STAR-Lab

This setup has been commissioned by Synchrotron Elettra of Trieste (Italy) and assembled in STAR-Lab. at the University of Calabria.

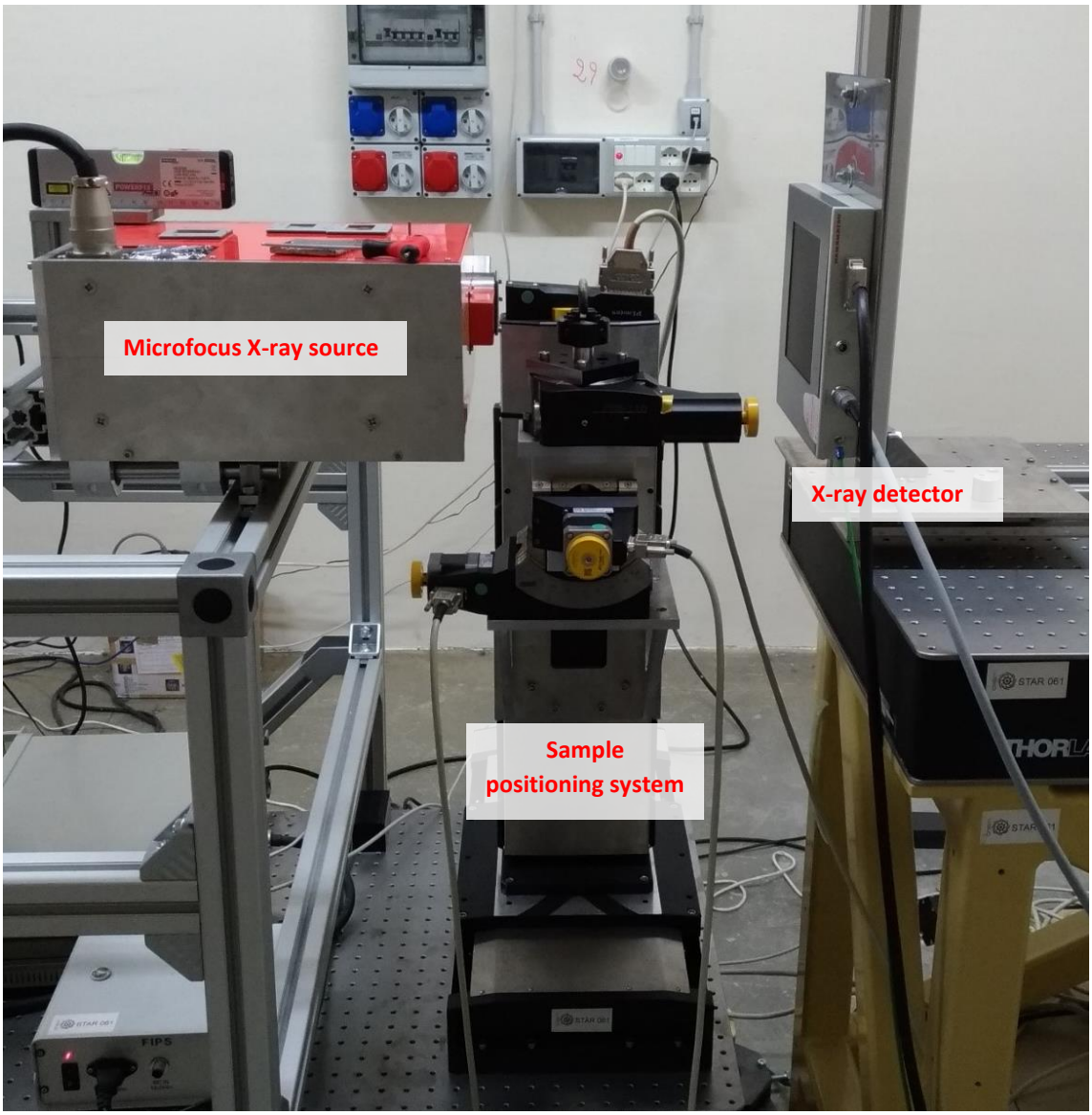

Figure 3.2: Picture of X-ray µTomo station STAR-Lab

Experimental setup consists in:

- ✓ Microfocus X-ray source Hamamatsu L12161-07
- ✓ Flat panel detector Hamamatsu C7942SK-05
- ✓ Five degree of freedom sample positioning system (linear movement and rotation stage)
- ✓ Hardware and software system for control and data acquisition

3.1.1. X-Ray source Hamamatsu L12161-07

The X-ray source is the Microfocus L12161-07 by Hamamatsu (figure 3.3).

Figure 3.3: Microfocus X-ray source Hamamatsu L12161-07 & the external control unit

It is a polychromatic microfocus transmission X-ray tube which geometry of the X-ray beam is conical with an opening angle of about 43 degrees. The target anode is made of tungsten, while the exit window is a 200nm thick beryllium sheet.

The operating voltage and the operating current of the tube can vary in a range between 40 and 150kV and a range between 10µA and 500µA respectively.

The tool can work at three focal spot size: 7µm (Small Focus Mode), 20µm (Middle Focus Mode) and 50µm (Large Focus Mode).

The maximum output power depends on the selected focus mode (Small, Middle, Large) which is 10 W, 30 W and 75W respectively. If the power is 4W, it is possible to have a nominal focal spot size of 5µm.

The main features are shown in table 3.1.

Parameter		**Value**
X-ray tube voltage setting range		0 to 150 (Kv)
X-ray tube current setting range		0 to 500 (µA)
X-ray tube voltage operational range		40 to 150 (Kv)
X-ray tube current operational range		10 to 500 (µA)
Maximum output	Small focus mode	10 W
	Middle focus mode	30 W
	Large focus mode	75 W
X-ray focal spot size (nominal value)	Small focus mode	7 µm (5 µm at 4 W)
	Middle focus mode	20 µm
	Large focus mode	50 µm
X-ray beam angle		≅ 43 degree
Focus to object distance (FOD)		≅ 17 mm

Table 3.1: X-ray source Hamamatsu L12161-07 main features

The working curve of the microfocus source Hamamatsu L12161-07 is shown in figure 3.4, from which it is possible to determine the maximum value of the tube current, once the tube voltage and the focal spot size have been set.

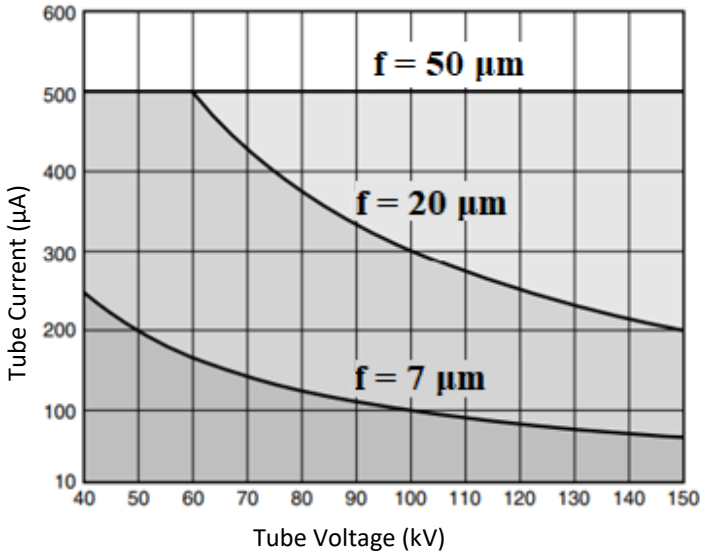

Figure 3.4: Graph of the microfocus X-ray source Hamamatsu L12161-07 working curves

Figure 3.5 shows the polychromatic X-rays spectrum generated by Hamamatsu L12161-07 X-ray sources at different acceleration potentials and plotted for a range of voltages between 1 and 150 kV, the photon counts were normalized to 1 (relative).

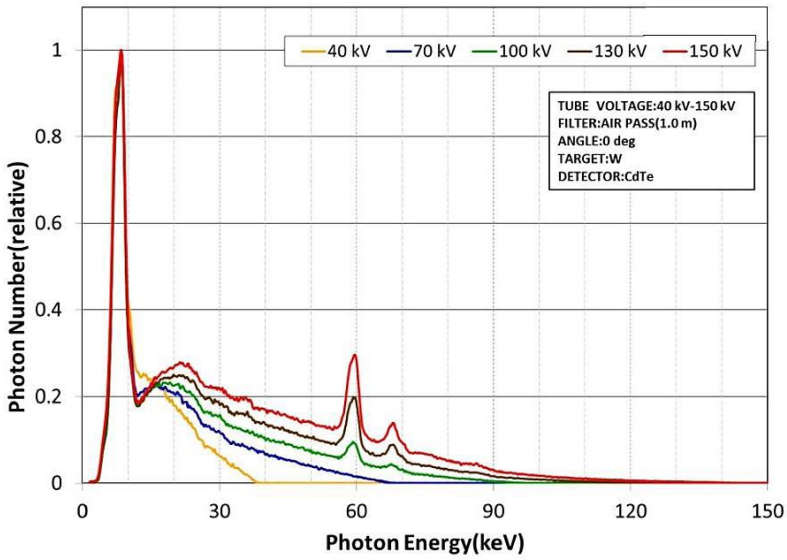

Figure 3.4: Spectra generated by microfocus x-ray sources Hamamatsu L12161-07 at different acceleration potentials and plotted for a range of voltages between 1 and 150 kV. The photon counts were normalized to 1 (relative).

3.1.2. X-ray detector Hamamatsu C7942SK-05

The detector is a Flat panel sensor C7942SK-05 from Hamamatsu (figure 3.5). It is based on two-dimensional arrays of photodiodes CMOS (CCD) directly coupled to a scintillator for X-ray to light conversion. The sensor is composed of a scintillator layer of Gadolinium oxysulfide (GOS). The detector has 2316 × 2316 active pixels, with a pixel size of 50x50 µm and the photodiode area is 120 × 120 mm. The acquired signal is sent in digital form to an acquisition card (Frame Grabber). The frame rate allows fixing the signal acquisition frequency, therefore the exposure period, in a range between 0.2 and 9 fps (frames per second).

Figure 3.5: X-ray detector Hamamatsu C7942SK-05

The main features are shown in table 3.2.

Parameter	**Specification**
Pixel size	50 X 50 (µm)
Photodiode active area	115 X 115 (mm)
Number of active pixel	2316 X 2316 (pixels)
Energy range	Max 150 kVp
High quality image	5.4 Mpixels
Digital output	12 bit
Scintillator	GOS

Table 3.2: X-ray detector Hamamatsu C7942SK-05 main features

Moreover, the software for image acquisition control then allows you to select the number of radiographic images or projections.

3.1.3. Sample positioning system

The sample position system consists of five motors by miCos Physik Instrumente, each of these provides one degree of freedom.

As shown in figure 3.5:

- ✓ 1 position: PRS-110 Precision Rotation Stage model, corresponds to the **ω** rotation angle;
- ✓ 2 and 3 positions: WT-90 Goniometer models, corresponds to the **θ** and **φ** tilt angles;
- ✓ 4 position: LS-180 Linear Stage for Heavy Loads model, corresponds to the **y** axis

✓ 5 position: LS-270 Linear Stage for Very High Loads model, corresponds to the **x** axis.

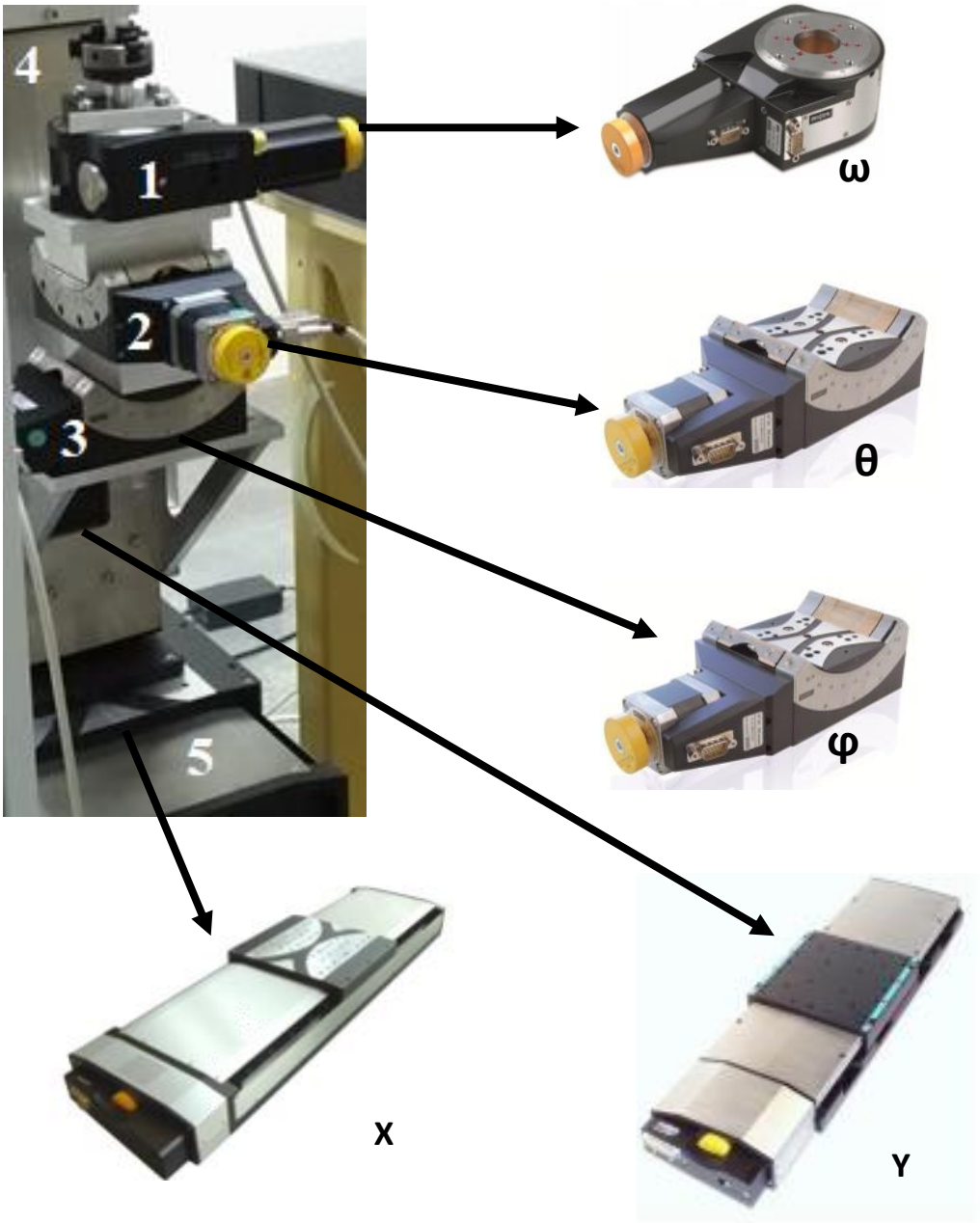

Figure 3.5: Sample positioning system

This equipment can work in open loop, excellent holding torque and low speeds, low maintenance (brushless), very rugged in any environment, excellent for precise

positioning control and no tuning required.

Table 3.3 shows the main features of the stepper motor positioners.

Specification	Pi-Micos Model				
	LS-270 (X)	**LS-180 (Y)**	**WT-90 (θ)**	**WT-90 (φ)**	**PRS-110 (ω)**
Load Capacity (Kg)	150	100	8	8	10
Load Capacity (N)	1500 (Fz)	200 (Fy)	80 (Fz)	80 (Fz)	100 (Fz)
Travel range	205 mm	155 mm	90° (max)	90° (max)	>360°
Bi-direc. Repeatability (down to)	0.05 µm	0.05 µm	0.001°	0.001°	0.0002°
Maximum speed (mm/s)	150	200	15	15	200

Table 3.3: main features of the stepper motor positioners

3.1.4. Software system

The µTomo software was developed using LabVIEW to control the hardware by means of a graphical user interface (GUI). LabVIEW is a graphical programming language. It has a powerful function library and an easy-to-use multithreaded programming and graphical user interface (GUI) design. The availability of drivers, debugging, and other features make it an ideal software for instrument-oriented programming.

The developed software is flexible allowing easy changes or additions of the hardware. The RS232 serial interface is the communication standard for most of the used laboratory equipment (Microfocus X-ray source and motors).

Figure 3.6 shows the connection diagram for the remote control of the µTomo station, instead figure 3.7 shows the front panel of the main program.

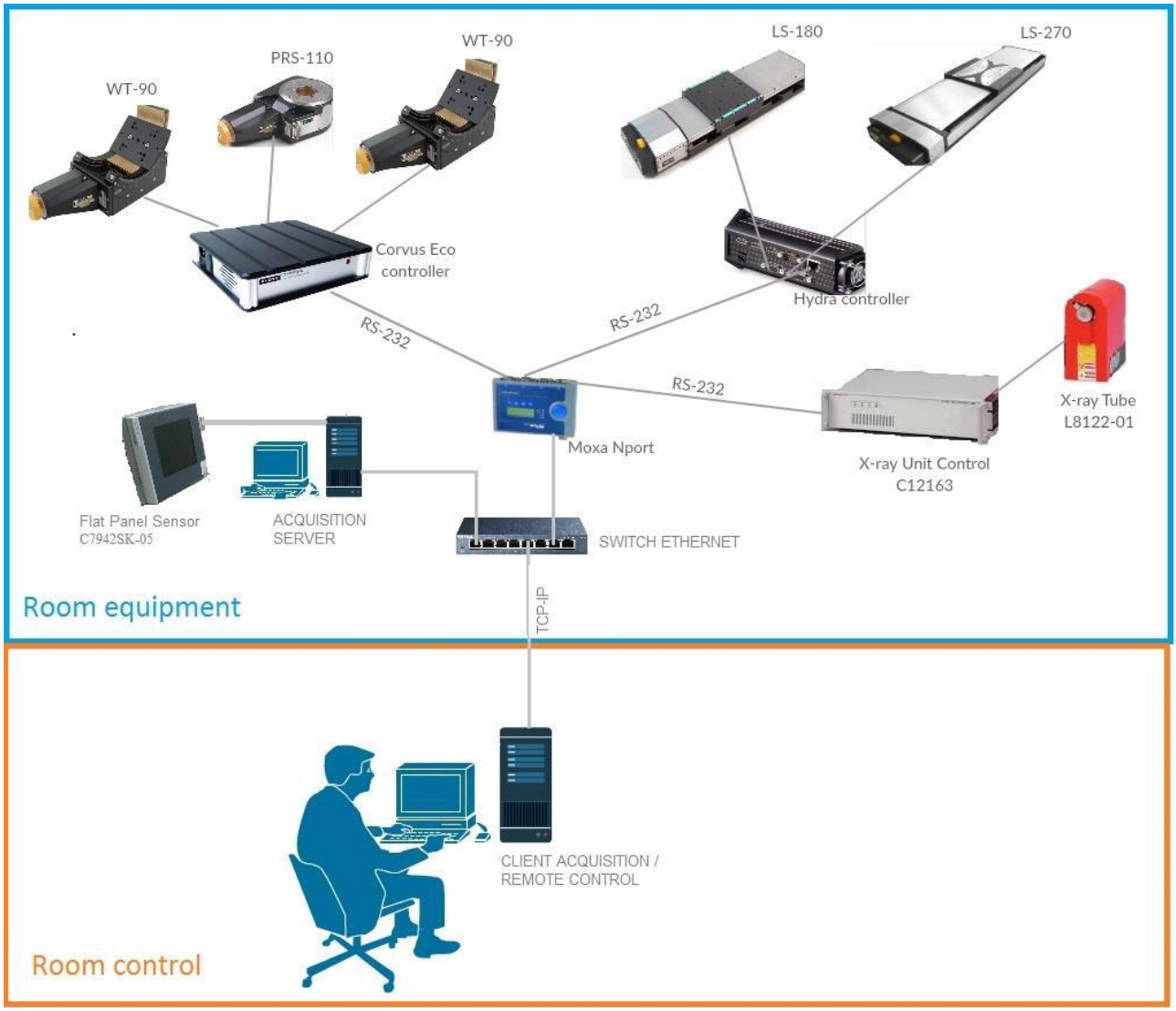

Figure 3.6: Sample connection diagram for the remote control of the µTomo station

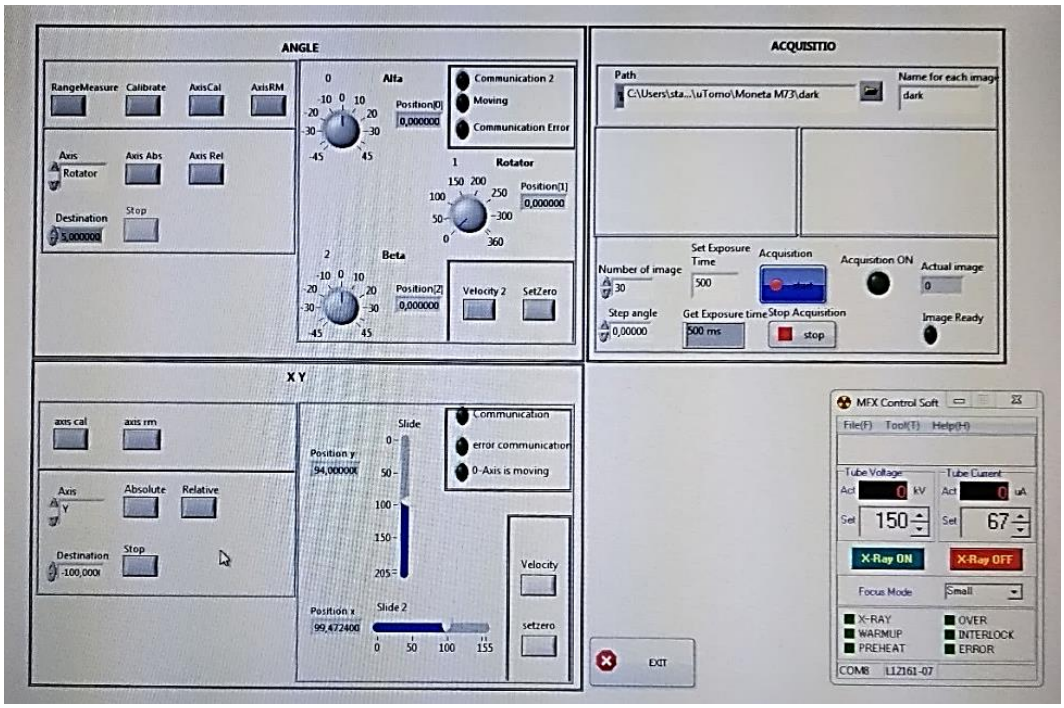

Figure 3.7: front panel of the main program

3.1.5. Image analysis

Image analysis was performed with Fiji (Fiji Is Just ImageJ) an image processing package based on ImageJ. ImageJ is an open source software developed by the National Institutes of Health of the United States, which allows digital image processing operations. [64]

ImageJ is designed with an ″open architecture″ that provides the possibility to install extensions via small subprograms "Java plugin" and the possibility to develop many macros for ad-hoc processing.

3.2. Bruker Artax 400

The surface chemical analysis of archaeological finds were carried out by the Artax 400, an portable Micro-XRF spectrometer by Bruker Corporation. It is designed for non-destructive elemental analysis and it works in an energy dispersive method (ED-XRF).

Its picture is shown in figure 3.8.

Figure 3.8: Portable Micro-XRF spectrometer Artax 400 by Bruker Corporation

The main components are:

- ✓ Measuring head with:
    - X-ray radiation source
    - X-ray detector
    - X-ray optics
    - CCD camera
    - Laser pointer
    - Collision sensor

- ✓ XYZ adjustment
- ✓ Tripod with arms and floating arms
- ✓ Electronic unit
- ✓ Terminal
- ✓ Measurement computer
- ✓ Helium flushing system

Main components are shown in figure 3.9.

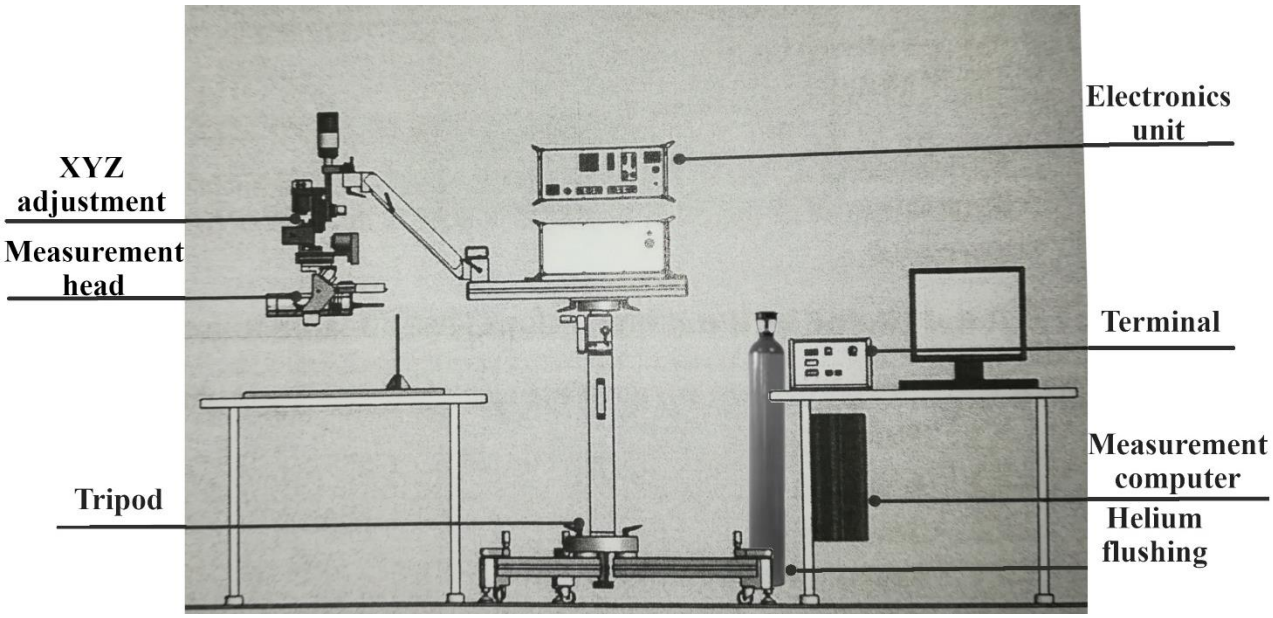

Figure 3.9: Artax 400 main components

3.2.1. Measurement head

The measurement head consists essentially in X-ray source and X-ray detector, as shown in figure 3.10.

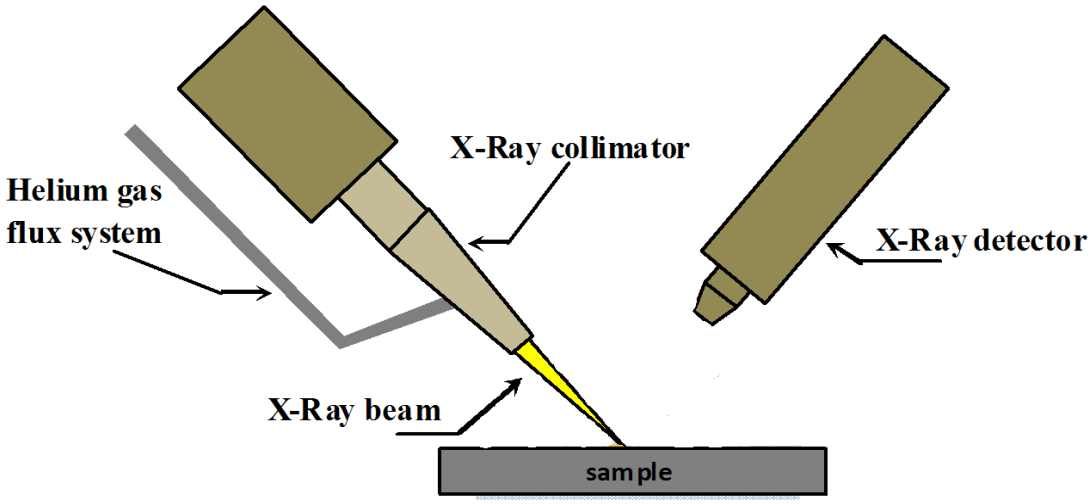

Figure 3.10: Artax 400 measurement head

The X-ray source is a mini-focus tube with, the target anode is made of molybdenum and the exit window is a 100µm thick beryllium sheet.

The operating max voltage and the operating max current of the tube are 50kV and 1000µA respectively, for a max power of 50 W.

The X-ray beam is restricted by a series of collimators, with a lateral resolution of 200 µm, 650 µm, 1 mm and 1.5 mm.

The X-ray tube emits a polychromatic beam whose spectral characteristics are determined primarily by the elements of the X-ray target and the value of the high voltage present. After the interaction of X-ray radiation with the object under examination, the spectrum registered contains not only the sample specific fluorescence radiation, but also a considerable share of scattered primary radiation. The scattered excitation radiation is generally a disturbance signal. Using a thin metal foil filter which absorbs certain low-energy ranges or emission lines of the excitation spectrum, is one way for suppressing this effect. The Artax 400 has an exchangeable filter slide with three position: position 1 is empty, position 2 and 3 are occupied with aluminium foil of different thicknesses.

The spectrometer Artax 400 enables determination of chemical elements with lower atomic number using a helium flushing which generating a modified atmosphere between X-ray beam and sample.

Figure 3.11 shown various excitation spectra of Artax 400's Mo X-ray tube. It is apparent as to how the He flush clearly improves the transmission of the Mo-L line and how an aluminium filter (600 µm thickness) contributes to a weakening of a low-energetic part of the excitation spectra. Therefore filters always have the effect of a reduction of the subsurface in the spectrum. At the same time, a filter means the reduction of the excitation intensity and hence a lowering of the fluorescence intensity.

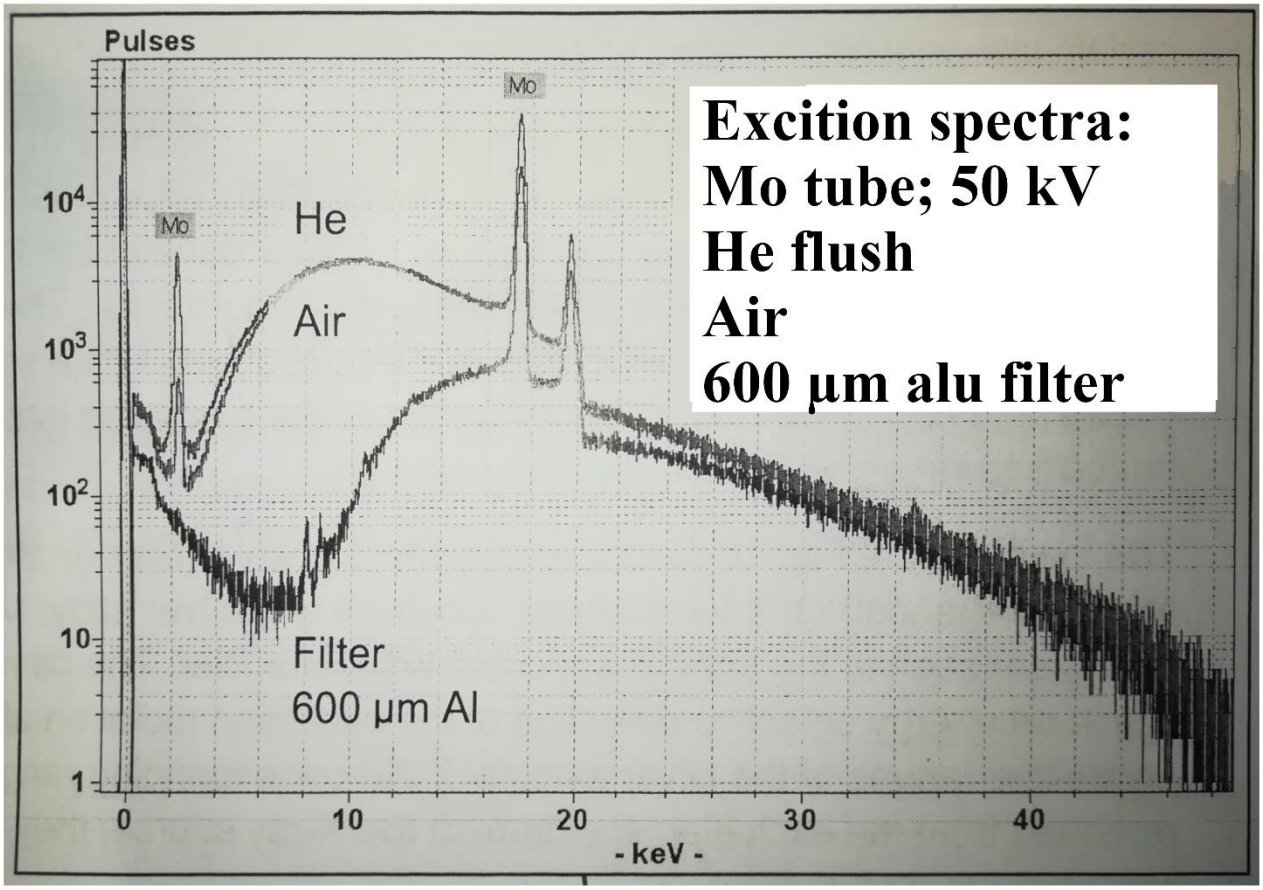

Figure 3.11: excitation spectra of Artax 400's Mo X-ray tube: in modified atmosphere (with He flush); in air; with 600 µm Al filter

The Artax 400's detector belongs to the XFlash devices family, based on silicon semiconductor drift (SDD) technology with a Peltier cooling system. Useful area of 10 mm^2, resolution <155 eV at 10 kcps and maximum count rate up to 100 kcps.

Spectra 7 is an in house Bruker software for acquiring and evaluating XRF spectra acquired by Artax 400. Thanks to the characteristic X-ray emitted from the sample, it was possible to get out the atomic concentration of the sample by comparing it with a reference sample having a well-known atomic concentration, using the formula:

$$C_i = \frac{N_i}{T * I * K_i}$$

Where: C_i= concentration of the element; N_i= total count; T= time (s); I= current intensity (μA); K= calibration factor.

4. CHAPTER: Case studies

4.1. Case study 1

Silver plated Greek and Roman coins from the “Brettii and Enotri” museum: a non-destructive archaeometric study

4.1.1. Introduction

The plated coins are made up of a core of base metal (planchet or flan), like copper, but also tin and lead, pure or as alloy, coated with a layer of precious metal such as gold or silver. These coins were widespread since classical antiquity but mostly in republican and first imperial Rome. [65] The production of plated coins was very cost-effective. In fact, during the Republican period, 1 gram of silver was purchased with 240 grams of copper. The production of plated coins and their circulation, therefore, took place through counterfeiters, but some theories say that in republican Rome, the creation and the issue of these coins were authorized by the State, perhaps to deal with a series of economic problems in the republic. [65]

The methods used since ancient times for gilding or silvering objects are varied and were used on jewels, statues, coins of low-value materials by giving them the appearance of silver or solid gold. [66]–[70]

One of the most used methods for silver plating coins consisted in the plastic processing of the planchet (also known as flan) to give it the right shape, size and weight. Then, the planchet is minted. The surface was first sandblasted to eliminate any oxides and then the silver leaf was applied by cold compression. At the end of the process, it was necessary to ensure the optimal adhesion and the absence of air bubbles that would have triggered oxidation processes, therefore damaging the

metals making up the coin core. The coated disk was thus brought close to the melting temperature of the silver (961.8 °C). So, the precious metal could firmly and uniformly coat the flan by creating an interpenetration between the interface of the two metals. Other widely used methods are the deposition by immersion in the molten precious metal and the deposition by mercury amalgam. The coating produced was very resistant to wear, making the counterfeiting work difficult to notice and allowing the circulation of plated coins even for long periods of time. [65], [66], [71]–[74]

In this case study, the results of the chemical-physical investigations performed on three silver-plated coins from the Chiaia Collection of the Brettii and Enotri museum in Cosenza will be discussed. We examined a Greek stater coin and two Roman denarius coins present in the Museum Coins Collection catalogue [75] as M106 (figure 4.1.1), M114 (figure 4.1.2) and M115 (figure 4.1.3) respectively.

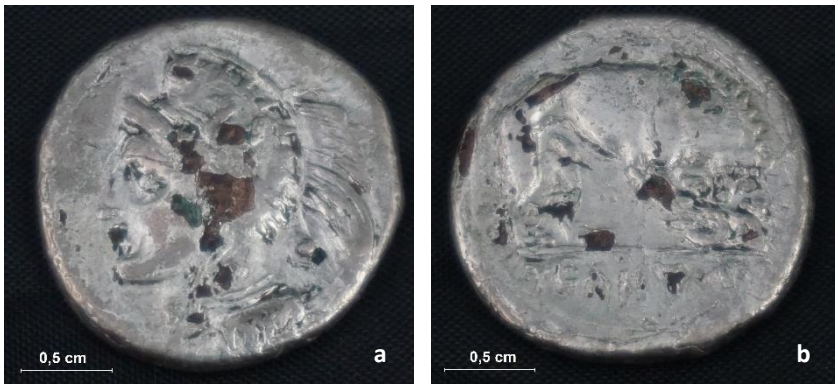

Figure 4.1.1: Obverse (a) and reverse (b) of the M106 stater coins

Figure 4.1.2: Obverse (a) and reverse (b) of the M114 denarius coin

Figure 4.1.3: Obverse (a) and reverse (b) of the M115 denarius coin

The aims of this work is the chemical and morphological study in order to find peculiarities for hypothesize the production process and the construction technologies. Chemical elements are studies by XRF spectrometer, however morphological studies of the surface covering layer and the interface between the base metal and precious metal carry out by X-ray microtomography and scanning electron microscope.

For first approach, the surface of the coins was examined under an optical microscope.

4.1.2. Optical microscope

Figures 4.1.4, about an area of the obverse of the M106 coin, shows a pyramidal section hole, probably intentionally made in Greek period to verify its authenticity. Figure 4.1.5 shows a small area of the reverse of the M106 coin in which are visible a crack in correspondence of two overlapping silver layers.

Figure 4.1.6, about the edge of the same coin, shows the high thickness of the surface silver layer.

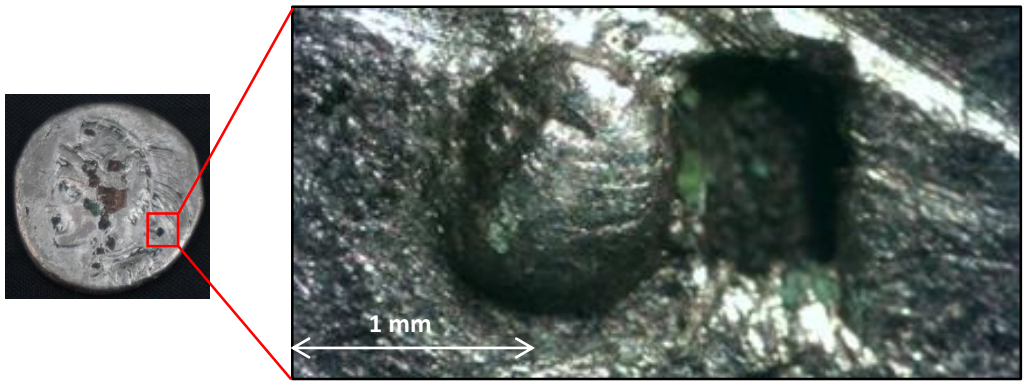

Figure 4.1.4: A detail of the obverse of the M106 coin showing the pyramidal section hole

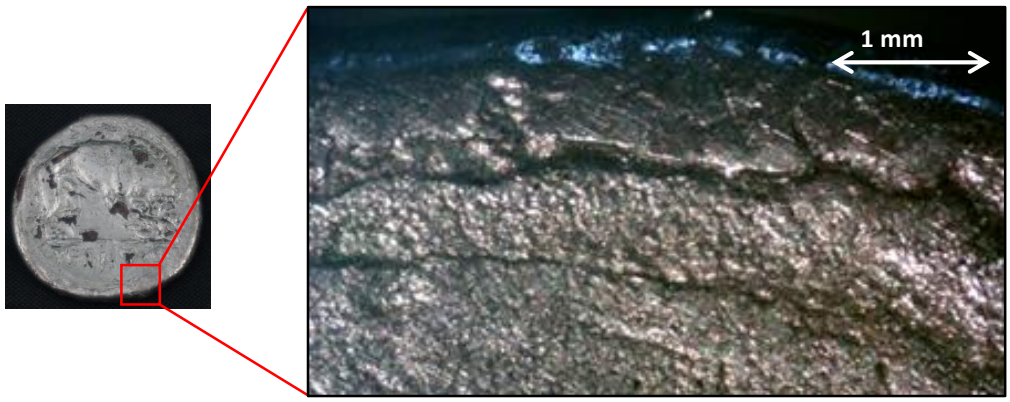

Figure 4.1.5: Crack and overlap of silver layers in a small area near the edge of the reverse of the M106 coin

Figure 4.1.6: Detail from the edge of the M106 coin in which overlapping of silver layers is evident

Figures 4.1.7 and 4.1.8 show an area of the obverse and an area of the reverse of the M114 coin respectively. In the first case an evident thinning of the silver layer is visible, while the second figure shows the silver layer lifting. Similarly, the obverse of the M115 coin in figure 4.1.9 has the same morphological characteristics as the M114 coin.

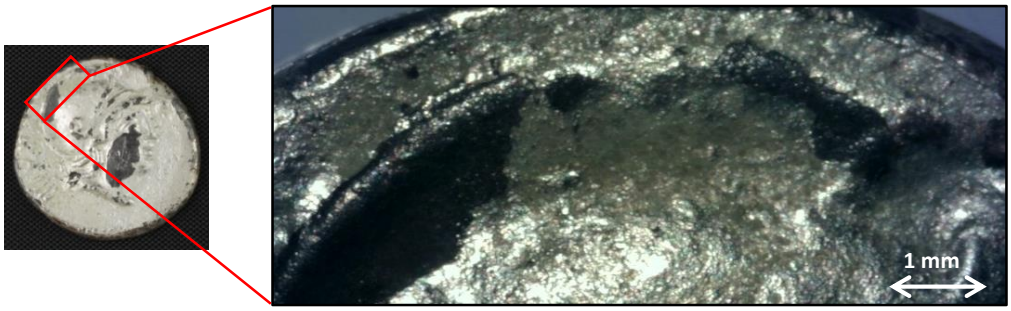

Figure 4.1.7: Detail of the obverse of the M114 coin showing the thinning of the silver layer

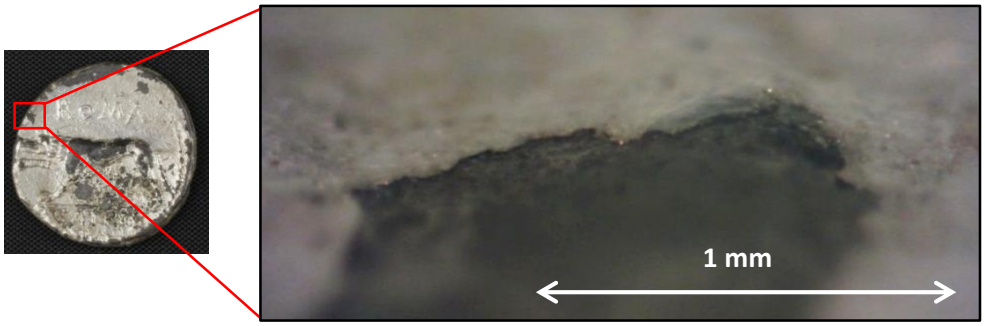

Figure 4.1.8: A particular from the reverse of the M114 coin displaying the lifting of the silver layer from the substrate

Figure 4.1.9: Detail of the obverse of the M115 coin pointing out the thinning of the silver layer and lifting of it from the substrate

4.1.3. X-ray fluorescence spectroscopy

The XRF chemical investigation was performed to detect the planchet chemical nature and to confirm the chemical nature of the silver covering layer. For each coin, four measurement points were chosen: two on the silver layer and two on the planchet surface (as shown in figures 4.1.10, 4.1.11, 4.1.12). The pairs of measures were averaged between them.

The parameters used to perform the XRF measurements are shown in table 4.1.1.

Energy	50 keV
Voltage	50 kV
Current	700 µA
Collimator	0.65 mm
Exposition time	1200 s

Table 4.1.1: XRF measurements parameters

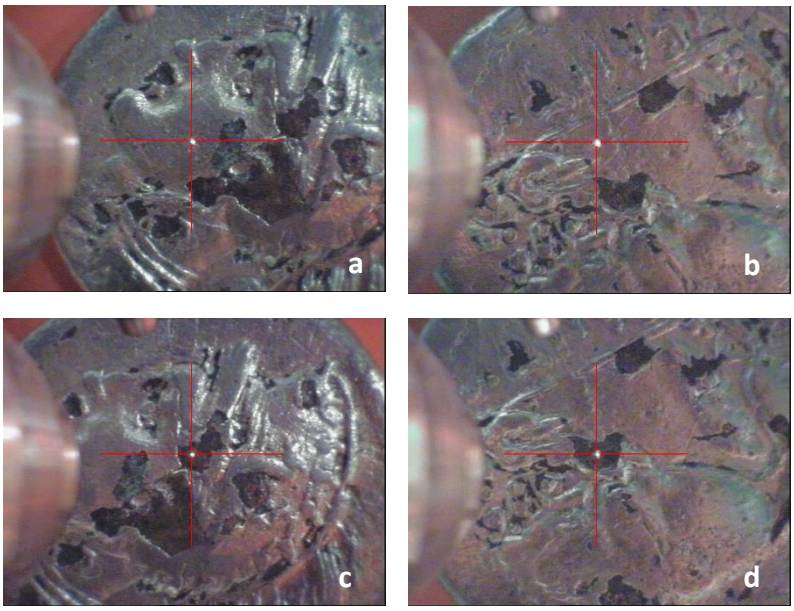

Figure 4.1.10: XRF measuring points on the M106 coin's silver layer (a-b) and flan (c-d)

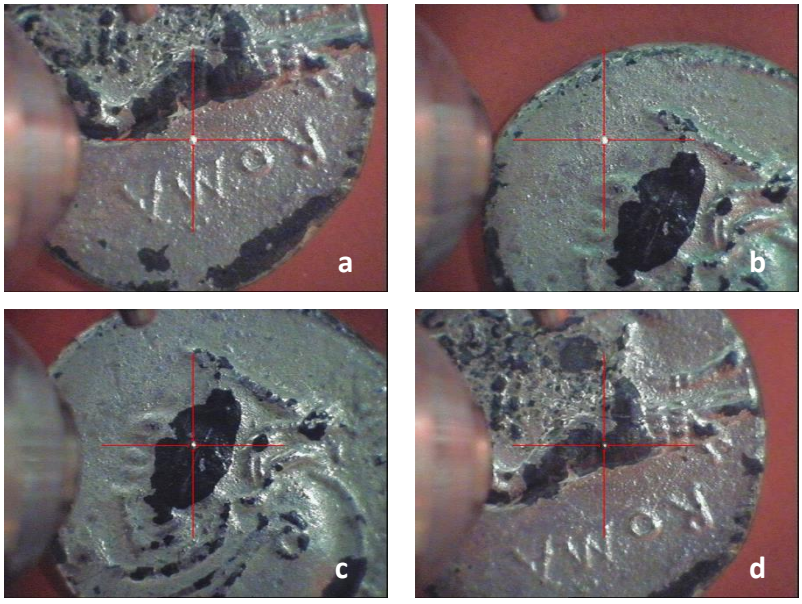

Figure 4.1.11: XRF measuring points on the M114 coin's silver layer (a-b) and flan (c-d)

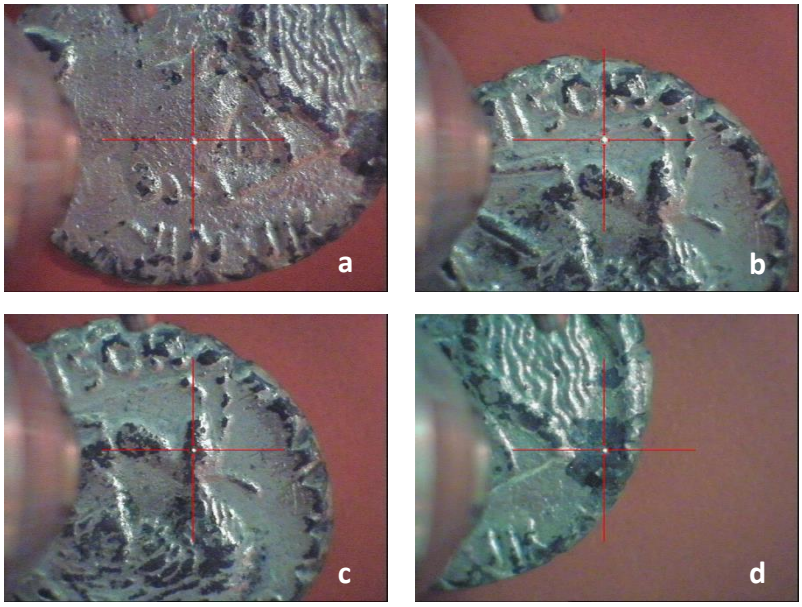

Figure 4.1.12: XRF measuring points on the M115 coin's silver layer (a-b) and flan (c-d)

The XRF spectra about M106 coin's silver layer and flan are shown in figure 4.1.13a and 4.1.13b respectively. However, the relative atomic concentrations of the chemical elements are shown in table 4.1.2.

We can confirm the silver nature of the coating layer. It is made approximately 98% silver with presence of secondary elements as gold (0.31%), lead (0.27%), zirconium (800 ppm), nickel (200 ppm), zinc (100 ppm) and tin (100 ppm), while titanium, iron, rubidium and bismuth are present below 100 ppm. The presence of Copper (1.73%) may be due to the planchet contribution.

The planchet measurements revealed a copper presence (84.43%) and other secondary elements as tin (1.40%), chlorine (0.33%), lead (0.22%), zinc (0.21%), potassium (300 ppm), iron (300 ppm) and arsenic (200 ppm), while chromium, cobalt, strontium and bismuth are present below 100 ppm. The silver (13.36%) could be due to interdiffusion phenomena between the layers of silver and copper created during the plating process. [65], [76] We can therefore consider that the coin's core is made almost exclusively of copper.

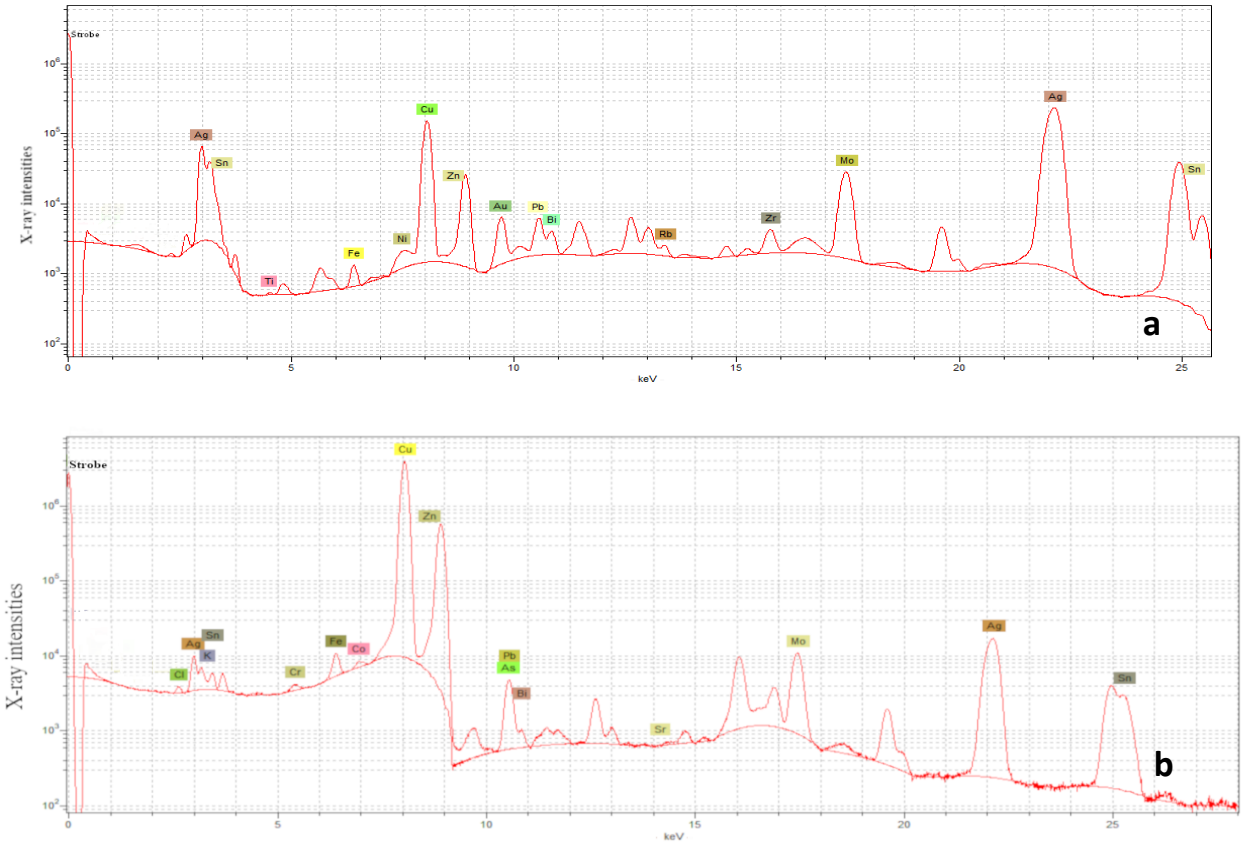

Figure 4.1.13: XRF spectra in logarithmic scale of the elements present on the M106 coin's silver layer (a) and flan (b)

N.	Element	Silver layer Conc. (%)	Flan Conc. (%)
1	Ti K_α	<0.01	----------
2	Cl K_α	----------	0.33 ± 0.15
3	K K_α	----------	0.03 ± 0.03
4	Cr K_α	----------	<0.01
5	Fe K_α	<0.01	0.03 ± 0.01
6	Co K_α	----------	<0.01
7	Ni K_α	0.02 ± 0.01	----------

8	Cu K_α	1.73 ± 0.10	**84.43 ± 1.00**
9	Zn K_α	0.01 ± 0.01	0.21 ± 0.04
10	Rb K_α	<0.01	----------
11	Zr K_α	0.08 ± 0.01	----------
12	As K_α	----------	0.02 ± 0.01
13	Sr K_α	----------	<0.01
14	Ag K_α	97.59 ± 0.06	13.36 ± 0.71
15	Sn K_α	0.01 ± 0.01	1.40 ± 0.15
16	Au K_α	0.31 ± 0.01	----------
17	Pb L_α	0.27 ± 0.03	0.22 ± 0.01
18	Bi L_α	<0.01	<0.01

Table 4.1.2: atomic concentrations of the elements present on the M106 coin's silver layer and flan

The XRF spectrum of the M114 coin's silver layer is shown in figure 4.1.14a, however the XRF spectrum of the flan is shown in figure 4.1.14b. The relative atomic concentrations of the chemical elements about M114 coin's silver layer and flan are shown in table 4.1.3.

The study of the spectra shows that the coating layer contains 42.95% silver, 31.74% tin, 21.28% antimony, 2.40% zinc and 1.34% lead and other secondary elements as copper (0.15%), zirconium (0.12%) and nickel (400 ppm), while iron, cobalt, arsenic and bismuth are present below 100ppm. The planchet measurements revealed a tin (51.88 %) and antimony (41.99%) alloy and other secondary element as zinc (2.64%),

lead (2.38%), zirconium (0.15%), silver (0.91%) and copper (700 ppm), while iron, arsenic, gallium and bismuth are present below 100 ppm.

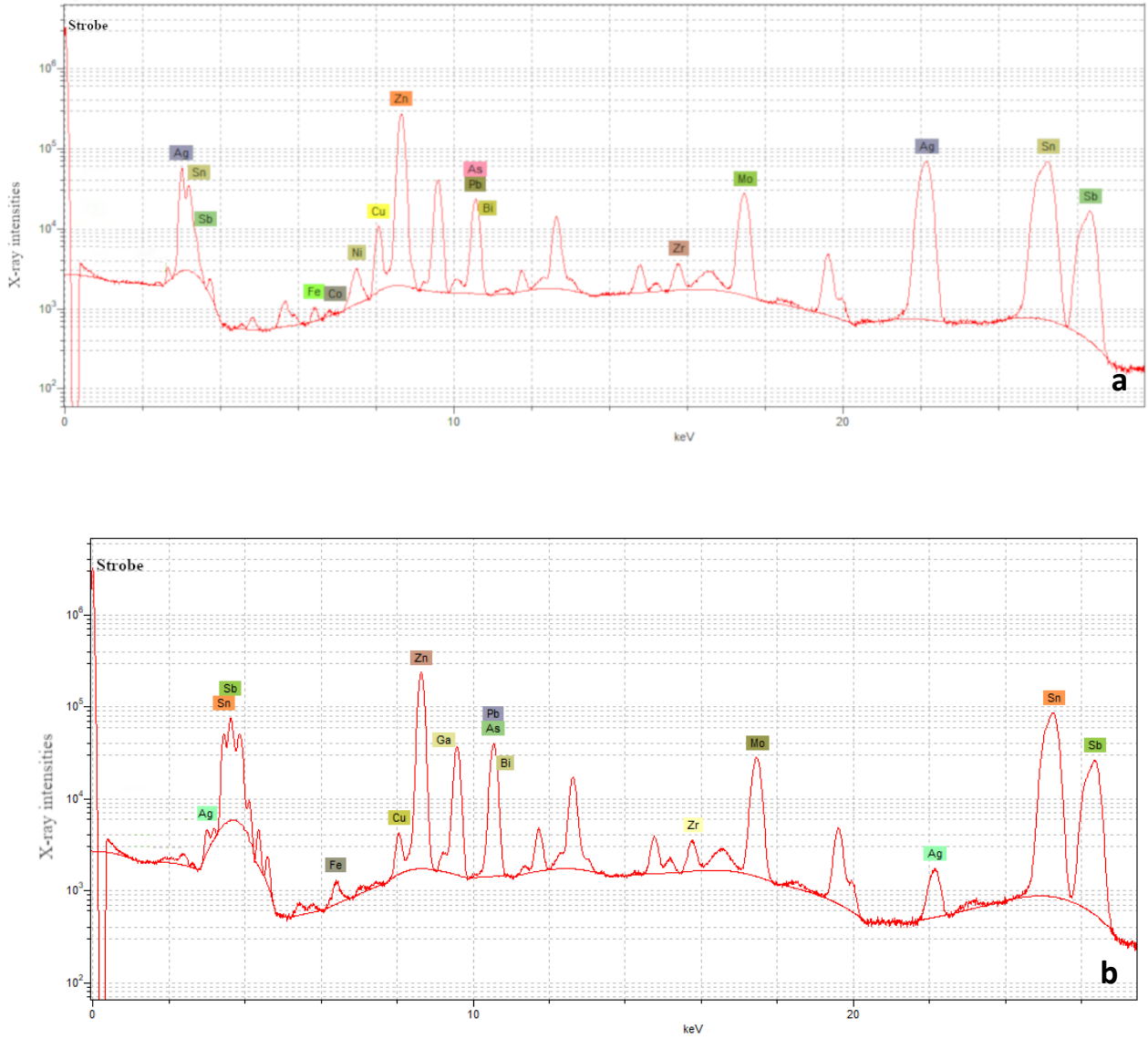

Figure 4.1.14: XRF spectra in logarithmic scale of the elements present on the M114 coin's silver layer (a) and flan (b)

N.	Element	Silver layer Conc. (%)	Flan Conc. (%)
1	Fe Kα	<0.01	<0.01

2	Co Kα	<0.01	----------
3	Ni Kα	0.04 ± 0.01	----------
4	Cu Kα	0.15 ± 0.12	0.07 ± 0.03
5	Zn Kα	2.40 ± 1.60	2.64 ± 0.28
6	Ga Kα	----------	<0.01
7	As Kα	<0.01	<0.01
8	Zr Kα	0.12 ± 0.01	0.15 ± 0.01
9	Ag Kα	**42.95 ± 5.70**	0.91 ± 0.81
10	Sn Kα	31.74 ± 3.59	**51.88 ± 0.01**
11	Sb Kα	21.28 ± 3.69	**41.99 ± 0.25**
12	Pb Lα	1.34 ± 0.15	2.38 ± 0.30
13	Bi Lα	<0.01	<0.01

Table 4.1.4: atomic concentrations of the elements present on the M114 coin's silver layer and flan

The XRF spectra of the M115 coin's silver layer and flan are shown in figure 4.1.15a and 4.1.15b respectively. However, the relative atomic concentrations of the chemical elements are shown in figure and in table 4.1.5.

The study of the spectra shows that the coating layer contains 30.94% silver, 40.85% tin, 21.29% antimony, 4.21% zinc and 2.38% lead and other secondary elements as copper (0.14%), zirconium (0.14%) and nickel (700 ppm), while iron, cobalt, arsenic and bismuth are present below 100ppm. The planchet measurements revealed a tin (57.50 %) and antimony (34.19%) alloy and other secondary element as zinc (2.89%), lead (2.48%), zirconium (0.16%) and copper (700 ppm), while iron, arsenic, gallium and bismuth are present below 100 ppm. The silver (2.73%) could be a residue of the coating layer.

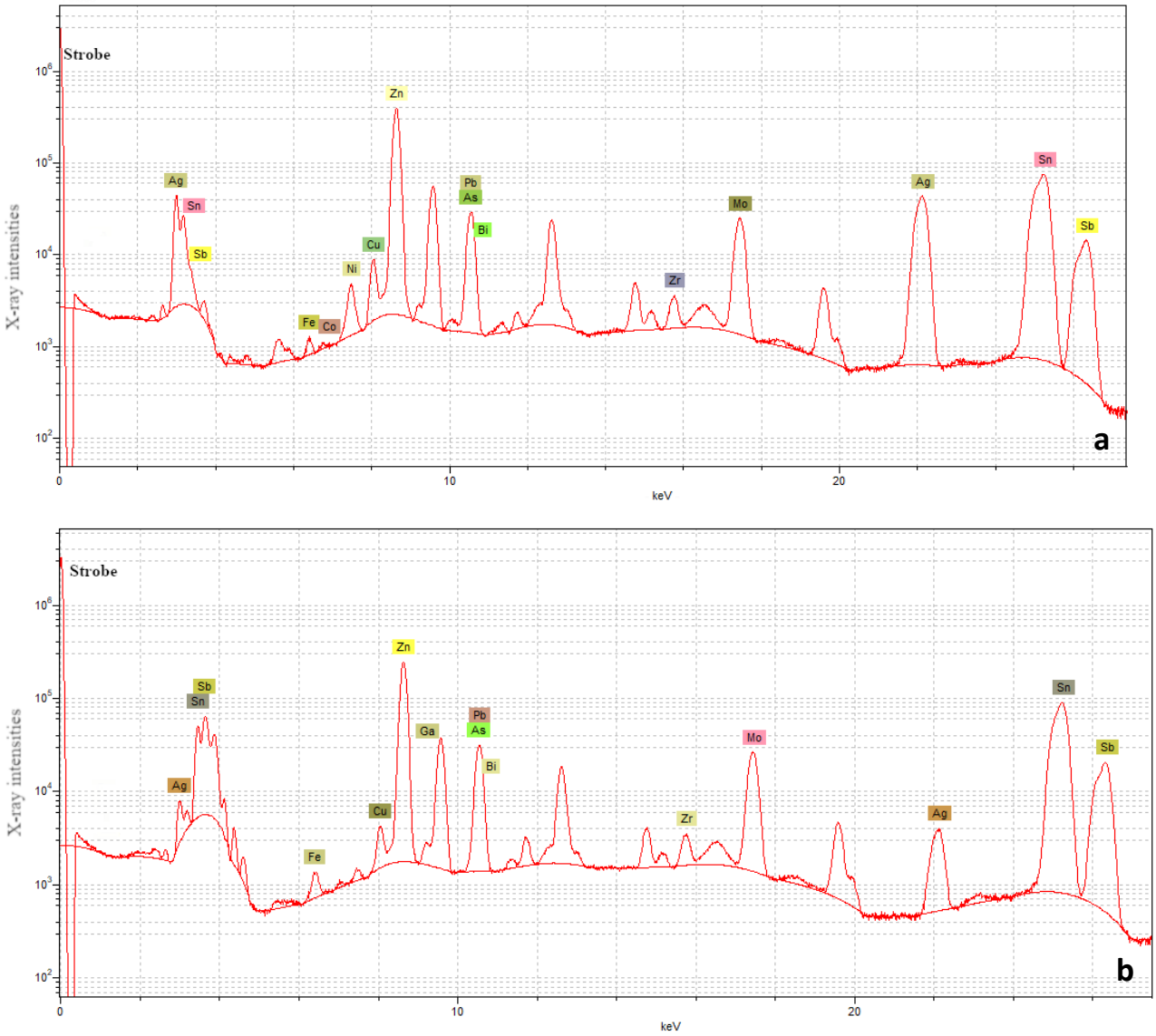

Figure 4.1.15: XRF spectra in logarithmic scale of the elements present on the M115 coin's silver layer (a) and flan (b)

N.	Element	Silver layer Conc. (%)	Flan Conc. (%)
1	Fe Kα	<0.01	<0.01
2	Co Kα	<0.01	----------

3	Ni Kα	0.07 ± 0.04	----------
4	Cu Kα	0.14 ± 0.12	0.07 ± 0.01
5	Zn Kα	4.21 ± 3.72	2.89 ± 0.68
6	Ga Kα	----------	<0.01
7	As Kα	<0.01	<0.01
8	Zr Kα	014 ± 0.01	0.16 ± 0.01
9	Ag Kα	**30.94 ± 9.07**	2.73 ± 1.12
10	Sn Kα	40.85 ± 2.75	**57.50 ± 1.18**
11	Sb Kα	21.29 ± 2.72	**34.19 ± 0.65**
12	Pb Lα	2.38 ± 0.26	2.48 ± 0.03
13	Bi Lα	<0.01	<0.01

Table 4.1.5: atomic concentrations of the elements present on the M115 coin's silver layer and flan

In M115 and M114 coins the ratio of antimony and tin concentration on the flan surface to antimony and tin concentration on the silver surface is very similar. Furthermore, the silver layer of both coins made with a thickness of approx 25 µm (see the SEM investigation in paragraph 4.1.5). This evidence suggests that X-ray beam can penetrate the covering layer and detect the elements present below. [77] So, to determine the real composition of the covering layer, for both coins, the flan contribution was subtracted. Therefore, it can be stated that the M114 and M115 coins are covered with an almost purest silver thin layer.

The use of Sn-Sb alloy for the realization of the core is very rare in ancient objects and there are little data reported in the literature, [73] while its use in the production of silver imitation coins is found in the denarius of A. Plautius (54 BC). [78]

4.1.4. X-ray microtomography

The X-ray microtomography surveys of the M106, M114 and M115 samples showed a series of peculiarity non-appreciable by visual investigations.

The measurements parameters are shown in table 4.1.6.

Voltage	150 KV
Current	66 µA
Exposure time for each projection	1 s
Focal spot	middle
Magnification	4
Pixel size	12.5 µm
Number of projections	1805
Step	0.2°

Table 4.1.6: X-ray microtomography measurements parameters

Figure 4.1.16 shows a slice of the M106 coin's microtomography reconstruction in which an uneven thickness silver layer is visible. At the coins face the silver layer thickness varies between 100 µm and 170 µm. In correspondence to the coin edge the thickness is almost double (200-300 µm), that can be seen in grayscale 3D rendering modified by segmentation process shown in figure 4.1.17 . In the same image you can see that the thickness of the silver coating along the edge decreases in the axial direction.

The yellow arrows in figure 4.1.16 and figure 4.1.18 show darker areas between the silver layer and the copper core. These low-absorption areas are probably due to the presence of copper oxides between the surface layer and the core. The red arrows in figure 4.1.18 show two overlapping silver layers separated by a low-absorption area.

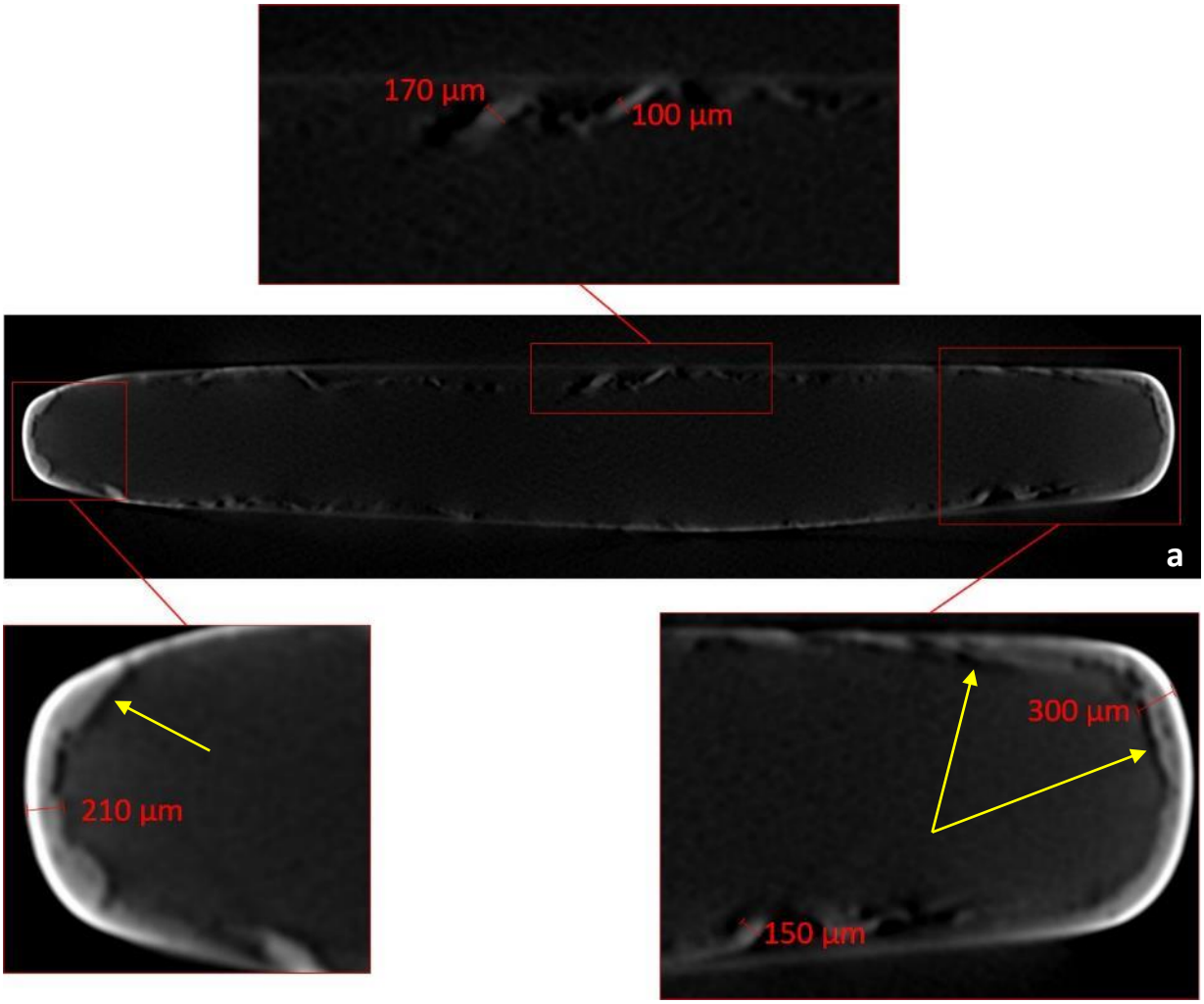

Figure 4.1.16: M106 coin's grayscale slice (a). The silver layer thickness and low-absorption areas between the silver layer and the copper core (yellow arrows) are shown

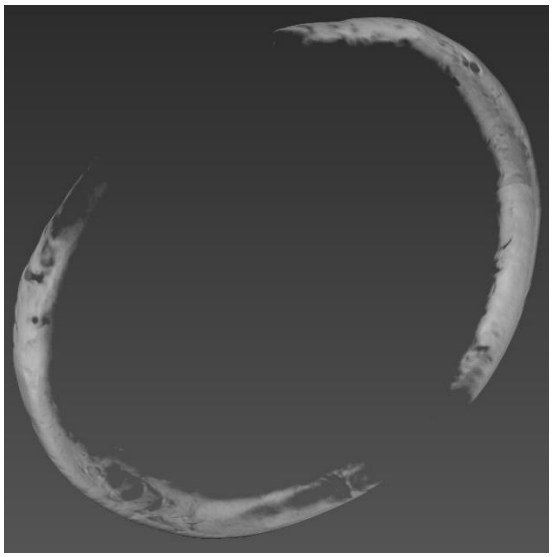

Figure 4.1.17: M106 coin's grayscale 3D rendering modified by segmentation process

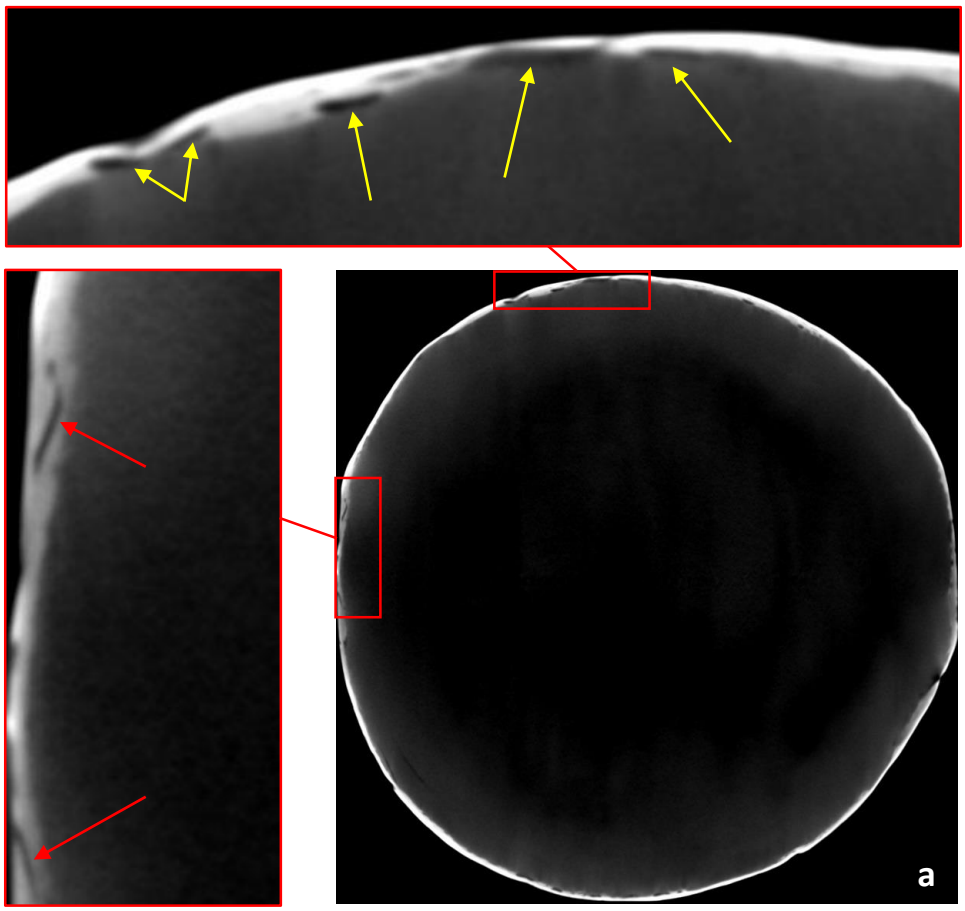

Figure 4.1.18: M106 coin's grayscale slice (a). Low-absorption areas between the silver layer and the copper core (yellow arrows) and two overlapping silver layers separated by a low-absorption areas (red arrows) are shown

Figure 4.1.19a shows a false colours slice of the M106 coin's microtomography reconstruction in which the double silver layer near the edge of the coin edge is clearly visible . The same area is shown in 3D rendering cross-section (figure 4.1.20b). The grey level histogram shown in figure 4.1.19c was acquired at the yellow line in figures 4.1.20a and b. By histogram study it is possible to deduce the separation thickness between the silver layers, which is about 25 µm.

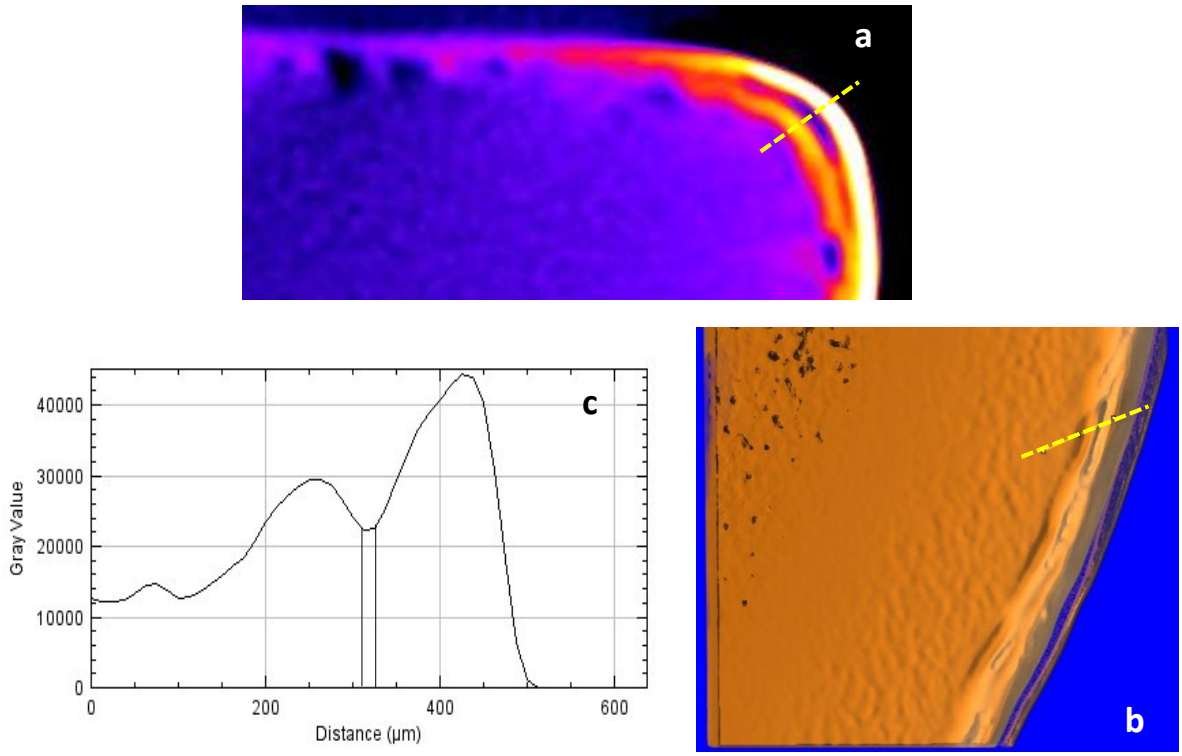

Figure 4.1.19: False colours slice of the tomographic reconstruction (a) and 3D rendering cross-section (b) in which the double silver layer near the edge of the coin is clearly visible ; grey level histogram acquired along the profile indicated by the yellow line in which it is possible value the separation thickness between the double silver layer, which is about 25 µm_M106 coin

The microtomography analysis performed on the M106 sample also revealed an internal lesion presence. It is located near the edge, it follows the coin circular form and involves the silver layer (figure 4.1.20a and b). We hypothesize that the lesion

was made due to the high stress underwent during the coining process that occurred after the plating process.

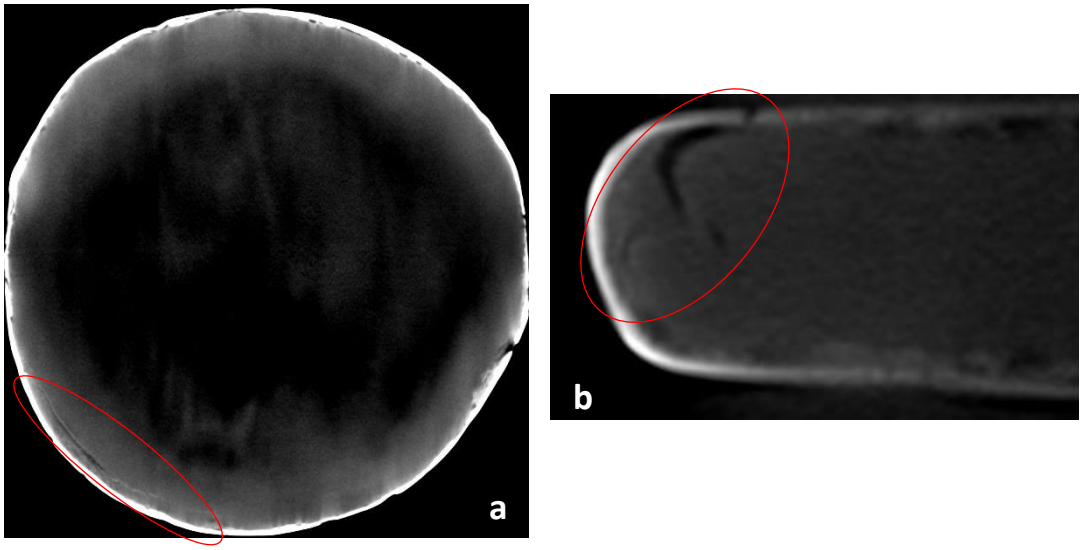

Figure 4.1.20: Transverse (a) and longitudinal (b) greyscale slices showing the internal lesion_M106 coin

The very thin silver layer and the similar values of the atomic numbers (Z) of the chemical elements most presents in flan and in coating layer of M114 and M115 coins, do not allow us an in-depth X-ray microtomography study.

From the slices examination in figures 4.1.21 and 4.1.22 it can be seen that there is no clear distinction between the silver layer and the Sn-Sb alloy core.

However, a significant detail obtained from the X-ray microtomography investigations is the presence in both core coins of cracks and voids, even of medium-large size (figure 4.1.21c and 4.1.22c), probably formed during the cooling of the Sn-Sb alloy.

The M114 and M115 coins surface are investigated under a scanning optical microscope (see paragraph 4.1.5).

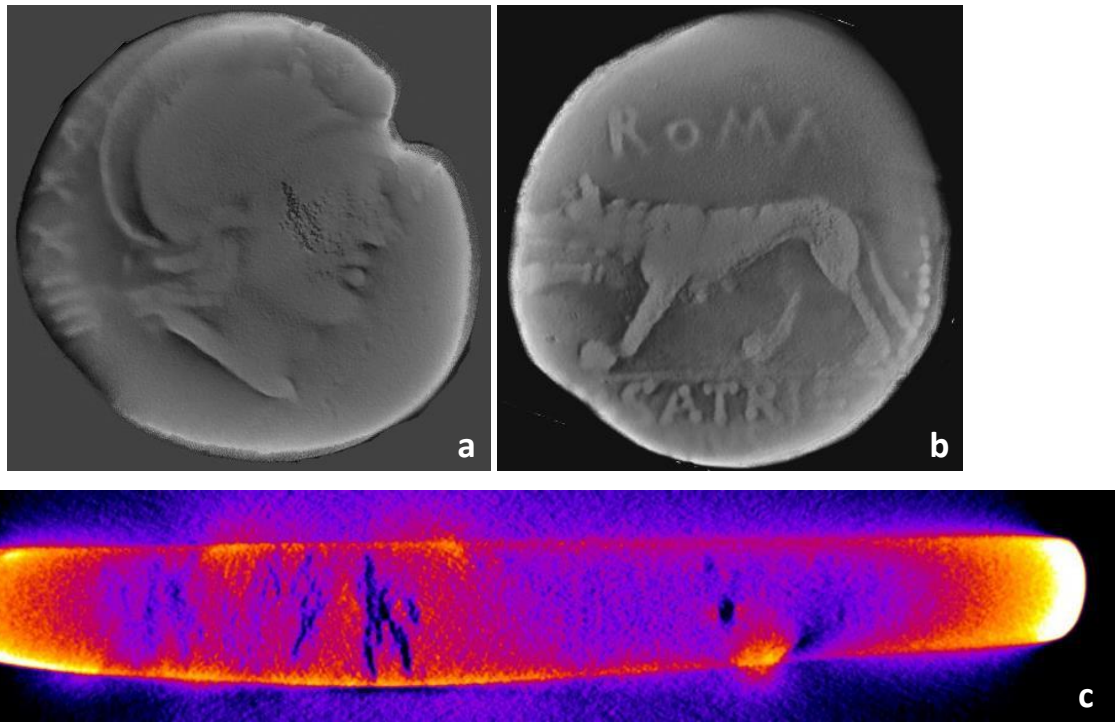

Figure 4.1.21: Transverse greyscale slice of the of the obverse(a) and reverse (b) surface; longitudinal false colours slice of the inside_M114 coin

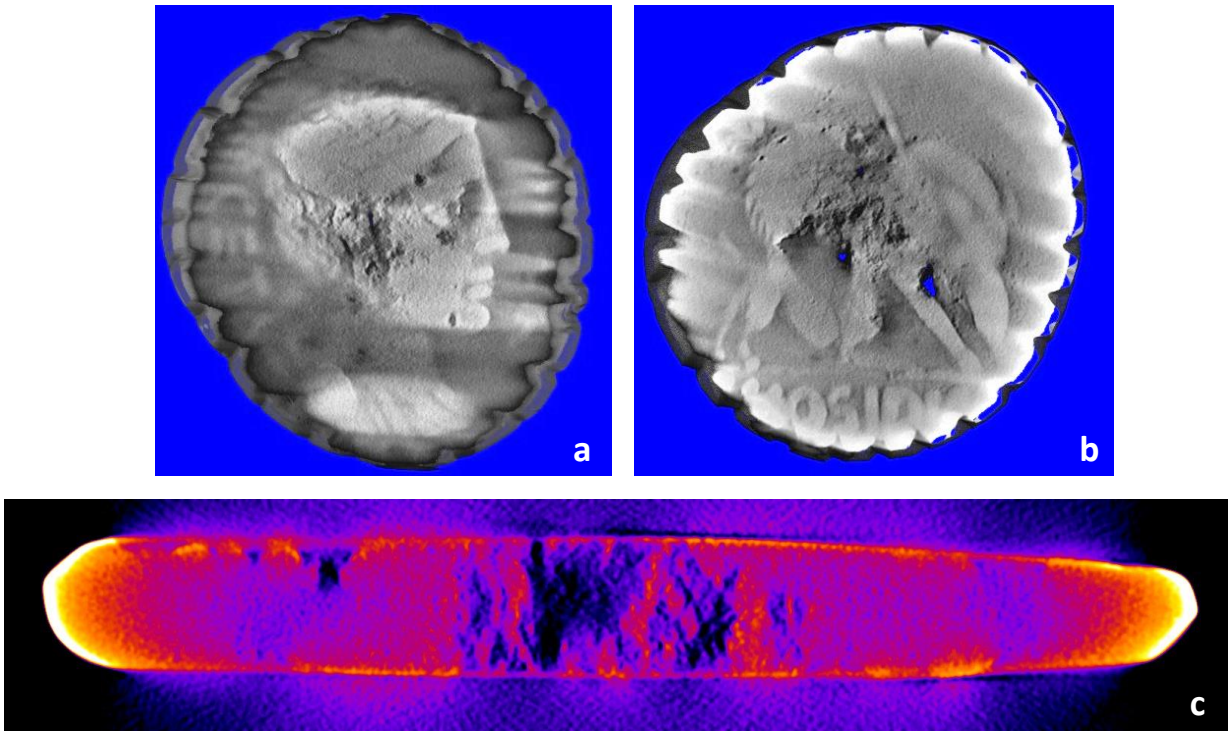

Figure 4.1.21: Transverse greyscale slice of the of the obverse(a) and reverse (b) surface; longitudinal false colours slice of the inside_ M115 coin.

4.1.5. Scanning electron microscope (SEM)

The morphological study of the M114 and M115 coins surface and the measurements of the its silver coating thickness were performed by scanning electron microscope (SEM).

Figure 4.1.22 and 4.1.23 show a SEM image of the M114 surface coin. In the first figure the red arrows in the picture miniature show the measuring point, while in the SEM image, the planchet surface and the silver layer, which is about 20 µm is clearly visible (see SEM image in figure 4.1.23)

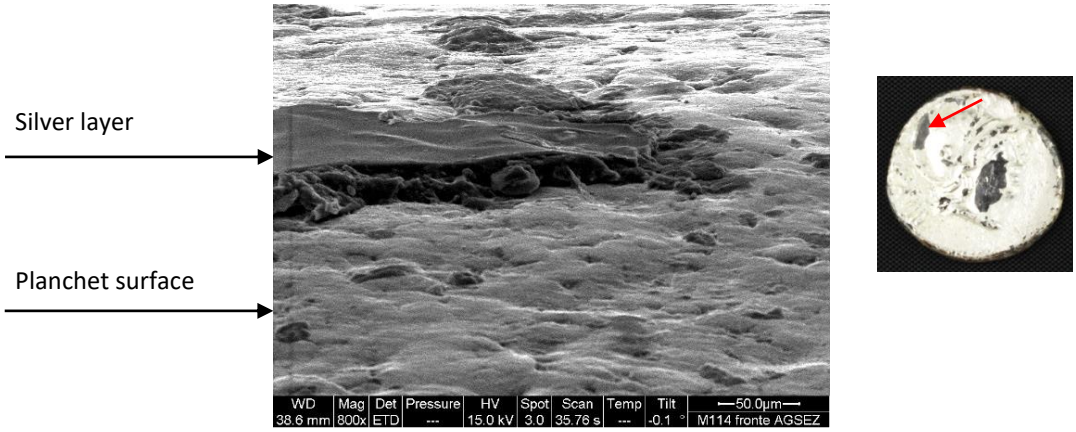

Figure 4.1.22: SEM image acquired in the M114 coin region indicated by the red arrow. The silver layer and the planchet surface are visible.

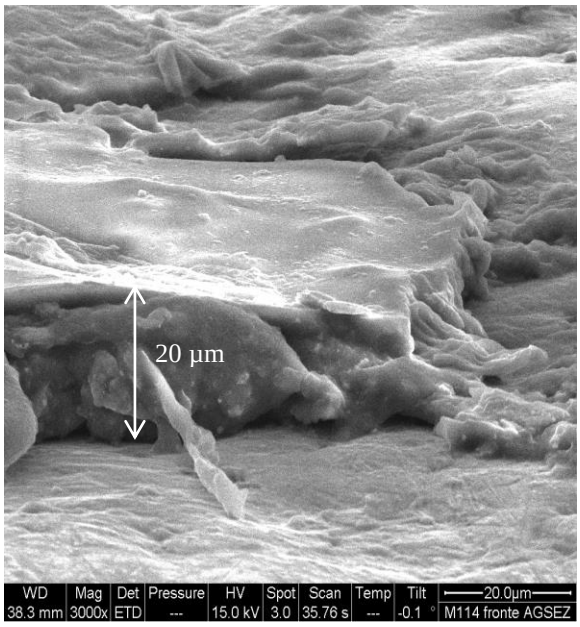

Figure 4.1.23: Higher magnification of the SEM image shown in figure 4.1.22. The silver layer thickness is 20 µm

Figures 4.1.24, 4.1.25 and 4.1.26 show a SEM image of the M114 surface coin. In the first figure the red arrows in the picture show the measuring point, while in the SEM image is clearly visible the planchet surface and the silver layer, which is about 25 µm (see SEM image in figure 4.1.25). In figure 4.1.26 the red arrows in the picture show the measuring point, while in the SEM image the planchet surface and the silver layer, which is about 25 µm, is clearly visible.

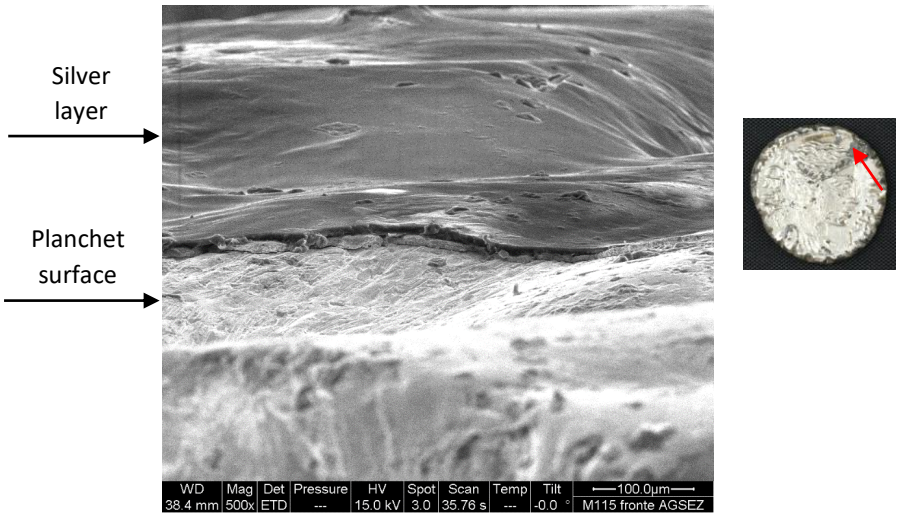

Figure 4.1.24: SEM image acquired in the M115 coin region indicated by the red arrow. The silver layer and the planchet surface are visible.

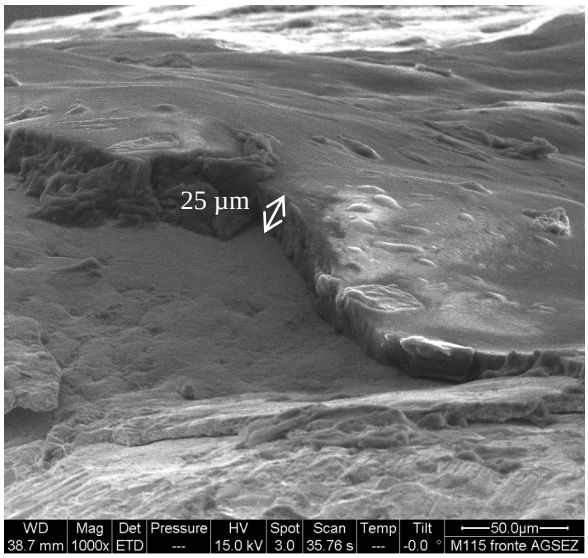

Figure 4.1.25: Higher magnification of the SEM image shown in figure 4.1.24. The silver layer thickness is 25 µm

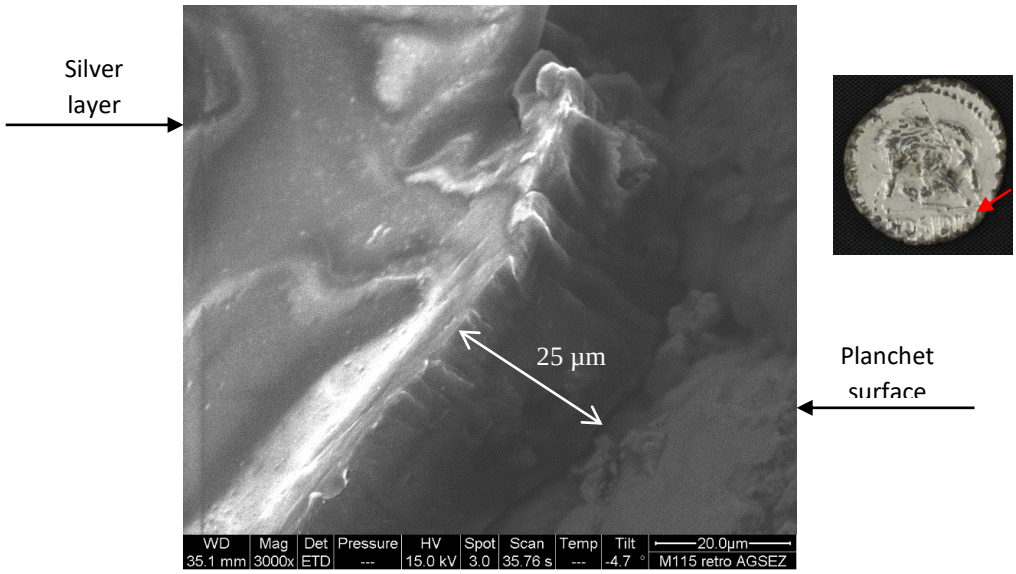

Figure 4.1.26: SEM image acquired in the M115 coin region indicated by the red arrow. The silver layer and the planchet surface are visible. The silver layer thickness is 25 µm

4.1.6. Conclusion

M114, M115 and M116 silver-plated coins preserved in the Brettii and Enotri Museum in Cosenza have been studied by complementary physical methodologies means, as an optical microscope, X-ray microtomography, XRF portable spectroscopy and scanning electron microscopy (SEM). These completely non-invasive and non-destructive methodologies have allowed to characterize the constituent materials, and to advance hypotheses on their construction methods.

The physical investigations have found that M106 coin is made from a copper core covered with a layer of silver. The presence of about 13% silver in the planchet surface is probably due to the interface between the two materials created as part of the plating process. The coin features an uneven thickness silver layer: at both sides the silver layer thickness varies between 100 µm and 170 µm, therefore in correspondence to the edge the silver layer thickness is almost double (200-300 µm). There are some low-absorption areas between the coating layer and the flan surface due to corrosion phenomena. The X-ray microtomographic reconstructions also show

the presence of a crack in both the planchet and the silver layer, maybe it was made as a result of the high stress underwent during the coining process that occurred after plating process.

So, we can assume that first the copper flan coin was made, which has been covered by two thin silver sheets, one for each face. In some area to the edge the silver sheets was overlapped, then the coin was heated up to the silver melting temperature, in order to create an interphase between the two metals. Later the coin was minted. Our hypothesis are supported by data present in the literature. [65], [66], [76]

The M114 and M115 coins were both made with Sn-Sb alloy core covered with a homogeneous and very thin layer of silver, about 20 µm for the M114 coin and 25 µm for the M115 coin. In both cases, the plating phase could have occurred by planchet immersion in a bath of molten silver. This procedure allows covering in a homogeneous manner with a very thin layer (few tens of µm) even irregular surfaces such as those of coins. [79] The thickness of thin silver layer and the similar melting point between silver and Sn-Sb alloy excludes a silver leaf use, while the absence of mercury in chemical investigations excludes the amalgam technique.

4.2. Case study 2

Roman coins from the “Brettii and Enotri” museum: a non-destructive archaeometric study

4.2.1. Introduction

In this case study the results of the chemical-physical investigations performed on two Roman coins conserved in the Brettii and Enotri museum in Cosenza will be discussed. The objects under investigation are present in the Museum Coins Collection catalogue [75] as M73 (figure 4.2.1) and M75 (figure 4.2.2) and they are part of a group of 30 coins. These coins were found found in the Cave of the Nymphs, an ancient source of sulphurous water near Cerchiara di Calabria (Cs). All coins except for two are fully oxidized and not readable.

Figure 4.2.1: Obverse and reverse of the M73 coin

Figure 4.2.2: Obverse and reverse of the M75 coin

The archaeological study of the reference context, and of the coin in better conservative conditions (M94 in catalogue [75]), which is show in figure 4.2.3, allowed us to hypothesize that these finds are dating to Julio-Claudian dynasty (27 BC – 68 AD) or Flavian dynasty (69 AD – 96 AD). These coins were used as reference sample.

Figure 4.2.3: Obverse (a) and reverse (b) of the M94 coin in better conservative conditions

The aim of this work is chemical and morphological studies by XRF portable spectrometer and X-ray microtomography, in order to understand the oxidation processes, to know constituent material and to find hidden signs or inscriptions.

4.2.2. X-Ray fluorescence spectroscopy

The XRF chemical investigation was performed to detect the coins chemical nature and to understand the oxidation processes. For each coin, two measurement points were chosen, which were averaged between them.

The parameters used to perform the XRF measurements are shown in table 4.2.1.

Energy	50 keV
Voltage	50 kV
Current	700 µA
Collimator	0.65 mm
Exposition time	1200 s

Table 4.2.1: XRF measurements parameters

The M73 and M75 XRF spectra are very similar. Figure 4.2.4 shows only spectrum about M75 coin and the relative atomic concentrations of the chemical elements are shown in table 4.2.2.

The surface coin measurements revealed a copper and sulphur presence, 33.15% and 66.44 respectively. Other secondary elements are present, as titanium (0.06%), iron (0.10%), zinc (0.10%), arsenic (0.02 %), tin (0.03%) and led (0.12%).

The sulphur presence due to oxidation processes caused by coin permanence near source of sulphurous water.

So, coins are made of copper metal.

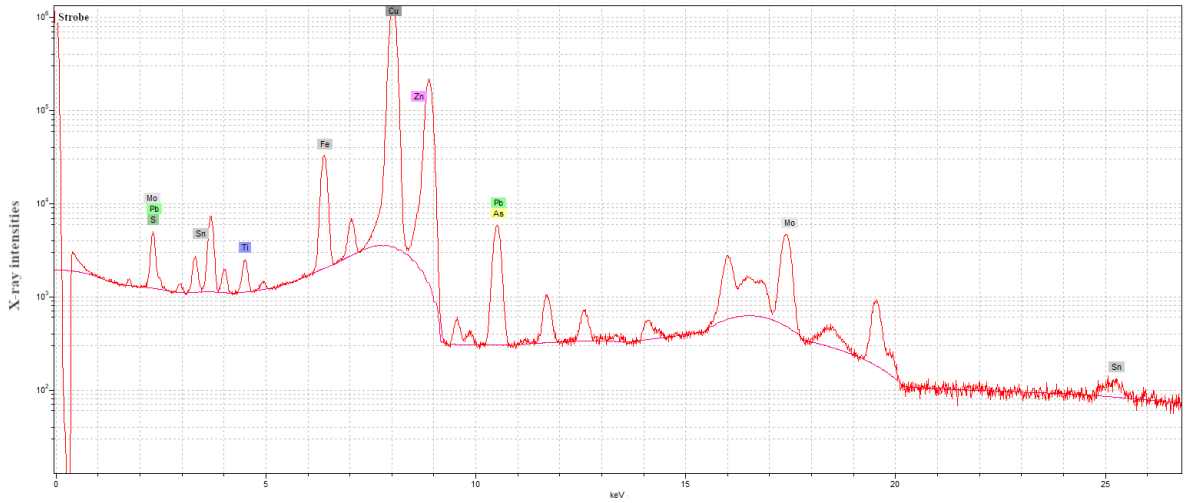

Figure 4.2.4: XRF spectra in logarithmic scale of the M75 coin's surface

N.	Element	Silver layer Conc. (%)
1	S Kα	66.44 ± 1.35
2	Ti Kα	0.06 ± 0.05
3	Fe Kα	0.10 ± 0.04
4	Cu Kα	33.15 ± 1.41
5	Zn Kα	0.10 ± 0.02
6	As Kα	0.02 ± 0.01
7	Sn Kα	0.03 ± 0.01
8	Pb Lα	0.12 ± 0.02

Table 4.2.2: atomic concentrations of the elements present on the M75 coin's surface

4.2.3. X-ray microtomography

The X-ray microtomography surveys of the M73 and M75 samples showed a series of sign similar to those found in M94 coin's surface.

The measurements parameters are shown in table 4.2.3. The tomographic reconstructions were correcting by following correction parameters: ring artefact reduction and beam hardening compensation 20%.

Voltage	150 KV
Current	66 µA
Exposure time for each projection	0.5 s
Focal spot	middle
Magnification	3
Pixel size	16.67 µm
Number of projections	1805
Step	0.2°

Table 4.2.3: X-ray microtomography measurements parameters

The follow X-ray microtomogaphy slice in figures 4.2.5-4.2.6 show more oxidation layer covering the coins bulk, in M73 and M75 coins respectively. In both cases, the oxidation layer thickness is 3.5 mm, while the coin edge thickness is 1.5 mm in accord to M94 coin edge thickness.

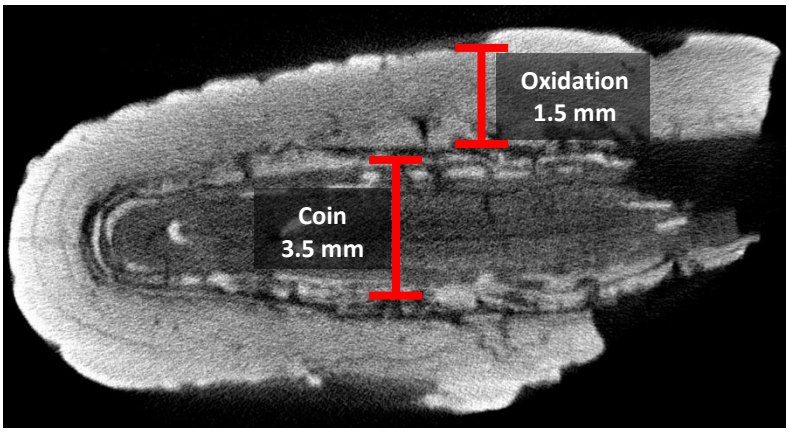

Figure 4.2.5: longitudinal grayscale slice of the M73 coin

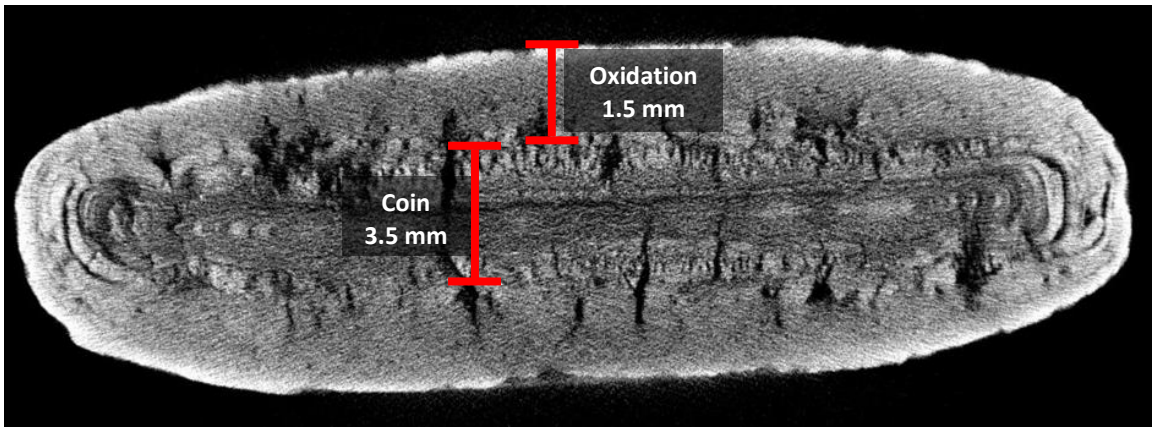

Figure 4.2.6: longitudinal grayscale slice of the M75 coin

Figures 4.2.7 and 4.2.8 show a transverse slice of M73 and M75 coins respectively, of which the diameter is measured. It is in accord to M94 coin diameter that is approximately 3 cm.

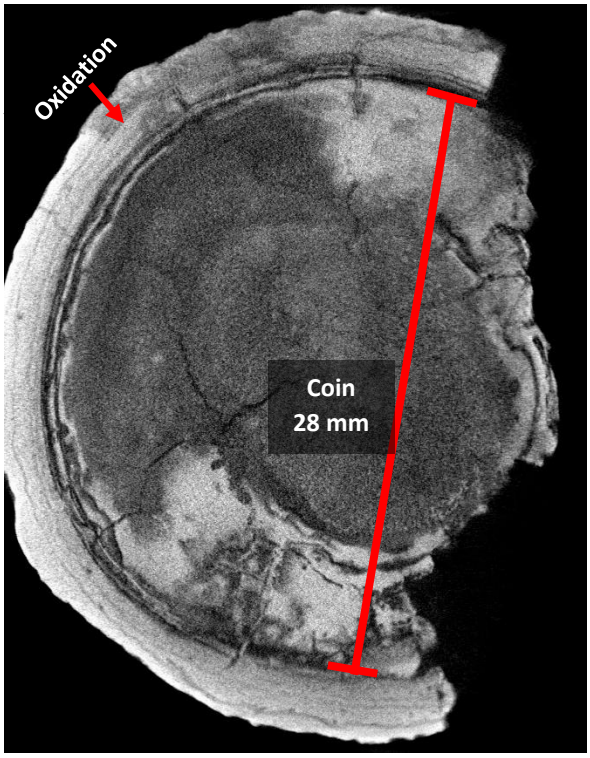

Figure 4.2.7: transverse grayscale slice of the M73 coin

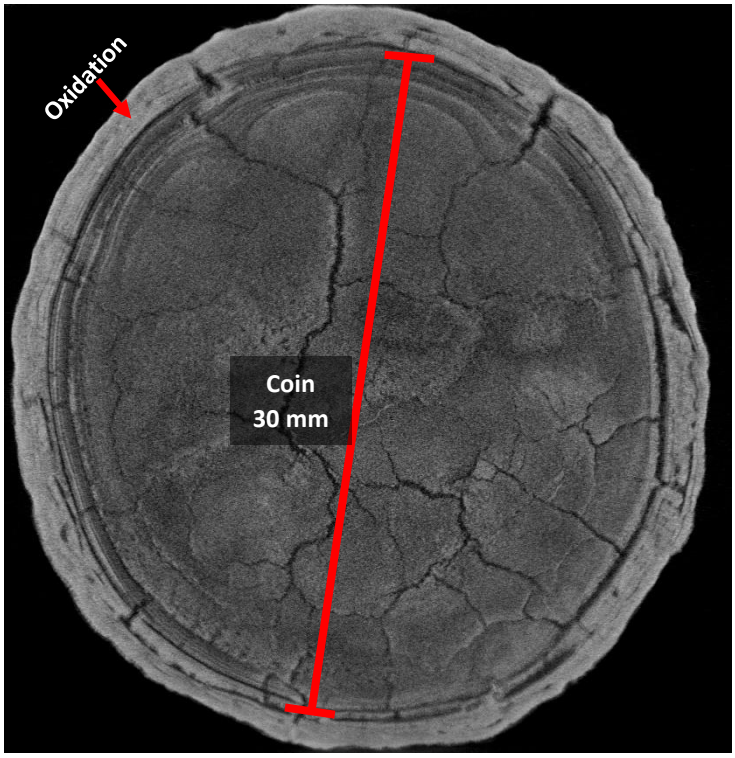

Figure 4.2.8: transverse grayscale slice of the M75 coin

Thanks to morphological analysis carried out on copper coins, we could find a similar sign to reference sample (i.e. M94 coin).

The M73 coin's grayscale slice in figure 4.2.9a shown a sign similar to head profile in M94 coin, shown in figure 4.2.9b.

Figure 4.2.9: M73 coin's grayscale slice (a) show a profile similar to head profile in M94 coin (b)

Another sign we found in the M73 coin, is shown in figure 4.2.10. Figure 4.2.11b shows a greyscale histogram acquired along the yellow line in figure 4.2.11a which has a different trend than the histogram acquired in other areas of the coin.

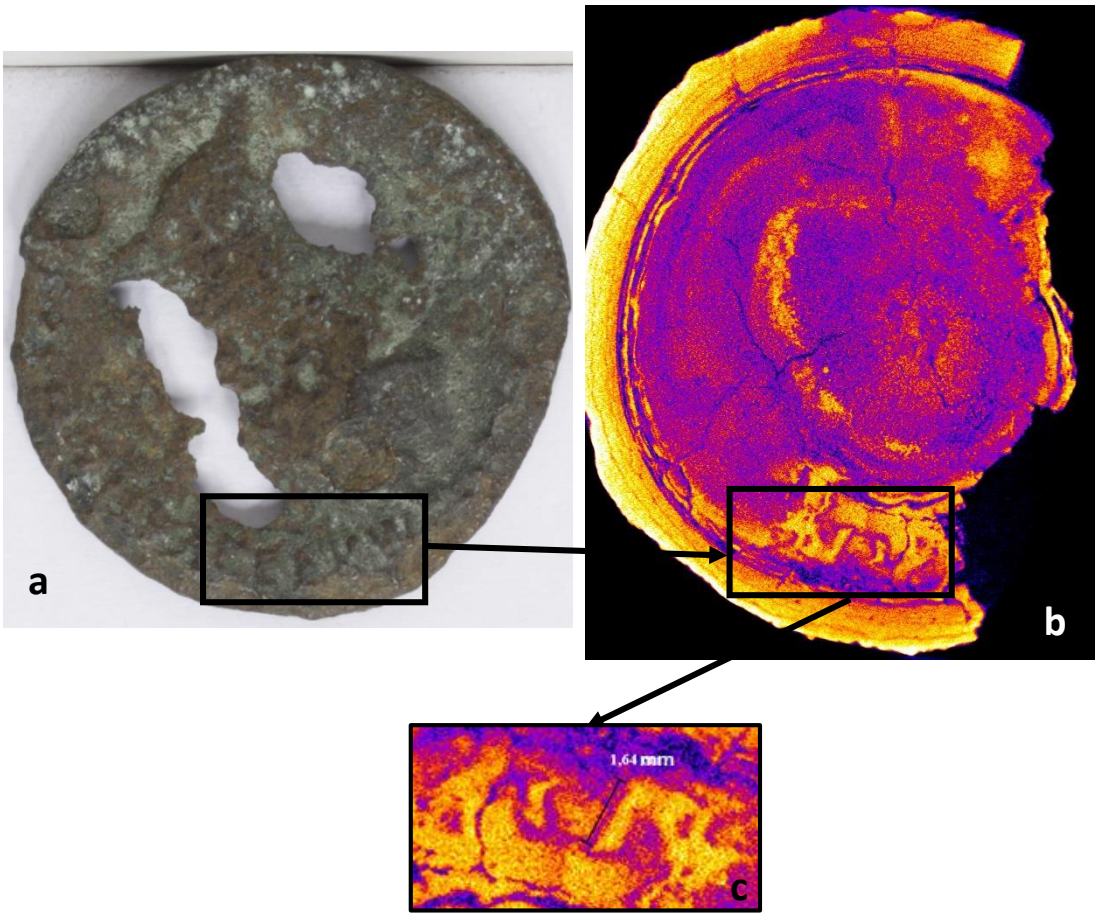

Figure 4.2.10: Coin M94 picture (a); false colour slice of the M73 coin in which are visible relevant signs (b); magnification of square area in figure 4.2.10b (c)

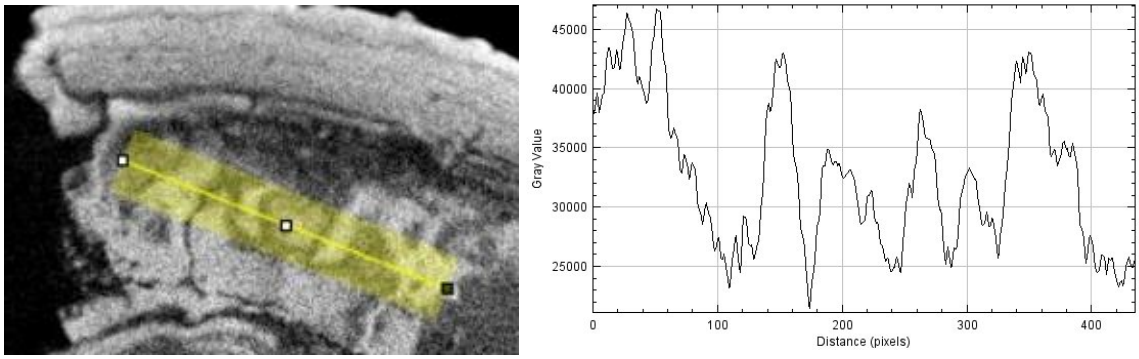

Figure 4.2.11: grey levels histogram acquired along the profile indicated by the yellow line

The M75 coin's false colour slice in figure 4.2.12 shows a sign similar to the inscription on the M94 coin.

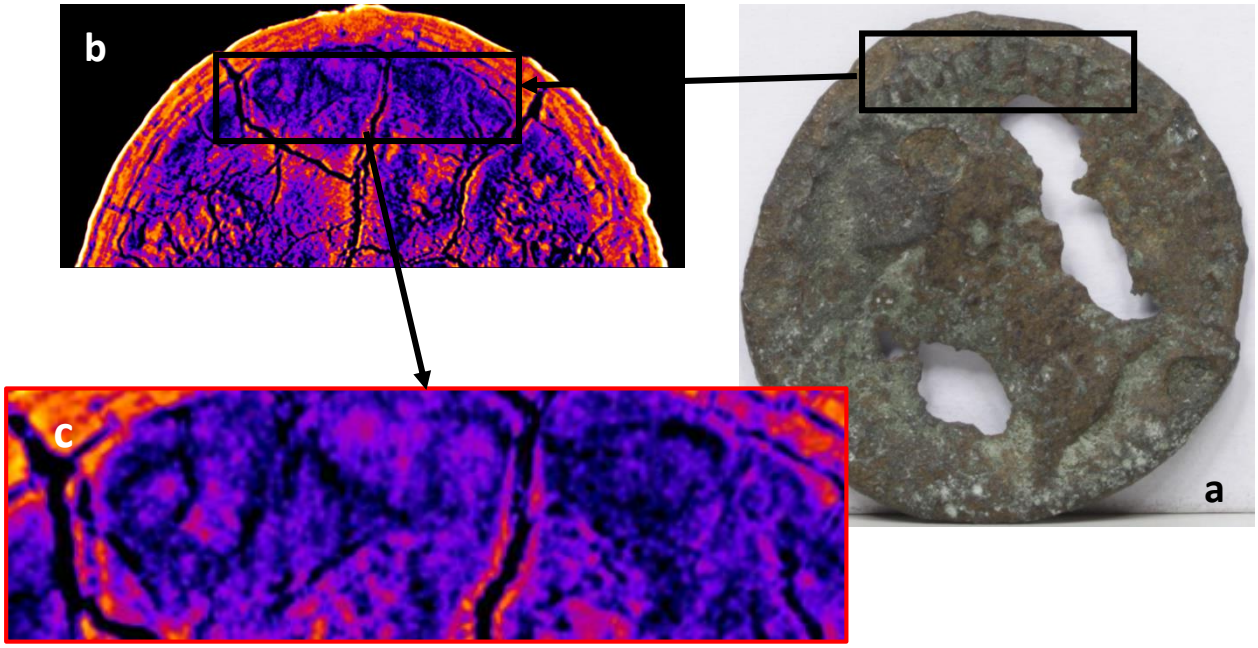

Figure 4.2.12: Coin M94 picture (a); false colour slice of the M75 coin in which relevant signs are visible (b); magnification of square area in figure 4.2.10b (c)

4.2.4. Conclusion

M73 and M75 coins preserved in the Brettii and Enotri Museum in Cosenza have been studied by complementary physical methodologies means, as X-ray microtomography and XRF portable spectroscopy. These completely non-invasive and non-destructive methods methodologies have allowed to understand the oxidation processes, to know constituent material and to find hidden signs or inscriptions.

Both coins are made of copper and they have followed an oxidation process due to the sulfur spring near the discovery site. Oxidation layers made the coins inscriptions unreadable. Thanks to morphological studies by X-ray microtomography we could find signs and inscriptions compatible with the inscriptions present on the reference coin. Therefore, we can say that the coins analyzed are belong to the same typology.

Then all the coins of the collection will be analyzed in future research.

4.3. Case study 3

Archaeometric investigation of a *unicum* object and a thin bronze plaque found in the arcaic sanctuary of Timpone della Motta in Francavilla Marittima (Cs)

4.3.1. Introduction

The archaeological site of Timpone della Motta is considered a key location for the understanding of the gradual cultural transformation that took place in Southern Italy during the period from around 800 to 500 BC. The earliest traces of human activities date back to the late Bronze Age, while the main period of activity at the site dates from the 8th to the 6th century BC. [80]

The archaeological finds under investigation have been excavated in the sanctuary area in a context datable to the Archaic period (VI century b.C.).

The aim of the current study is to determine the materials and technological features of *unicum* object and to read possible inscriptions and decorations under the superficial encrustations of bronze plaque.

The surveys were conducted by means of non-destructive techniques: X-ray microtomography, X-ray radiography and portable XRF spectroscopy.

Figure 4.3.1 and 4.3.2 show the *unicum* object and bronze plaque respectively.

The first is constituted by an oval stone element in which a metal ring is inserted, the second find is a fragmentary bronze plaque constituted by four thin fragments. In both case, their function is unknown. By result of archaeological investigation, *unicum* object has been likely used as a reference to weigh the food in ritual practices. A comparison can be made with the so called *Roman-Oscan pound.* [81]

Figure 4.3.1: *Unicum* object

Figure 4.3.2: Thin bronze plaque

4.3.2. Optical investigation: *unicum* object

In order to characterize peculiar elements and to find working traces, a visual investigations has been carried out on the *unicum* artifact. The latter is made by calcareous material and its shape is perfectly oval and there are some marks on it, maybe made smooth by human action. Another important characteristic is the trace of combustion on a side of the artifact (shown in figure 4.3.3), probably caused by a heat source used during the processing stages. However, the bronze ring is inserted in the stone's hole, filled by unknown material (figure 4.3.4).

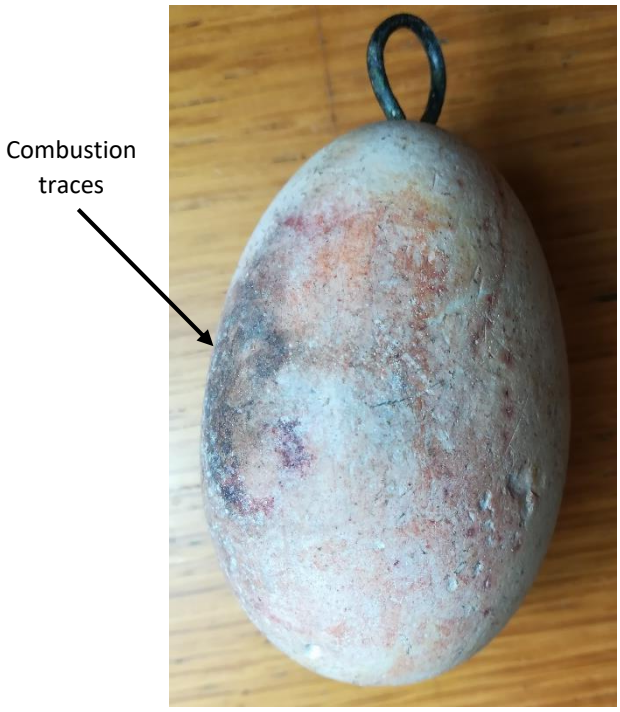

Figure 4.3.3: combustion traces on a side of the *unicum* object

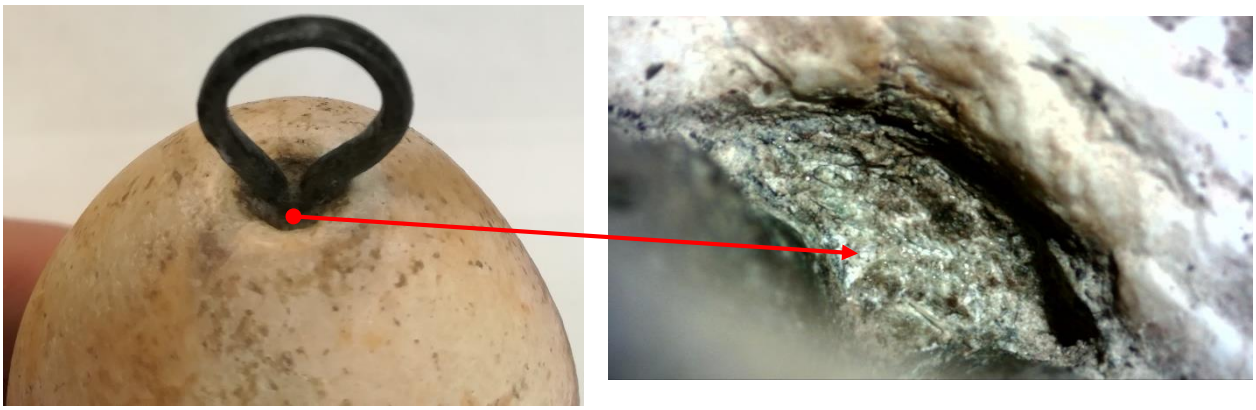

Figure 4.3.4: Bronze ring in a stone's hole filled by unknown material

4.3.3. X-ray microtomography: *unicum* object

The X-ray microtomography surveys of the *unicum* object showed a series of peculiarity non-appreciable by visual investigations. This physical methodology has allowed to advance hypotheses on construction methods.

The measurement parameters are shown in table 4.3.1.

Voltage	150 KV
Current	100 µA
Exposure time for each projection	1 s
Al filter	25 µm
Focal spot	middle
Magnification	1.5
Pixel size	33.33 µm
Number of projections	1805
Step	0.2°

Table 4.3.1: X-ray microtomography measurements parameters

Frontal and lateral radiographic images in figure 4.3.5 shown that hole on the stone top have a conical shape and it is filled by an opaque to X-ray material.

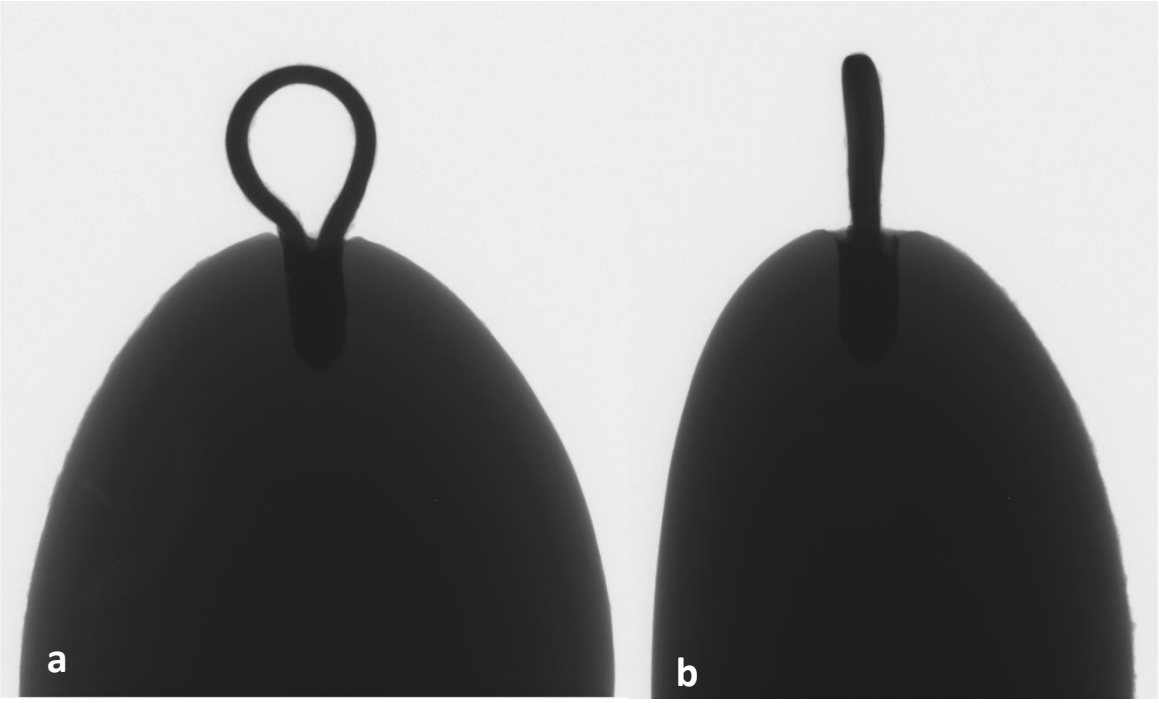

Figure 4.3.5: Frontal (a) and lateral (b) unicum radiographic images

By false colour slice in figure 4.3.6 it is possible to clearly see each element of the artifact. Particularly, the ends of the bronze ring are put in a hole filling material which is characterized by a different rate of X-ray absorption.

The stone and the other elements contribution have been separated (as shown in figure 4.3.7a) achieved grey-level segmentation of X-ray microtomographic reconstruction. Therefore, in the virtual transversal section shown in figure 4.3.7b the two ends of the ring are pretty distinguishable as well as the filling material.

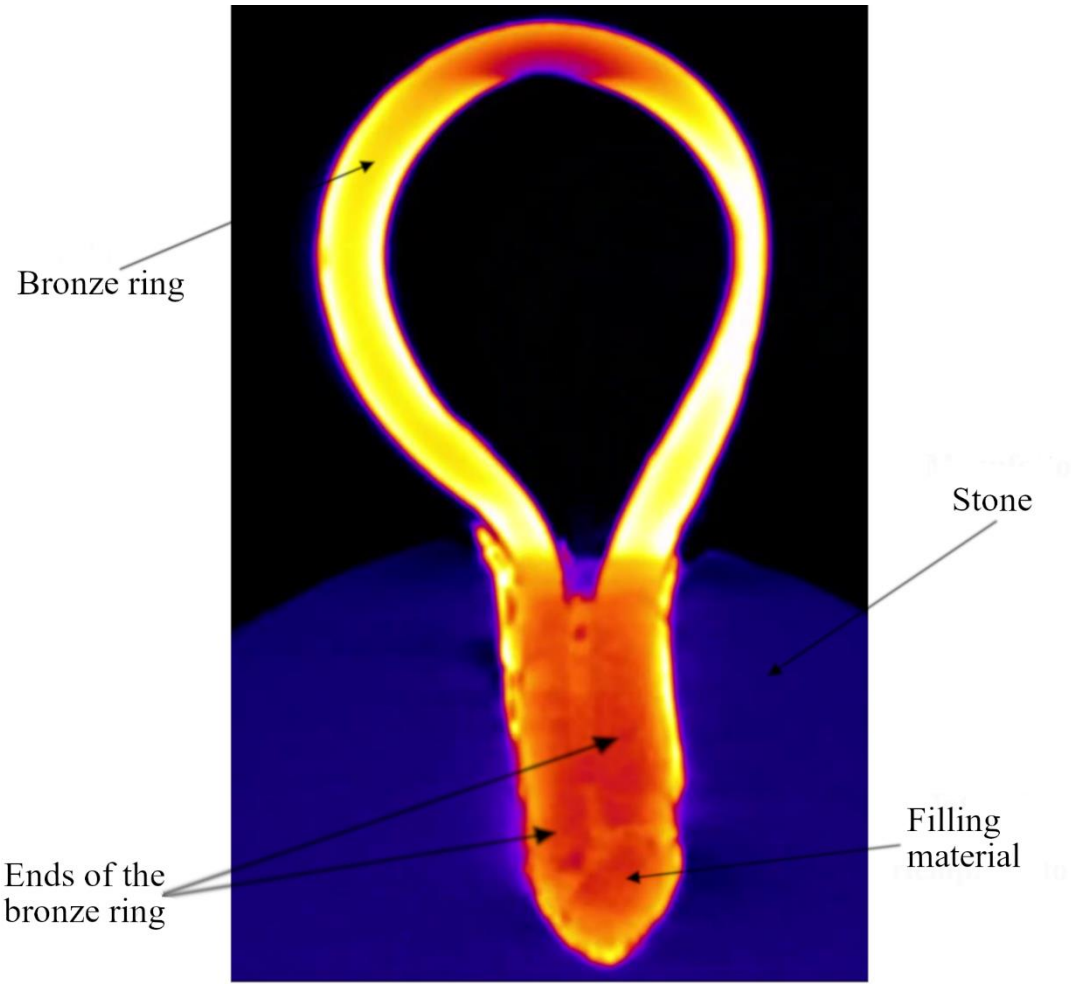

Figure 4.3.6: false colour slice in which is possible to clearly see each element of the artefact: bronze ring, stone, ends of bronze ring and filling material .

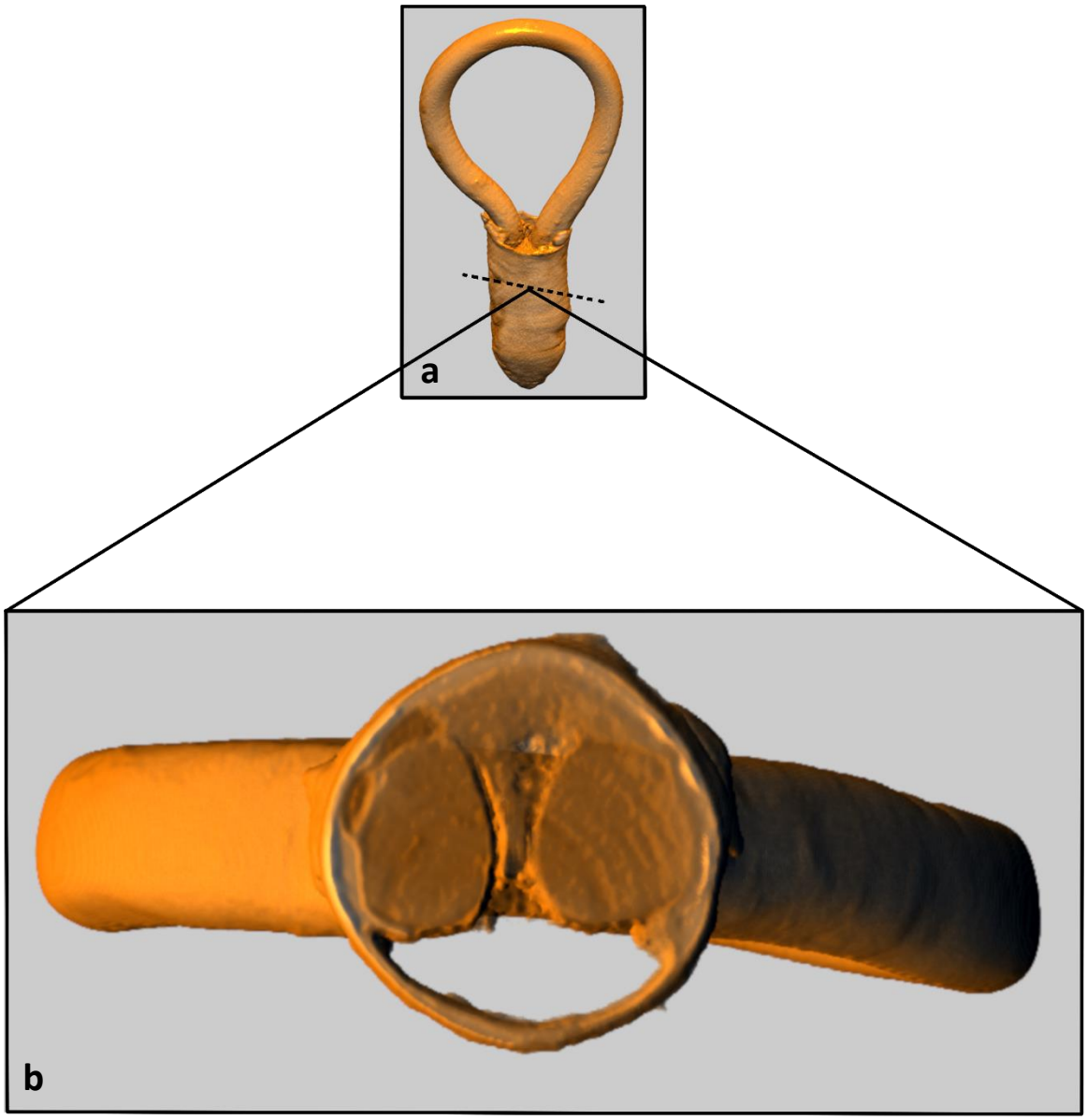

Figure 4.3.7: virtual transversal section (b) of 3D rendering after grey-level segmentation (a). The two ends of the ring are pretty distinguishable as well as the filling material

A mark is visible in the internal part of the ring, probably made by a rope rubbing or by another material (figure 4.3.8a) during its use as weight. A series of voids in the filling material probably due to air bubbles are shown in figure 4.3.8b. At last, filling material lifting along the hole edges is shown in figure 4.3.8c. Such results let us to suppose that the filling material was put in the hole at the liquid state.

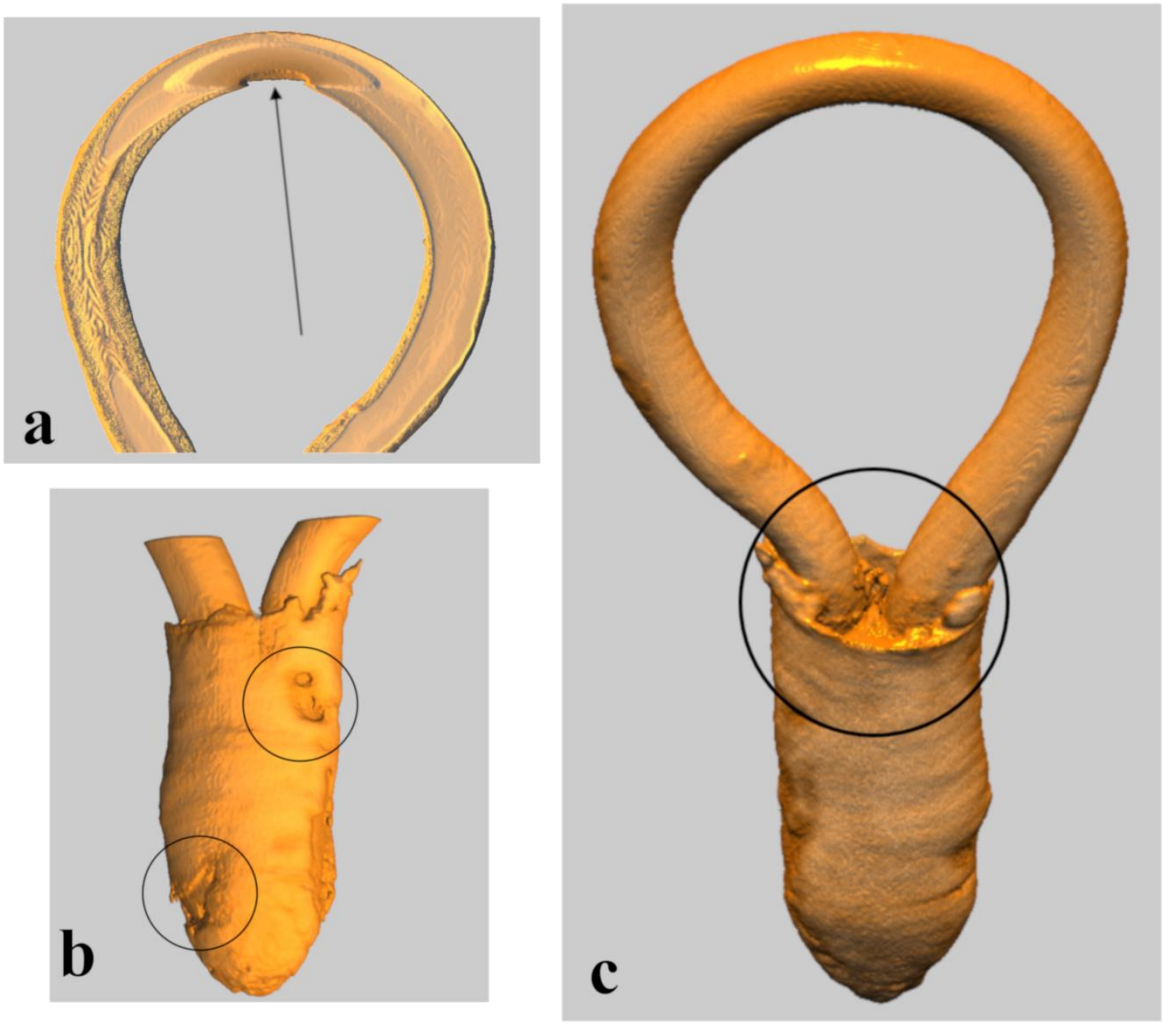

Figure 4.3.8: mark visible in the internal part of the ring probably made by a rope rubbing or by another material during its use as weight (a); voids in the filling material probably due to air bubbles (b); filling material lifting along the hole edges (c)

Longitudinal and transversal slice section in figure 4.3.9 show the elements dimensions. The conical hole length and diameter are 14 mm and 6 mm respectively. The conical shape let us suppose that the hole was made by a manual drill. The bronze ring has a section diameter of 2.5 mm and its ends are 8 mm deep. The maximum height of the ring is 25 mm while the maximum width is 15 mm. The rubbing mark is 2.5mm.

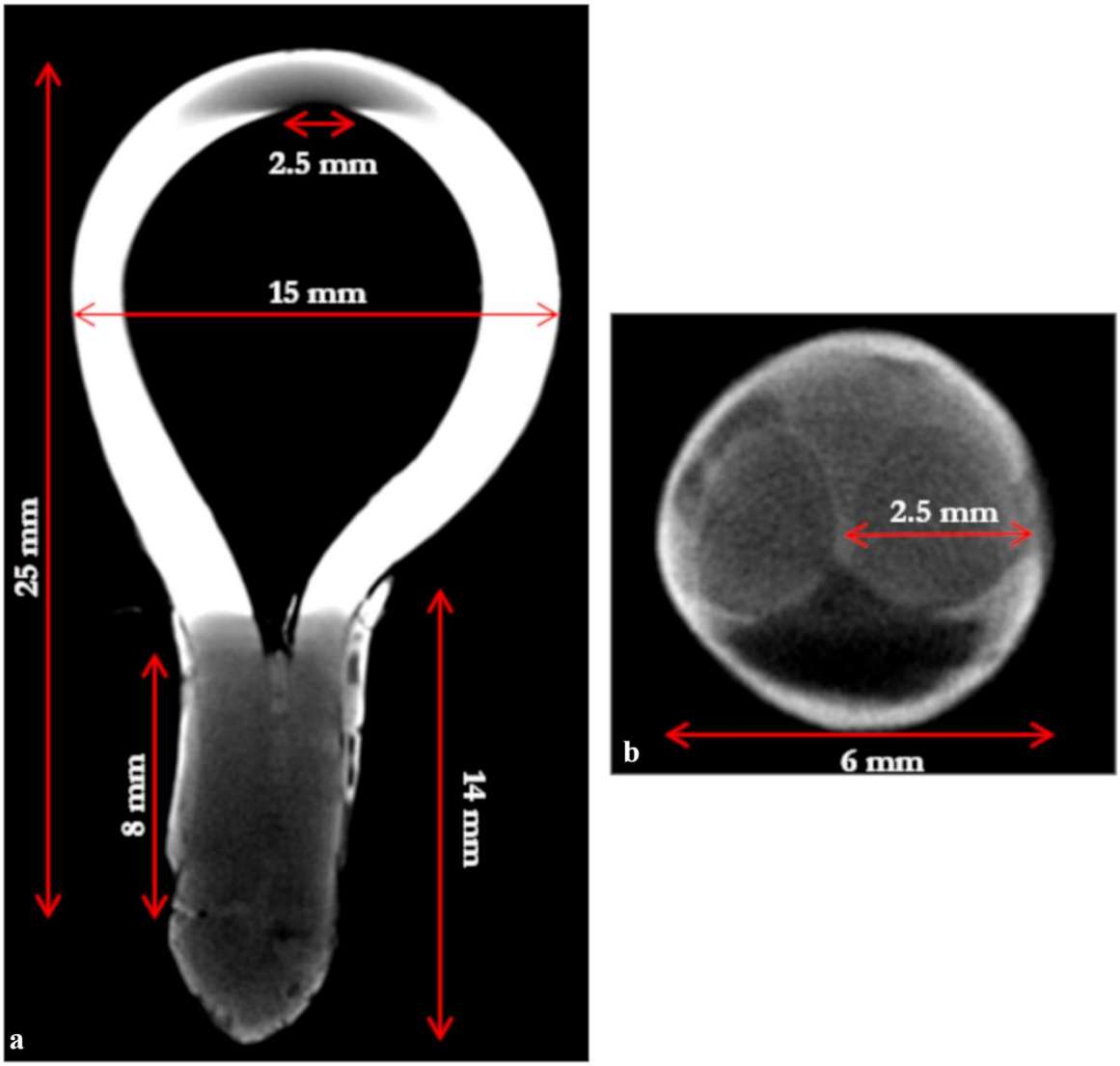

Figure 4.3.9: Transversal (a) and longitudinal (b) slice section in which are shown the find elements dimensions.

4.3.4. X-ray fluorescence spectroscopy: *unicum* object

The XRF chemical investigation was performed to detect the ring and the hole filling chemical nature. Three measurement points were chosen (shown in figure 4.3.10).

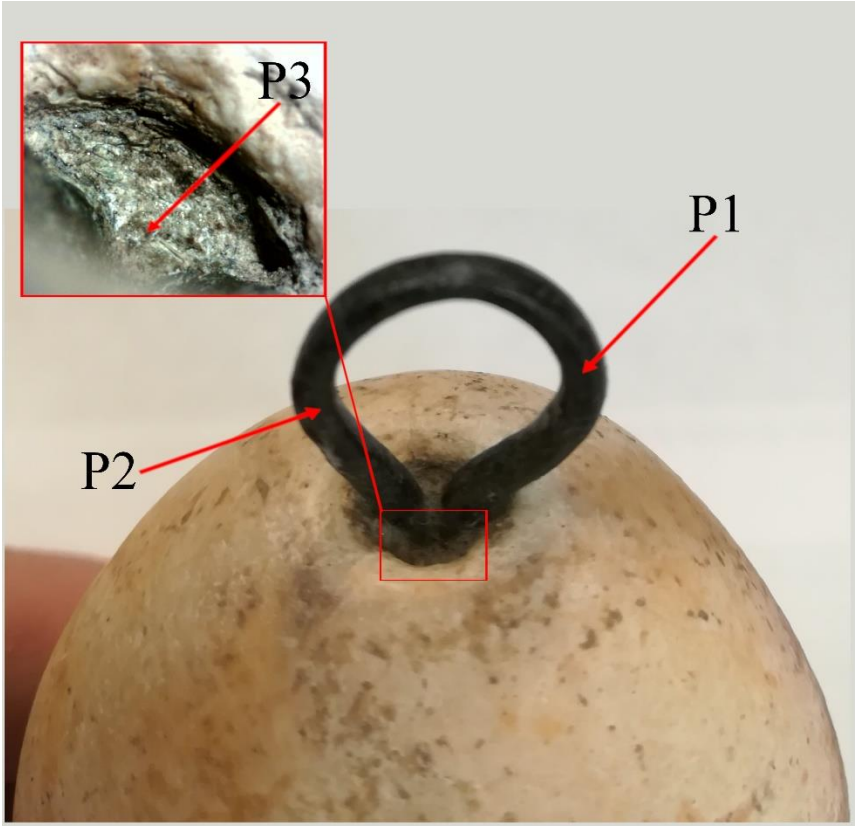

Figure 4.3.10: XRF measurement points

The parameters used to perform the XRF measurements are shown in table 4.3.2.

Energy	25 keV
Voltage	50 kV
Current	700 µA
Collimator	0.65 mm
Exposition time	750 s

Table 4.3.2: XRF measurements parameters

The XRF spectrum about bronze ring and hole filling are shown in figure 4.3.11 and 4.3.12 respectively. However, the relative atomic concentrations of the chemical elements are shown in table 4.3.3 and 4.3.4.

By spectra study we can confirm the bronze nature of the ring. It's approximately made by 69% copper and 28% tin with presence of secondary elements as lead (1.84%), titanium (0.10%), iron (0.83%), cobalt (0.30%), nickel (0.23%), zinc (0.20%), strontium (100ppm), silver (700 ppm) and rubidium (<100 ppm). The high value of tin is due probably to superficial decuprification phenomenon. [82]–[84]

The hole filling is a Sn (34%) - Pb (64%) alloy. This alloy owns good characteristics of surface tension reduction, wetting and corrosion resistance. Another relevant property is the melting temperature which drops in comparison to melting temperature of the single metals, as shown in in Pb-Sn phase diagram (figure 4.3.13). So, a Pb-Sn alloy allowed a ring strong adhesion and for a long time at the stone.

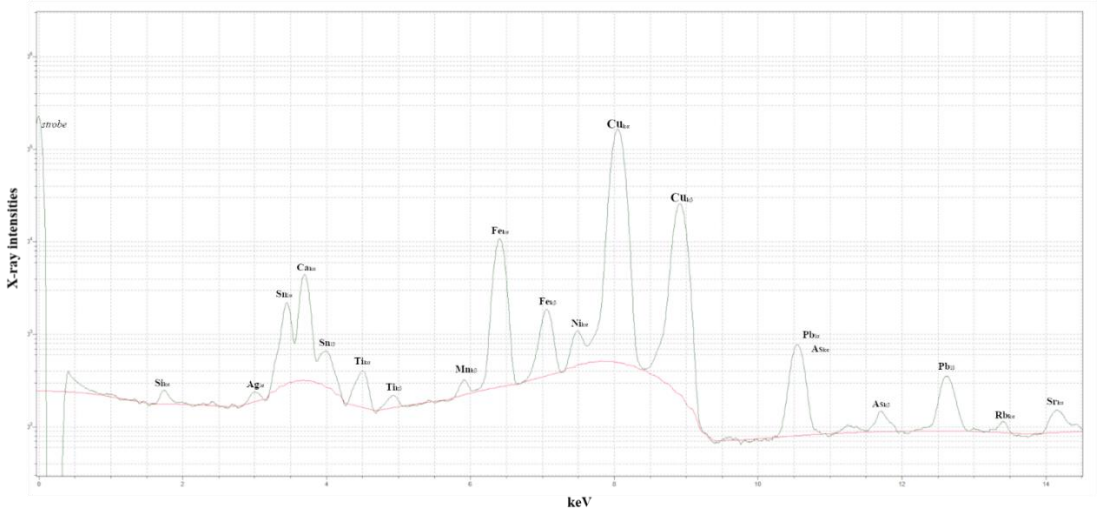

Figure 4.3.11: XRF spectra in logarithmic scale of the bronze ring

Element	Conc./%
Ti Kα	0.10 ± 0.06
Fe Kα	0.83 ± 0.28
Co Kα	0.30 ± 0.03
Ni Kα	0.23 ± 0.01
Cu Kα	68.74 ± 0.17
Rb Kα	<0.01
Zn Kα	0.20 ± 0.01
Sr Kα	0.01 ± 0.01
Ag Kα	0.07 ± 0.02
Sn Lα	27.7 ± 0.07
Pb Lα	1.84 ± 0.49

Table 4.3.3: atomic concentrations of the elements present in bronze ring

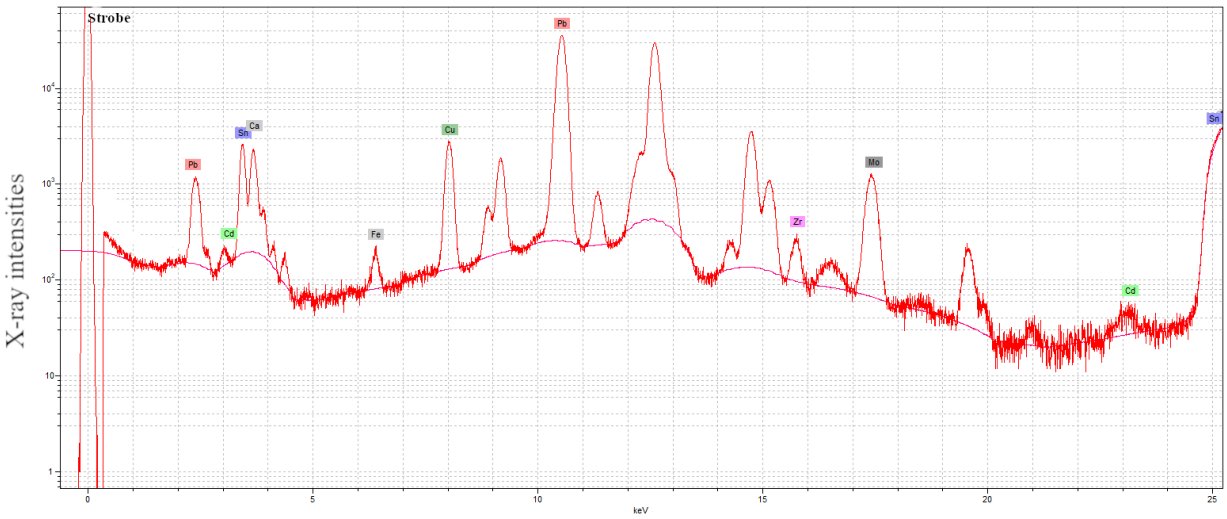

Figure 4.3.12: XRF spectra in logarithmic scale of the hole filling

Element	Conc./%
Fe Kα	0.01
Cu Kα	1.07
Cd Kα	<0.01
Zr Kα	<0.01
Sr Kα	0.01
Ag Kα	0.07
Sn Lα	33.94
Pb Lα	63.98

Table 4.3.4: atomic concentrations of the elements present in hole filling

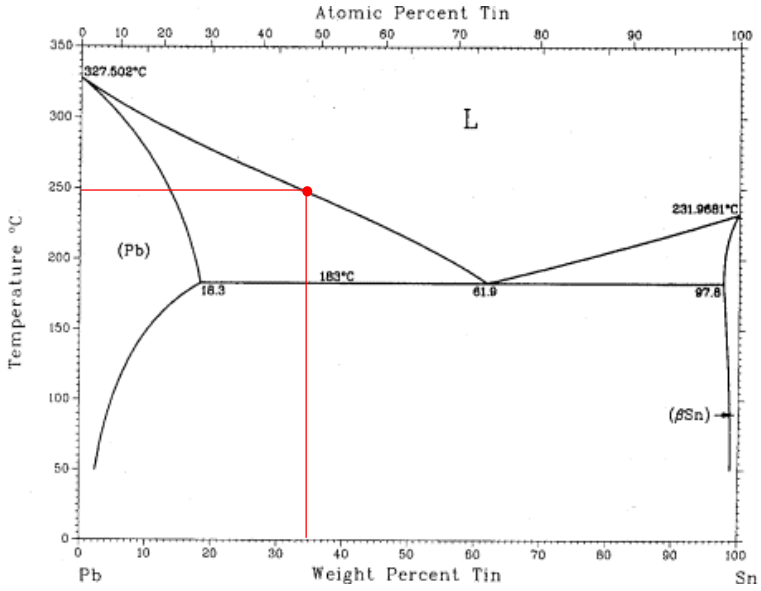

Figure 4.3.13: Pb-Sn phase diagram in which the red point is melting temperature for Sn 34% and Pb 64% alloy

4.3.5. X-ray radiography: bronze plaque

The radiographic investigations of the bronze plaque have revealed some engraving and decoration below oxide coat and surface residual. The bronze plate is very thin

and fragile, so thanks to a non-destructive archaeometric technique which X-ray microtomography was possible to analyze the decoration without ruin the artifact.
The figure 4.3.14a and 4.3.14b shown a radiographic images in grey scale and false colour respectively. The same images are analyzed using Gaussian Blur e Unsharp Mask filters (figure 4.3.15).

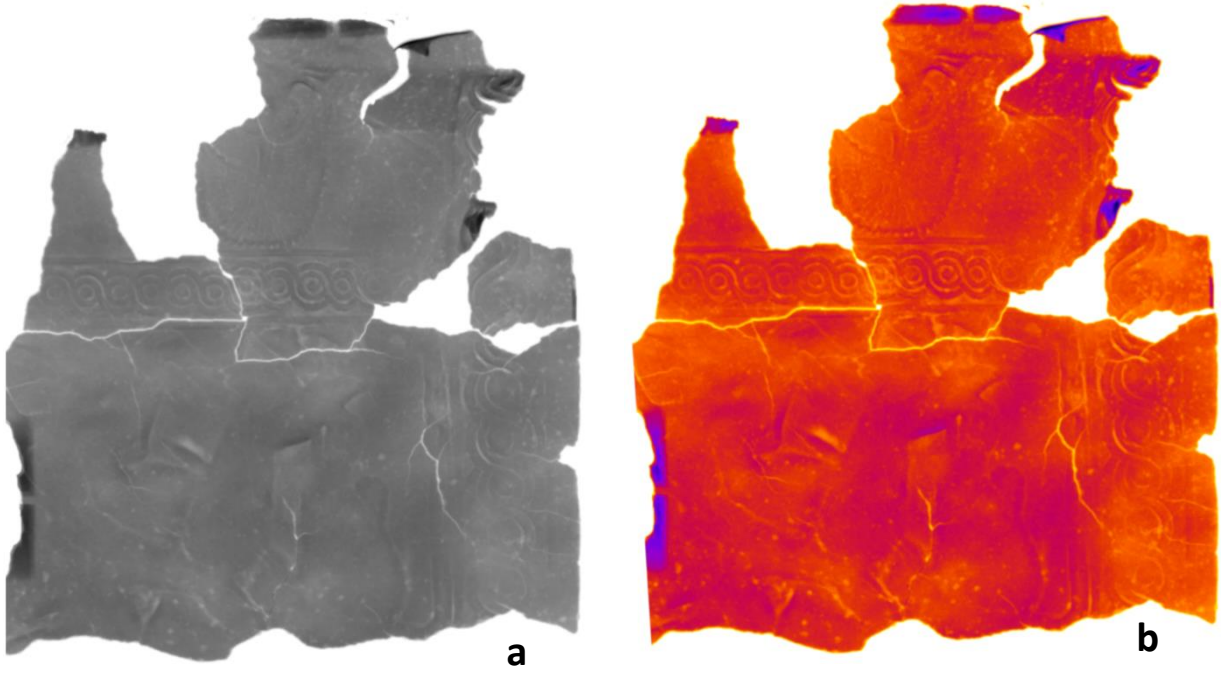

Figure 4.3.14: radiographic images of the bronze plaque in grey scale (a) and false colour (b)

Figure 4.3.14: radiographic images of the bronze plaque analyzed using Gaussian Blur e Unsharp Mask filters

4.3.6. Conclusion

The artifacts analyzed in this case study have been found out in a votive deposit of VI b.C., placed in the archaic sanctuary of Timpone della Motta (Francavilla Marittima, Cosenza).

The first element is a reference to weigh the food in ritual practices constituted by an oval stone artifact on which top was made an hole in order to put inside a bronze ring. The second one is a fragmentary bronze plate, extremely fragile, which inscriptions and decorations was hidden by superficial encrustations. The use of high resolution and high energy X-ray microtomography and radiography and the use of X-ray fluorescence spectroscopy, have given information about the materials and the building process and they made readable hidden decoration.

The first artifact is a stone which weight is 276 g. On the top of it was made a conical hole of 14 mm length and 6 mm diameter, it was made by a manual drill. The hole was filled by a molten Pb 64%-Sn 34% alloy while, which has good characteristics of surface tension reduction, wetting and corrosion resistance. Later, keeping artefact near heat source in order to maintain the alloy at liquid state, the two ends of the bronze ring have been put inside the hole. The ring is made of a Cu (68.74 %) and Sn (27.70%) alloy. The microtomographic reconstructions have shown a visible mark in the internal part of the ring, probably made by the rope rubbing or by another material used as hanging. By result of archaeological and archaeometric investigation, *unicum* object has been likely used as a reference to weigh the food in ritual practices in which the meat was weighed distribution to ritual participated in the ritual.

The high resolution and high energy X-ray radiography carried out to bronze plate investigation allowed to readable their decorations present on the surface. This are important information for archaeological investigation.

4.4. Case study 4

Archeometric investigation of a bronze anthropomorphic couples as pendants

4.4.1. Introduction

Among the productions of bronze jewelry of the ateliers of southern Italy in the Early Iron Age, the pendants depicting a couple of male and female individuals in the act of embracing each other stand out for their symbolic-ideological and social connotations. They are necklace pendants, as can be seen from the only intact exemplar so far known from tomb 57 of the necropolis of Macchiabate (Francavilla Marittima).

Basing on typologies already elaborated, we can distinguish “type B”, in which the man, always represented on the left side, wraps his right arm around the woman’s body, keeping his hand on her right shoulder; the female figure embraces her companion in the same way. In some of the exemplars, the connotation of the sex of the two individuals is rendered plastically through a generic representation of the genitals: a uniform prominence of oblong shape characterizes the pelvis of the male figure, while the female figure is characterized by a slight inflection of the bronze surface just detected. Figure 4.4.1 shows “type B” small bronze statue coming from Pietrapaola (Cs).

The figure 4.4.2 shown “type A” pendant which was found in Bucita-Rossano archaeological site. It is distinguished by the complexity of the treatment of the two figures. In fact the two silhouettes occupy the same positions but with a gestural variant that is expressed in the upper limbs: the curvilinear left arm of the man with a curvilinear trend is stretched along the body and has the forearm facing the woman's pelvis with the hand, preserved only in a small part, resting on her belly. In

both exemplars, the figures, represented with their lower limbs bent, assume a seated posture, that has a considerable significance on the semiotic plane, in relation to the general interpretation of the representation. The heads, in this case separated, are distinguished by their slightly elongated spheroidal shape, with rounded eyes and mouth treated by a deep groove that seems to translate into a barely hinted smile. The posterior skull cap is outlined in a naturalistic and anatomically well delineated way, as can also be seen for the occipital septum of the muliebrous figure.

Type A, unlike type B, has separate heads and bodies, with a single point of contact at shoulder height.

Figure 4.4.1: Front (a) and back (b) of the “Type B” pendant

Figure 4.4.2: Front (a) and back (b) of the “Type A” pendant

Archaeological investigations have been expanded by scientific studies to get more information about manufacturing process and state of preservation of the findings. The chemical composition of the bronze alloy and physical-technical characteristics have been studied. Of great historical and archaeological interest, the finds “type A” and “type B” have been investigated using non-invasive procedures. To identify the chemical composition we used portable X-Ray Fluorescence Spectrometry. However, to understand the physical-technical characteristics we used X-Ray micro-tomography.

4.4.2. X-ray fluorescence spectroscopy

The XRF chemical investigation was performed to detect the different chemical nature between the two finds. The experimental setup is shown in table 4.4.1, it is the same for both samples.

Energy	50 keV
Voltage	50 kV
Current	700 μA
Collimator	0.65 mm
Exposition time	360

Table 4.4.1: XRF experimental setup

Six measuring points were selected on “type B” pendant for the chemical surface investigation. The first two are called B4-R and B6-R, they were acquired on abraded area devoid of the oxidation. The other four measuring points, referred to as B1-R, B2-R, B3-R and B5-R, were acquired on oxidation layer. The measures groups were averaged between them.

Below, in table 4.4.2, the atomic concentration values related to the mean of the spectra values are reported and compared.

"Type B"	Element	Oxidation-free layer (Conc./%)	Oxidation layer (Conc./%)
1	K kα	0.14 ± 0.08	0.08 ± 0.06
2	Ca kα	0.75 ± 0.19	1.96 ± 0.28
3	Ti kα	<0.01	0.01 ± 0.01
4	Cr kα	<0.01	<0.01
5	Fe kα	0.07 ± 0.01	0.15 ± 0.07
6	Co kα	0.08 ± 0.01	0.02 ± 0.04
7	Ni kα	0.11 ± 0.02	0.06 ± 0.02
8	**Cu** kα	**76.81 ± 2.29**	**33.85 ± 7.58**
9	Zn kα	0.28 ± 0.05	0.24 ± 0.14
10	As kα	0.06 ± 0.02	0.11 ± 0.05
11	Sr kα	<0.01	<0.01
12	Zr kα	0.06 ± 0.02	0.11 ± 0.01
13	Ag kα	0.26 ± 0.05	0.87 ± 0.15
14	Cd kα	<0.01	<0.01
15	**Sn** kα	**19.16 ± 1.70**	**57.01 ± 6.39**
16	Sb kα	0.70 ± 0.11	1.36 ± 0.43
17	**Pb** Lα	**1.54 ± 0.34**	**4.17 ± 1.24**
18	Bi Lα	<0.01	<0.01

Table 4.4.2: Comparison between the atomic concentration values of the elements present on the oxidation layer (average between the B1-R, B2-R, B3-R and B5-R spectra) and on the abraded surface without oxidation (average between the B4-R and B6-R spectra) of the find "Type B"

By analyses of the spectra acquired on oxidation-free surface, we can confirm the bronze nature of the “type B” pendant. A binary alloy consisting of 76.81% copper and 19.16% tin was used, including presence of secondary metals such as lead (1.54%), antimony (0.70%), zinc (0.28%), silver (0.26%), nickel (0.11%) and trace elements such as iron (700 ppm), arsenic (600 ppm), zirconium (600 ppm) and cobalt (800ppm). While titanium, bismuth, cadmium, strontium and chromium are present at concentrations below 100 ppm.

However, the spectra acquired on oxidized surface revealed greater quantities of major elements, such as copper (33,85%), tin (57,01%) and lead (4,17%). This increase in tin and lead quantities could be due to the superficial decuprification phenomenon, [82]–[84] which consist in superficial migration of copper ion as a result of leaching of corrosion products (run-off). The result is a relative enrichment on the surface of the other alloying elements. This phenomenon is well present both on underground bronzes and exposed to the outside. [85], [86]

Two histograms, that compare the data relating to the two series of measurements, are show in figure 4.4.3 and 4.4.4.

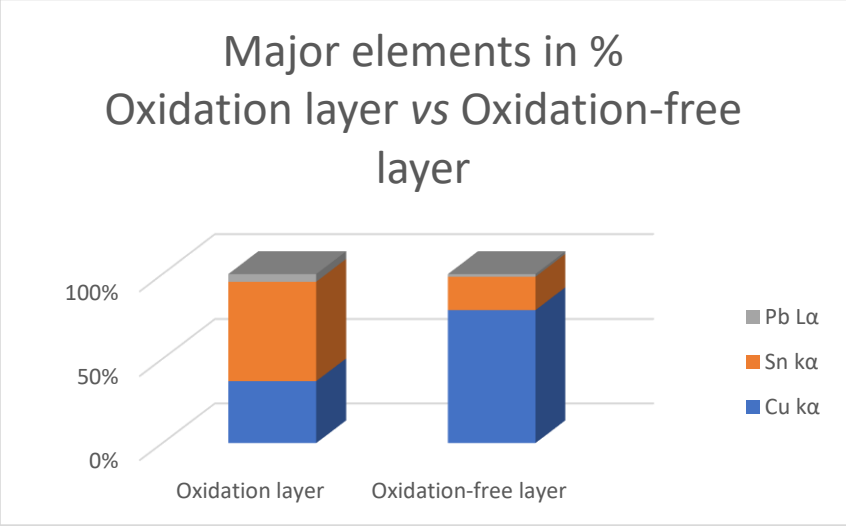

Figure 4.4.3: Histogram of the major elements present in oxidation layer and in oxidation-free layer of the "Type B" find

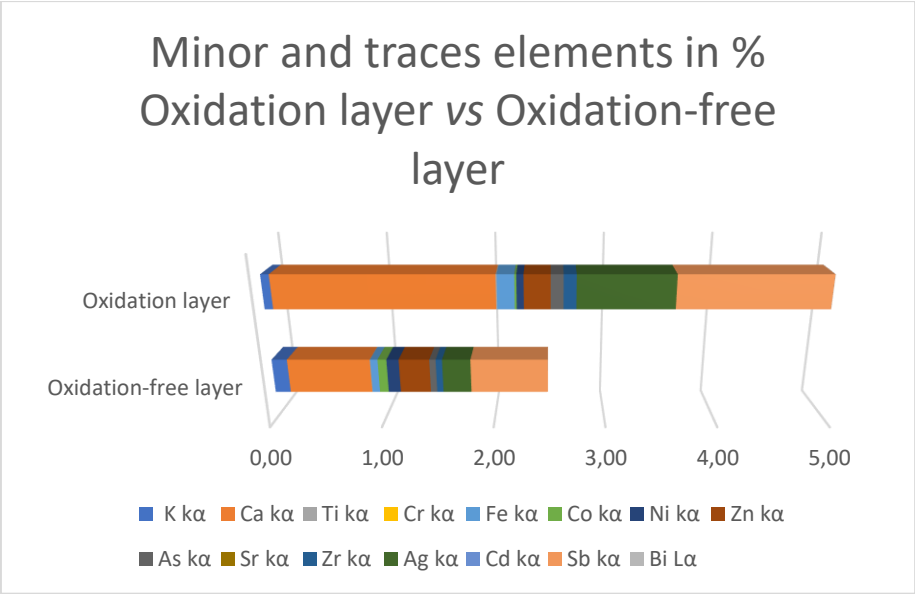

Figure 4.4.4: Histogram of the minor and traces elements present in oxidation layer and in oxidation-free layer of the "Type B" find

Four measuring points were selected on “type A” pendant for the chemical surface investigation. The spectra to B1-R, B2-R, B3-R and B5-R points were averaged between them. The relative average percentage values of the chemical elements present are given in table 4.4.3.

"Type A"	Element	Average measures (Conc./%)
1	Si kα	2.86 ± 1.24
2	Cl kα	0.49 ± 0.27
3	K kα	0.77 ± 0.56
4	Ca kα	0.38 ± 0.07
5	Ti kα	0.06 ±0.05
6	Mn kα	0.01 ± 0.02
7	Fe kα	0.27 ± 0.19
8	Co kα	0.12 ± 0.05
9	Ni kα	0.09 ± 0.02
10	**Cu** kα	**84.92 ± 4.26**
11	Zn kα	0.28 ± 0.06
12	As kα	0.02 ± 0.01
13	Sr kα	<0.01
14	Ag kα	0.27 ± 0.22
15	**Sn** kα	**7.38 ± 2.92**
16	Sb kα	1.20 ± 0.28
17	Pb Lα	1.02 ± 0.89
18	Bi Lα	<0.01

Table 4.4.3: Mean values of the atomic concentration of the elements present on "type A" surface

By analyses of the spectra acquired on "type A" surface, we can confirm their bronze nature. A binary alloy consisting of 84.92% copper and 7.38% tin was used, including presence of secondary metals such as lead (1.02%), antimony (1.20%), zinc (0.28%), silver (0.27%), cobalt (0.12%) and iron (0.20%) and nickel (900ppm), titanium

(600ppm) and arsenic (200ppm). While bismuth and strontium are present at concentrations below 100 ppm. The presence of chlorine, associated with the presence of patinas, suggests that there is a process of formation of oxidation products such as Nantochite, Atacamite, Paratacamite or Bollachite. [66], [82], [91], [83]–[90]

Table 4.4.4 shows the percentage values of the chemical elements present in “type B” and “type A” pendants. Figures 4.4.5 and 4.4.6 show two histograms of the percentage concentration values of the chemical major and secondary elements respectively present in “type B” and “type A” pendants

No.	**Element**	**Type A (Conc./%)**	**Type B (Conc./%)**
1	**Cu** kα	**84.92 ± 4.26**	**76.81 ± 2.29**
2	**Sn** kα	**7.38 ± 2.92**	**19.16 ± 1.70**
3	Pb Lα	1.02 ± 0.89	1.54 ± 0.34
4	Sb kα	1.20 ± 0.28	0.70 ± 0.11
5	Fe kα	0.27 ± 0.19	0.07 ± 0.01
6	Ag kα	0.27 ± 0.22	0.26 ± 0.05
7	Zn kα	0.28 ± 0.06	0.28 ± 0.05
8	Co kα	0.12 ± 0.05	0.08 ± 0.01
9	Ni kα	0.09 ± 0.02	0.11 ± 0.02
10	Ti kα	0.06 ± 0.05	<0.01
11	Bi Lα	<0,01	<0.01

12	Cd kα	----------	<0.01
13	As kα	0.02 ± 0.01	0.06 ± 0.02
14	Sr kα	<0.01	<0.01
15	Zr kα	----------	0.06 ± 0.02
16	Cr kα	----------	<0,01
17	Cl kα	0.49 ± 0.27	----------
18	Si kα	2.86 ± 1.24	----------
19	Ca kα	0.38 ± 0.07	0.75 ± 0.19
20	K kα	0.77 ± 0.56	0.14 ± 0.08
21	Mn kα	<0.01	----------

Table 4.4.4: percentage values of the chemical elements present in “type A” and “type B” pendants

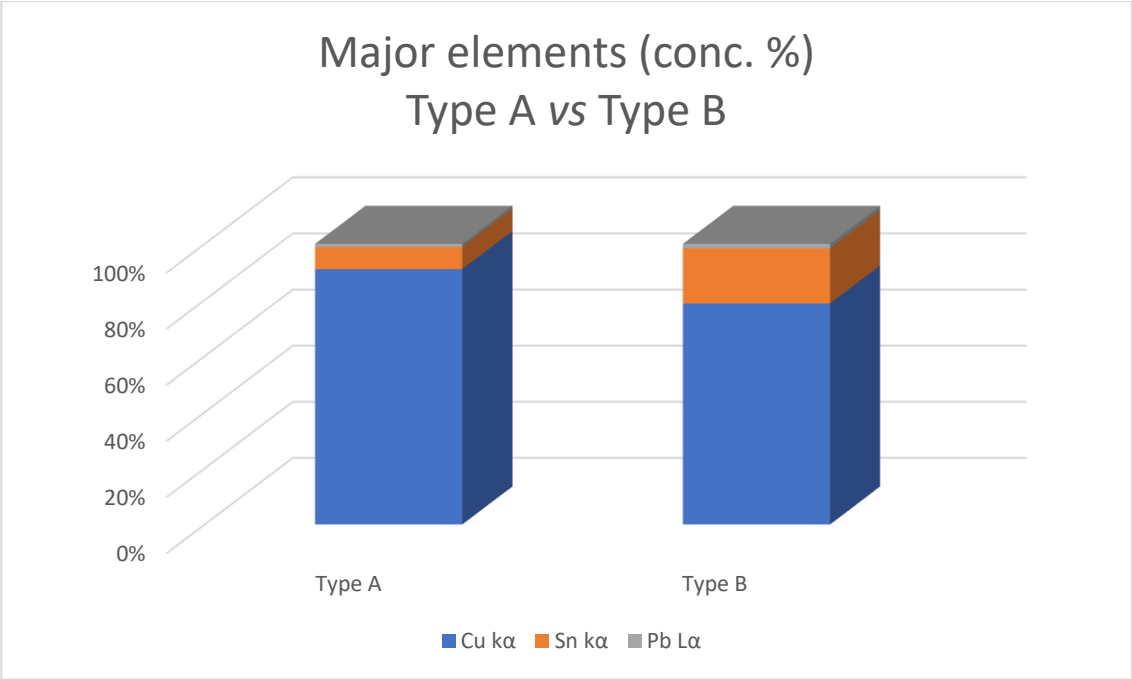

Figure 4.4.5: histogram of the percentage values of the chemical major elements concentration present in “type B” and “type A” pendants

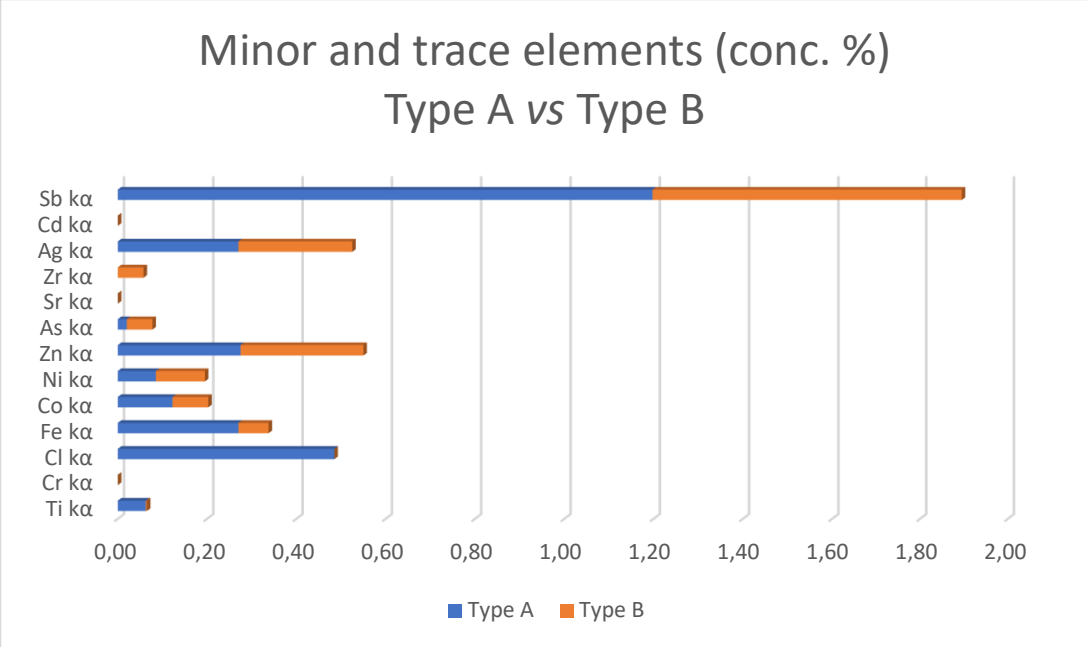

Figure 4.4.6: histogram of the percentage values of the chemical minor and trace elements concentration present in “type B” and “type A” pendants

4.4.3. X-ray microtomography

The X-ray microtomography surveys of the “type B” and “type A” pendants showed a series of peculiarity non-appreciable by visual investigations. This physical methodology has allowed to advance hypotheses on finds construction methods and their conservation status.

The measurements parameters are shown in table 4.4.5.

Voltage	50 KV
Current	66 µA
Focal spot	Small
Exposure time for each projection	2.5 s
Filter	3 mm Al + 25 µm Cu
Magnification	2
Pixel size	25 µm
Number of projections	1800
Step	0.2°

Table 4.4.5: X-ray microtomography measurements parameters

Figure 4.4.7 shows a X-ray image of the “type B” pendant. The red arrow indicates a lesion of the area between the bust of the female figure and that of the male figure. It isn’t possible to say whether this lesion was caused by alloy shrinkage phenomena during cooling phase or as a result of impacts occurred during excavation operations. In any case, its detection gives indications on the state of conservation of the artifact. The red circle shown in same figure, indicated a less X-ray absorption area between the two heads.

Figure 4.4.7: X-ray image in which the arrow indicates a lesion, while the circle highlights an area with less X-ray absorption_"type B"

The less X-ray absorption area between the two heads has been better analyzed in X-ray microtomographic reconstructions. By performing a segmentation operation of grey levels, it was possible to separate the contribution of the area under examination from that of the two heads. Figure 4.4.8 shows four rendering 3D at different grey levels segmentation of male and female heads area. Both heads have a regular and roundish shape even below the intermediate layer. The XRF measurements carried out on these areas showed no substantial differences from the rest of the find in terms of the chemical elements present and their concentrations. Also the X-ray microtomographic reconstructions have not evidenced presence of materials or structures other than the bronze alloy. [92]–[95]

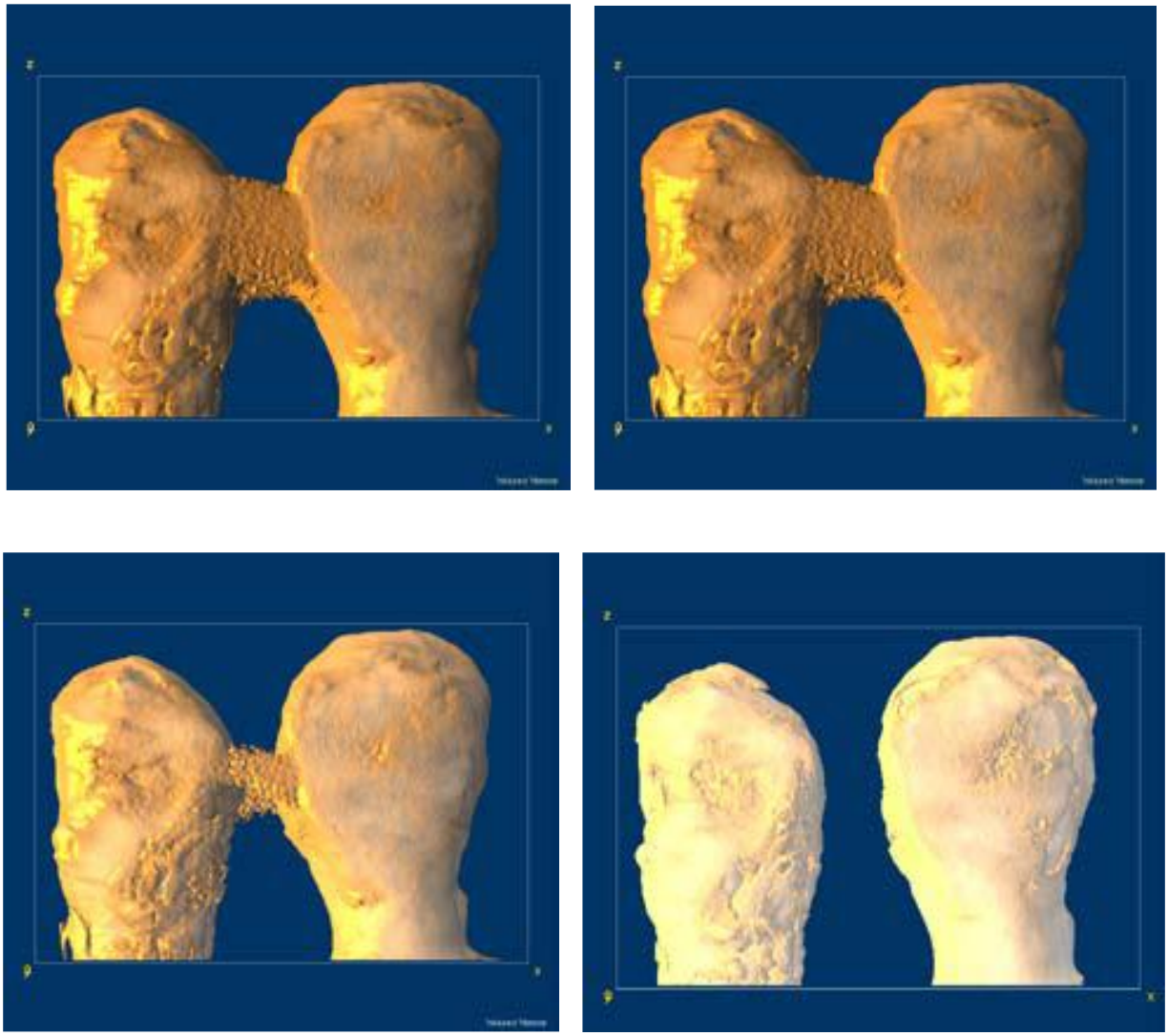

Figure 4.4.8: 3D tomographic reconstruction of the upper part at different levels of segmentation__”type B”

Figures 4.4.9 and 4.4.10 show two different 3D virtual sections of the central part of the "type B" find in the visualization of Imagej Volume Viewer tool. To the left of each image the cutting planes are displayed. The red circle indicates the area of union between the bust of the female figure and the bust of the male figure, in which the lesion already seen in the X-ray of figure 4.4.7.

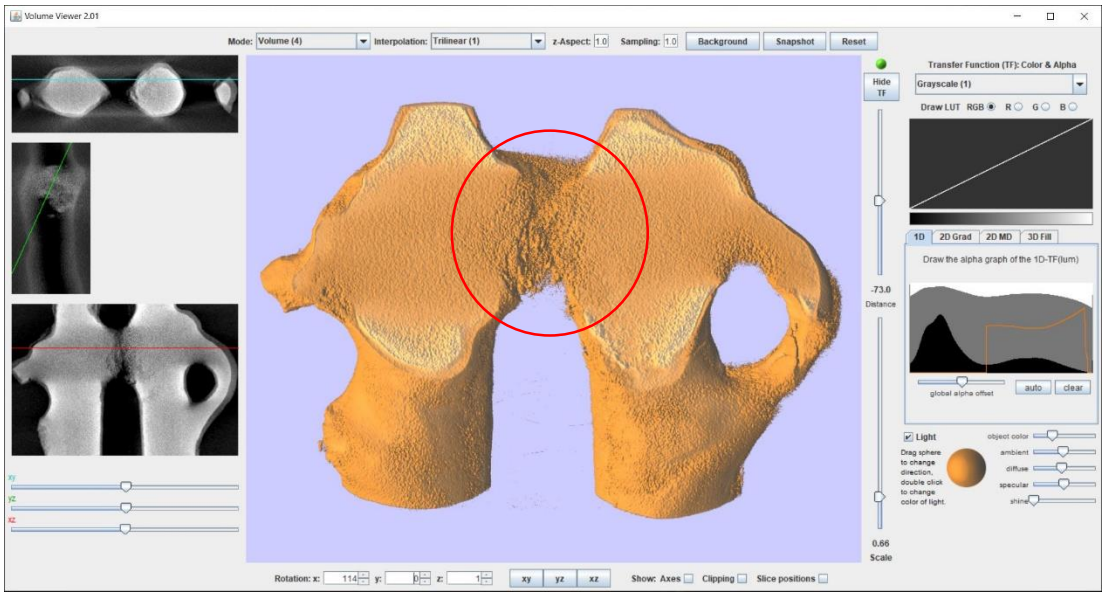

Figure 4.4.9: virtual section displayed using Imagej Volume Viewer tool of the middle area. The red circle indicates the area of union between the bust of the female figure and the bust of the male figure_"type B"

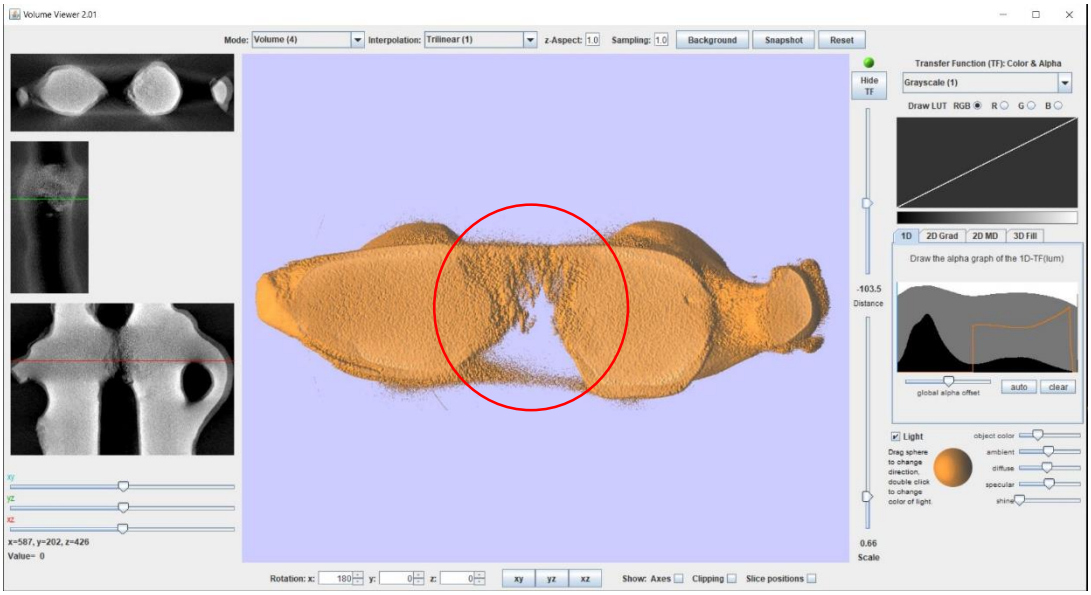

Figure 4.4.10: virtual section displayed using Imagej Volume Viewer tool of the middle area. The red circle indicates the area of union between the bust of the female figure and the bust of the male figure_"type B"

The figure 4.4.11 shows a X-ray images of the "type B" pendant, in which the red line shown a fracture that follows a single and linear direction at the both necks.

Figure 4.4.11: X-ray image in which the red line shown a fracture that follows a single and linear direction at the both neck_”type A”

This fracture is better investigated in X-ray microtomographic reconstructions (see 3D virtual section of the "type A” pendant upper portion in figure 4.4.12) in which are clearly seen that it follows a linear pattern on a single direction, has borders with sharp edges and no micro-lesions. These data suggest that the cut has taken place in a net way and at the same time for both heads, assuming an accidental breakage occurred in fairly recent times, perhaps during the recovery operations. The two heads are, at the moment, approximately glued together.

Figure 4.4.13 shows 3D reconstruction of the "type A" pendant upper portion in which two circular holes are visible at the both necks. The two holes, not visible to the naked eye because obliterated by sediments and encrustations, have a diameter of 2 mm, a very regular cylindrical section and lie on the same axis. The holes, made during the creation of the object, were most likely used to pass a lanyard that allowed the use of the object as a pendant.

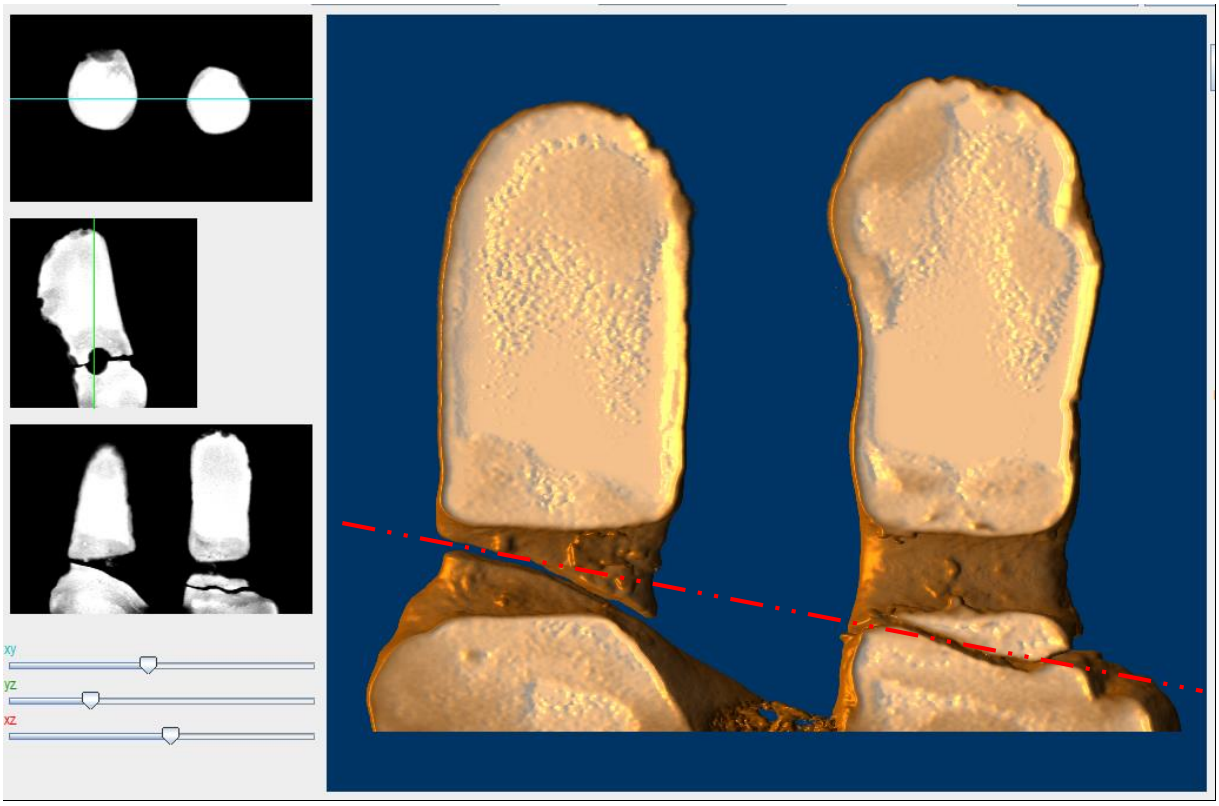

Figure 4.4.12: 3D virtual section of the frontal profile of the male and female heads in which the holes and fractures at the necks are well evident_"type A"

Figure 4.4.13: 3D reconstruction of the left side of the find in which the holes present in proximity to the necks are evident. It is clear that the holes are a very regular cylindrical section and lie on the same axis_”type A”

Figure 4.4.14 shows a 3D reconstruction of the female and male busts in which the outer arms are separated from the bust. As well as the necks holes, this detail is not visible to the naked eye because obliterated by sediments and encrustations.

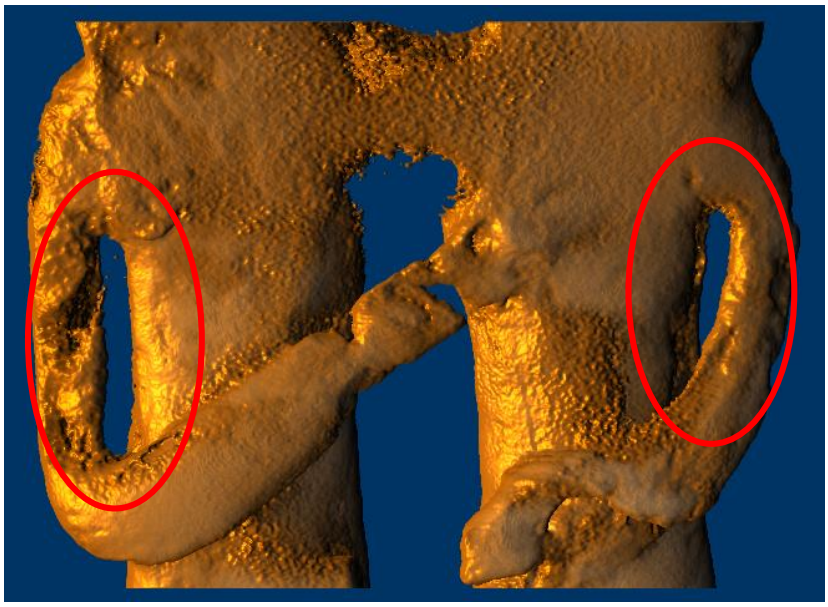

Figure 4.4.14: 3D reconstruction of the female and male busts in which is clearly visible that the outer arms are separated from the bust. This detail is not visible to the naked eye because obliterated by sediments and encrustations_”type A”

Figure 4.4.15 shows a 3D reconstruction in false colours of the "type A" pelvis and legs in which the knees and genitals are clearly evident. The 3D virtual sections of the same areas are shown in figures 4.4.16a-b-c and 4.4.17a-b.

The first two figures shows 3D internal virtual cross-sections of the legs near the knees where it is possible to observe how the kneecaps have a roundish shape with sharp edges. However, the knees are separated from the rest of the leg by a line that presents an absorption X-rays variation (indicated by black arrow in figure 4.4.16a-b). These features suggest that the knees have been made by additive method and by post-fusion mechanical machining. [92]–[95]

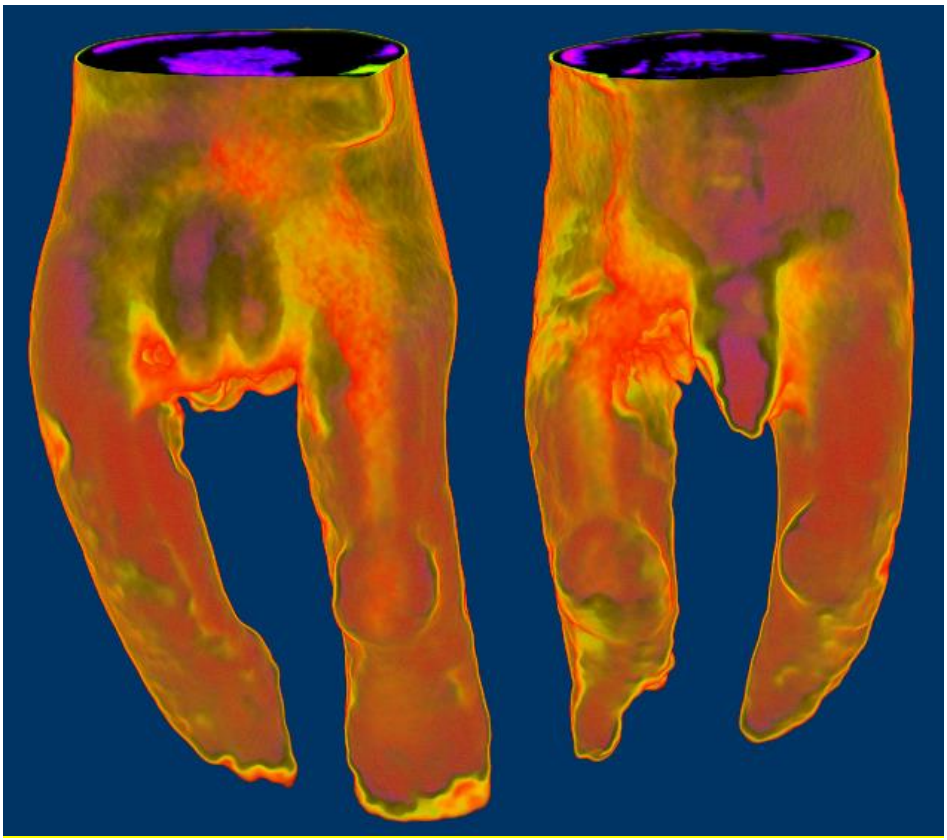

Figure 4.4.15: 3D reconstruction in false colours of the pelvis and legs areas_”type A”

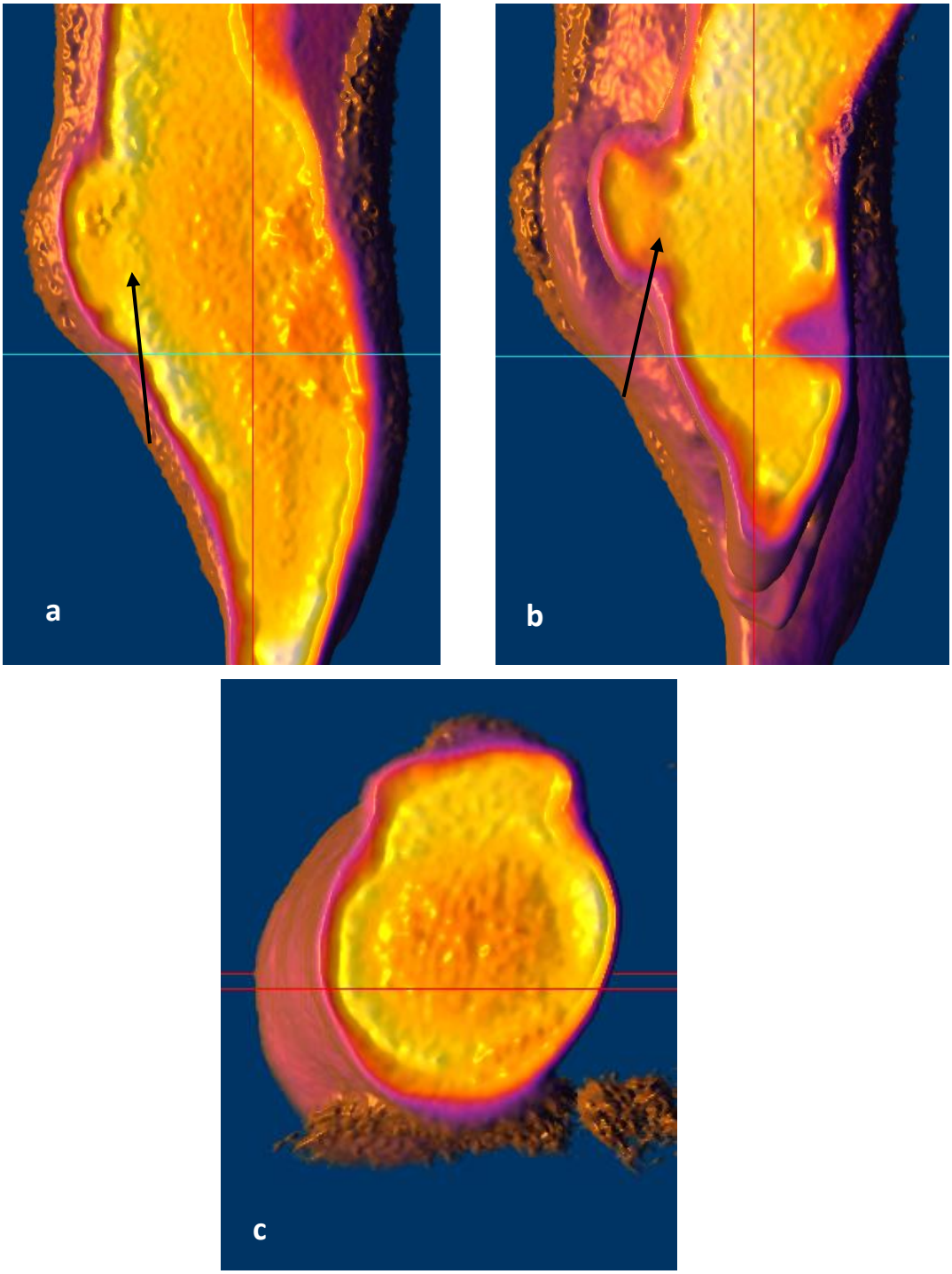

Figure 4.4.16: 3D virtual cross-section in false colours of the knees. Transversal section in which is present a line indicated by black arrow in which an absorption X-rays variation is valuable (a and b); longitudinal section in which is observed the roundish shape with sharp edges of the kneecaps (c)_"type A"

The figure 4.4.17 shows the 3D internal virtual cross-section in which is indicated by black arrows a series of lesion, voids and marks of working near the groin area. They

were probably produced during post-casting mechanical processing or by the presence of air bubbles during the alloy cooling phases.

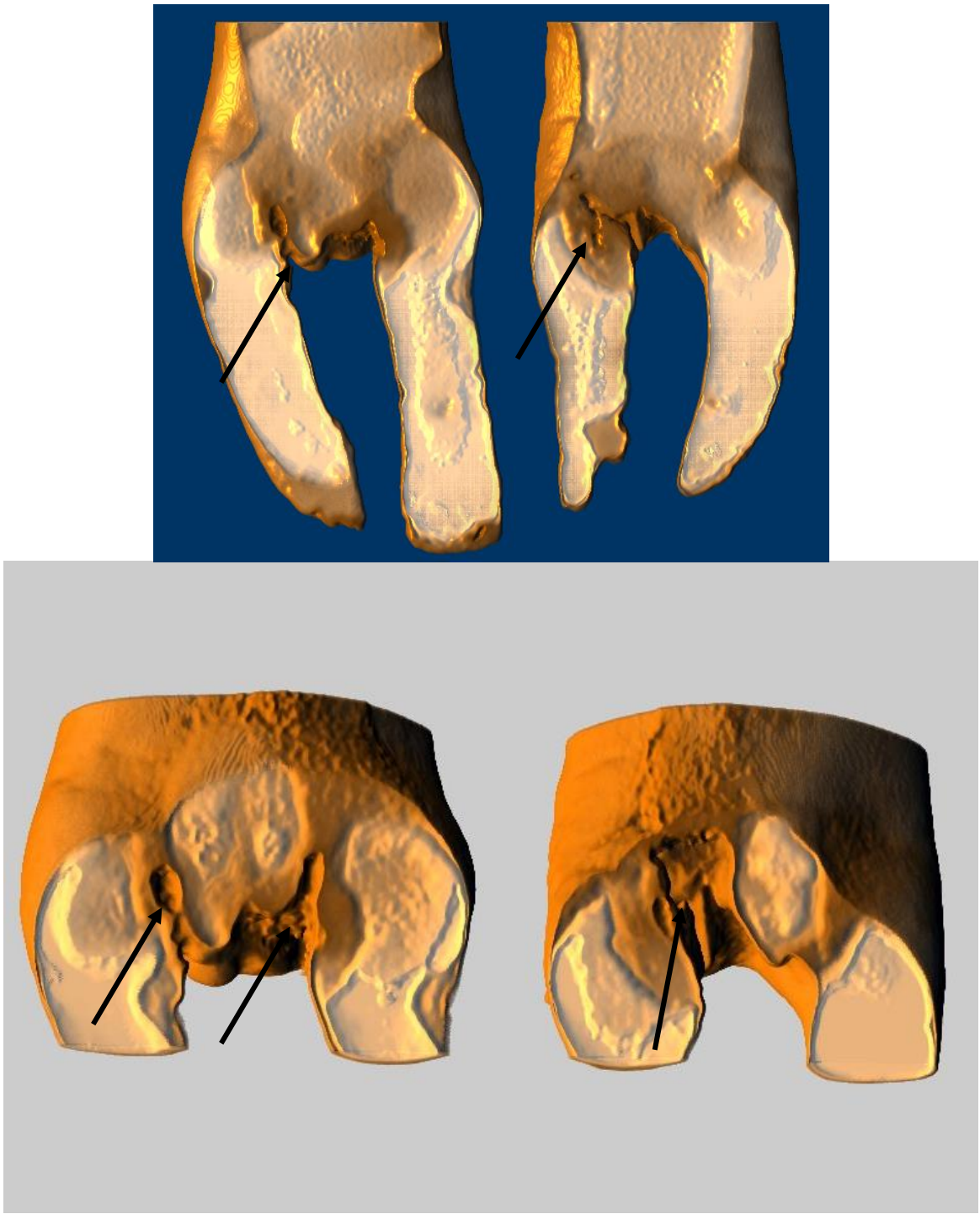

Figure 4.4.17: 3D virtual cross-section in which is indicated by black arrows a series of lesion, voids and marks of working near the groin area_ type A”

4.4.4. Conclusion

“Type A” and “Type B” bronzes anthropomorphic couples as pendants (dating to the Early Iron Age) have been studied by complementary physical methodologies means as X-ray microtomography and XRF portable spectroscopy. These completely non-invasive and non-destructive methods methodologies have allowed to characterize the constituent of materials and to advance hypotheses on their construction methods.

Both finds are made of a binary bronze alloy. The “type A” is made approximately of 85% copper and 7% tin, however the “type B” is made approximately of 77% copper and 19% tin. The secondary element as antimony is 1.20% in the “type A” and 0.70% in the “type B”, lead is 1.02% in the “type A” and 1.54% in the “type B”. Silver quantities are similar in both pendants. The iron greater quantities in “type A” are due probably to soil trace on find surface.

High tin content in bronze alloy like that of “type B” doesn’t allow post-fusion mechanical machining. Indeed, the malleability limit is achieved in upon 15% tin bronze alloy. [96]–[99] On the other hand, the same high tin content reduces the melting temperature and then reduces production times and costs. Moreover, the burrs in the “type B” statuette edges assume the double-valve mould casting. This method and the bronze alloy made of high Tin content are suitable for a fast and mass production. In contrast, “type A” is made of a binary bronze alloy that allows to post-fusion mechanical machining.

Decuprification phenomenon [82]–[84] is present on the “type A” surface and chloride is present in “type B” XRF result. So, several oxidation processes involved “type A” and “type B” pendants. It is due probably to their different making process and their different discovery site. Also different colours of oxidation patina prove this.

The X-ray microtomography reconstruction of the “type B” pendant shown a less X-ray absorption area between the two heads pendant. After performing a segmentation operation of grey levels, the contribution of the area under examination and that of the two heads are separated. Both heads have a regular and roundish shape even below the intermediate layer. The XRF measurements carried out on these areas showed no substantial differences from the rest of the find in terms of the chemical elements present and their concentrations. Also the X-ray microtomographic reconstructions have not evidenced presence of materials or structures other than the bronze alloy. The difference in X-ray absorption of the area in question is therefore caused probably by a lower density of the alloy have been combined during casting process.

The X-ray microtomography reconstruction of the “type A” pendant were allowed to discover a series of details which was hidden by soil residues and encrustations. In particular, 3D reconstruction of the upper portion shown two circular holes at the female and male necks. The two holes, not visible to the naked eye because obliterated by sediments and encrustations, made during the creation of the object and were most likely used to pass a lanyard that allowed the use of the object as a pendant. Moreover, the female right arm and the male left arm are separated from the bust. As well as the necks holes, this detail is not visible to the naked eye.

In the “type A” pendant a series of lesion, voids and marks of working near the groin area are visible and edges near arms, knees and genitals have undercuts. Moreover, the 3D reconstruction shown a different X-ray absorption strip between knees and legs. These features assume that the implementation of these anatomic details occurred by post-fusion mechanical machining and by additive and subtractive method.

4.5. Case study 5

Archaeometric investigation of 12 Magno-Greek bronze mirrors conserved at the National Archaeological Museum of Locri Epizefiri

4.5.1. Introduction

The bronze mirrors under physical investigation are preserved in the National Archaeological Museum of Locri Epizephyrii. They were discovered during the exploration of the Necropolis of Contrada Lucifero, they are the most interesting archaeological finds brought to light during the excavations in the ancient Locri Epizephyrii polis.

These objects frequently appears in the grave goods between the second half of the VI century b.C. and the first half of the IV century b.C.

These prestige goods are a clear example of the high level reached by the handicraft of Magna Graecia.

Usually, they consist in three parts: a circular bronze disc, a bronze support often finely worked ending in a tang to which an organic handle was attached.

Their handles are particularly important since they record a lot of interesting information regarding the artistic expressions of their age and, moreover, regarding how the bronze was worked during that age helping us to understand the techniques that were used to build the bronze statues which didn't ever reach our age and, of which, those mirrors are a representation at a smaller scale

Aims of this work are study the conservation status and chemical composition of the 12 Magno-Greek bronze mirror through non-destructive physical investigations as photographic in UV light, X-ray radiography and X-ray fluorescence spectroscopy. In addition, 3D reconstructions through automated photogrammetry were made.

The 12 bronze mirrors are shown in figure 4.5.1 – 4.5.12.

Figure 4.5.1: Front (a) and back (b) of the n.919 bronze mirror. It was discovered in tomb 173 of the Lucifer Necropolis. Height 26.5 cm, disc diameter 16.5 cm

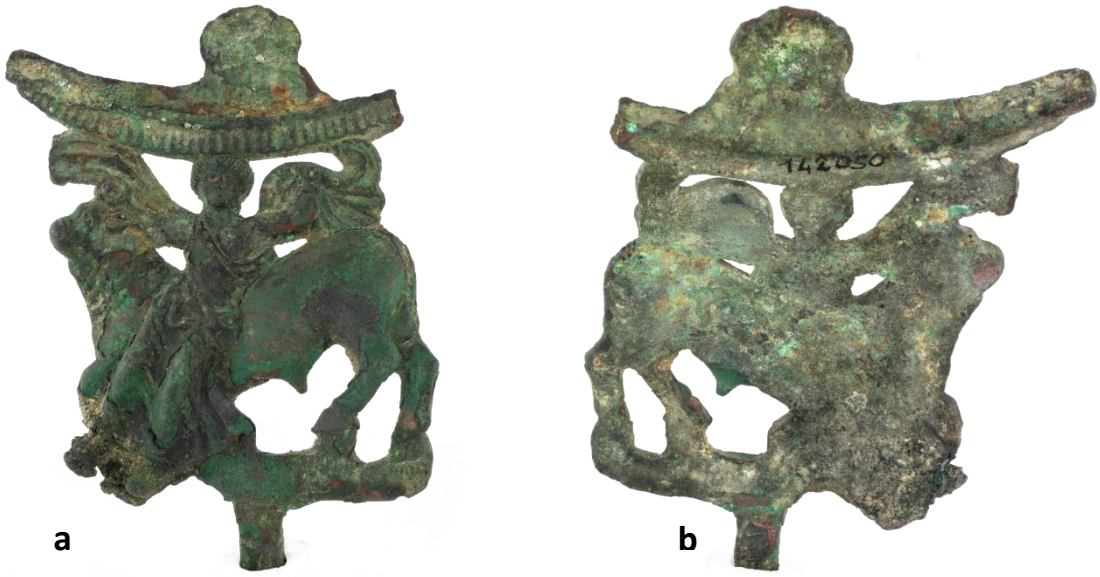

Figure 4.5.2: Front (a) and back (b) of the n. 142050 bronze mirror support. It represents Myth of Europe. Height 12 cm, width 8 cm

Figure 4.5.3: Front (a) and back (b) of the n. 916 bronze mirror. It was discovered in the Lucifer Necropolis. The support representing a nude and standing *keupos*. Height 30 cm, disc diameter 13.5 cm

Figure 4.5.4: Front (a) and back (b) of the n. 688 bronze mirror. It was discovered in tomb 1033 of the Lucifer Necropolis. Height 35 cm, disc diameter 16.5 cm

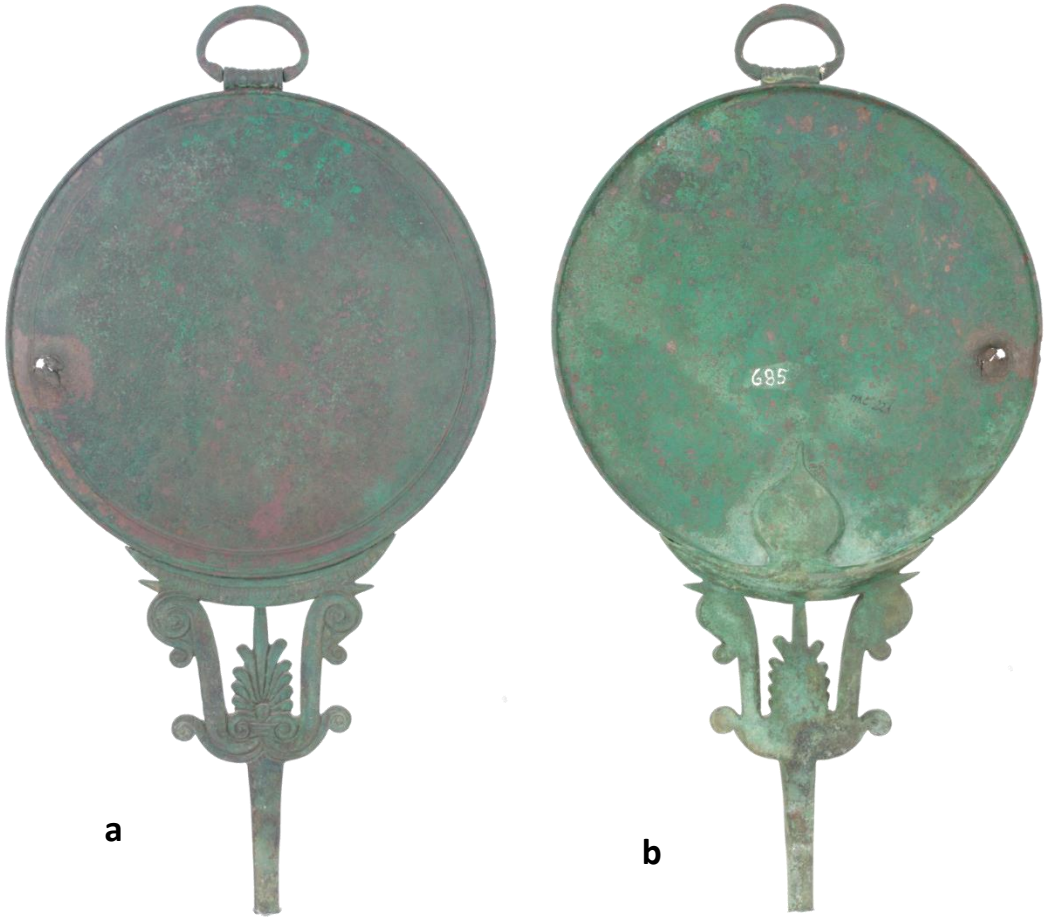

Figure 4.5.5: Front (a) and back (b) of the n. 685 bronze mirror. It was discovered in tomb 163 of the Lucifer Necropolis. Height 35 cm, disc diameter 18 cm

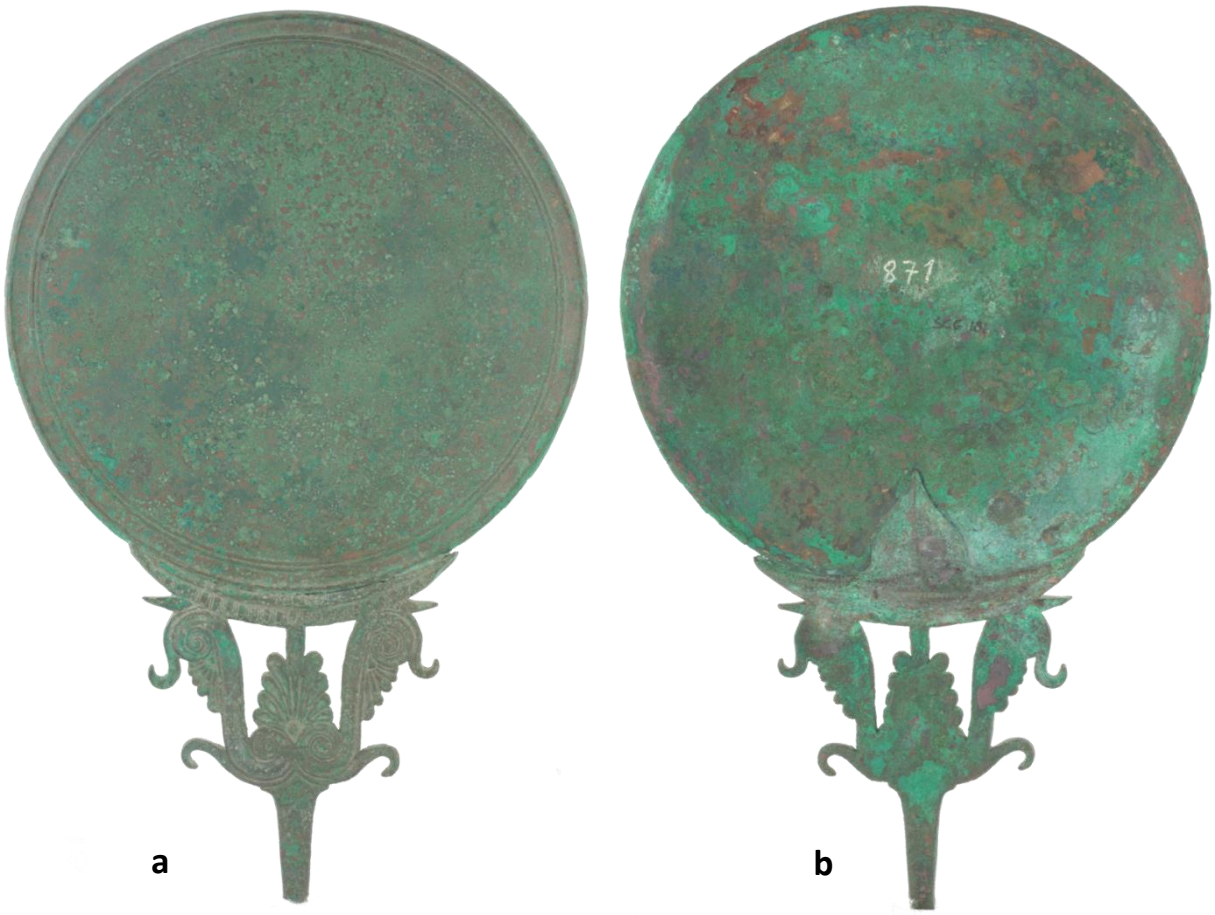

Figure 4.5.6: Front (a) and back (b) of the n. 871 bronze mirror. It was discovered in tomb 1312 of the Lucifer Necropolis. Height 28.5 cm, disc diameter 16.5 cm

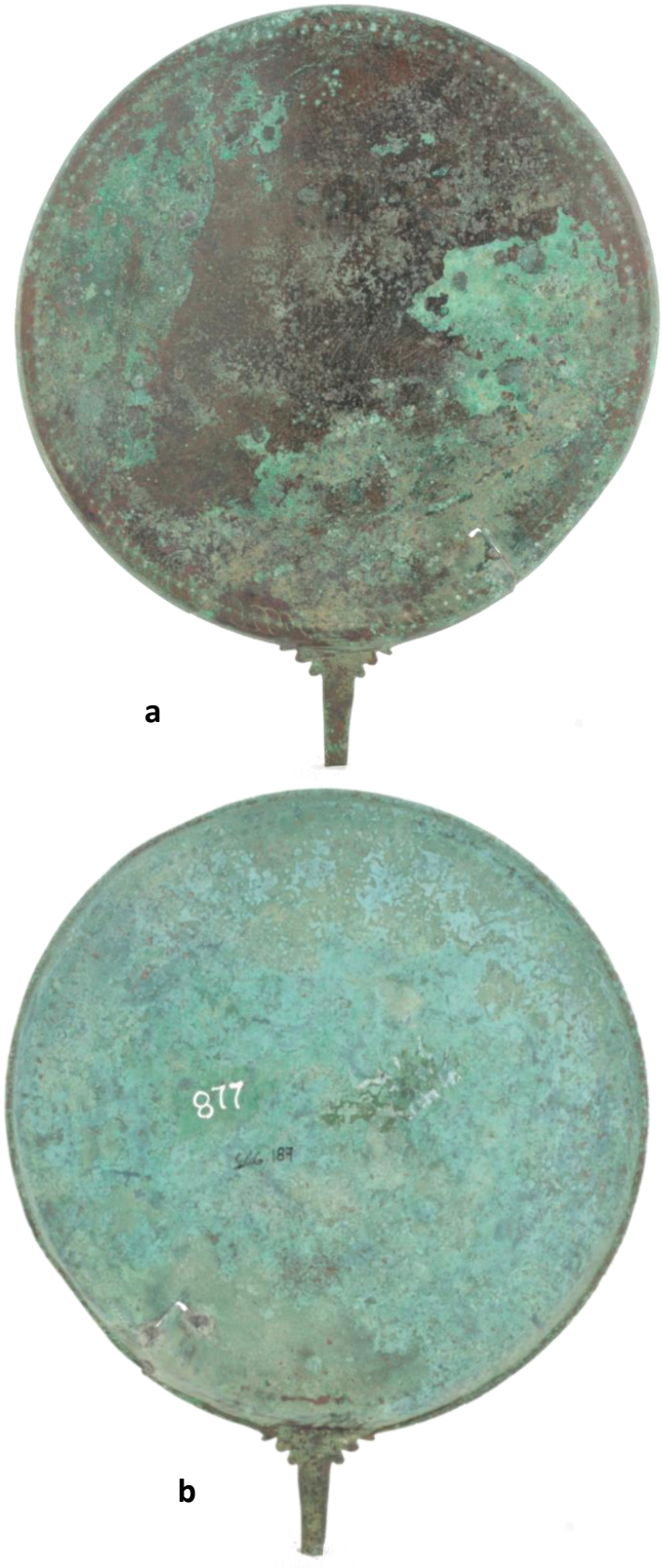

Figure 4.5.7: Front (a) and back (b) of the n. 877 bronze mirror. It was discovered in Lucifer Necropolis. Height 21 cm, disc diameter 15.5 cm

Figure 4.5.8: Front (a) and back (b) of the n. 911 bronze mirror support. It was discovered in Lucifer Necropolis. Height 20 cm, width 7.5 cm

Figure 4.5.9: Front (a) and back (b) of the n. 912 bronze mirror support. It was discovered in Lucifer Necropolis. Height 9 cm, width 8 cm

Figure 4.5.10: Front (a) and back (b) of the n. 918 bronze mirror. It was discovered in Lucifer Necropolis. Height 26 cm, disc diameter 16.5 cm

Figure 4.5.11: Front (a) and back (b) of the n. 915 bronze mirror support. It was discovered in tomb 645 of the Lucifer Necropolis. Height 10 cm, width 8 cm

Figure 4.5.12: Front (a) and back (b) of the n. 1765 bronze mirror support. It was discovered in the Lucifer Necropolis. Height 18 cm, width 12 cm

4.5.2. Photographic investigation: UV light and 3D reconstructions

The photographic investigation under UV light led to detection of older restoration residue and trace. The n. 919 and n.916 bronze mirrors were exposed under UV light. They are shown in figure 4.5.13 and 4.5.14 respectively in which the fluorescent areas are due to the resins used in old restoration work.

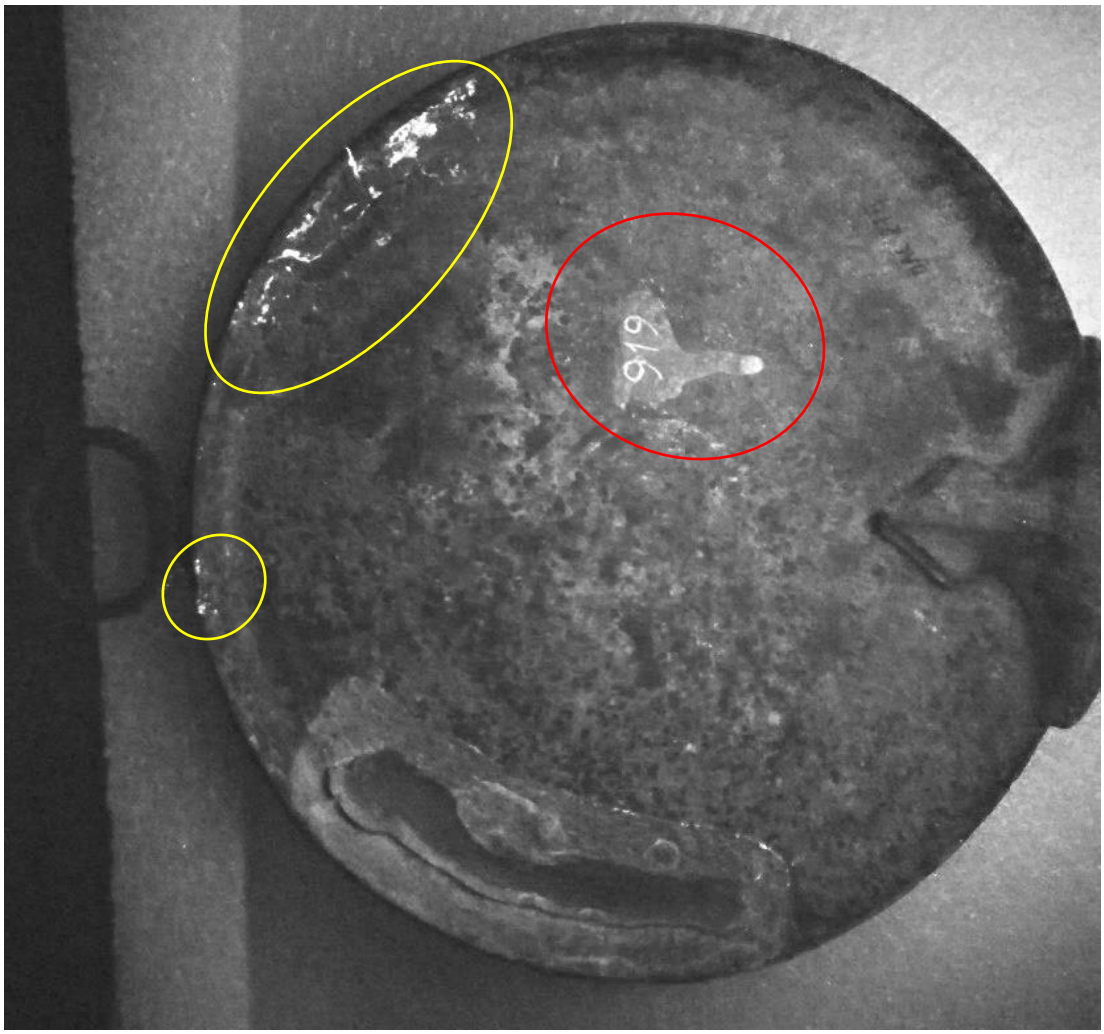

Figure 4.5.13: Back of the n.919 bronze mirror under UV light. Are visible a series of fluorescent areas due to glue and resin used in the restoration (yellow circles) and inventory (red circle) work.

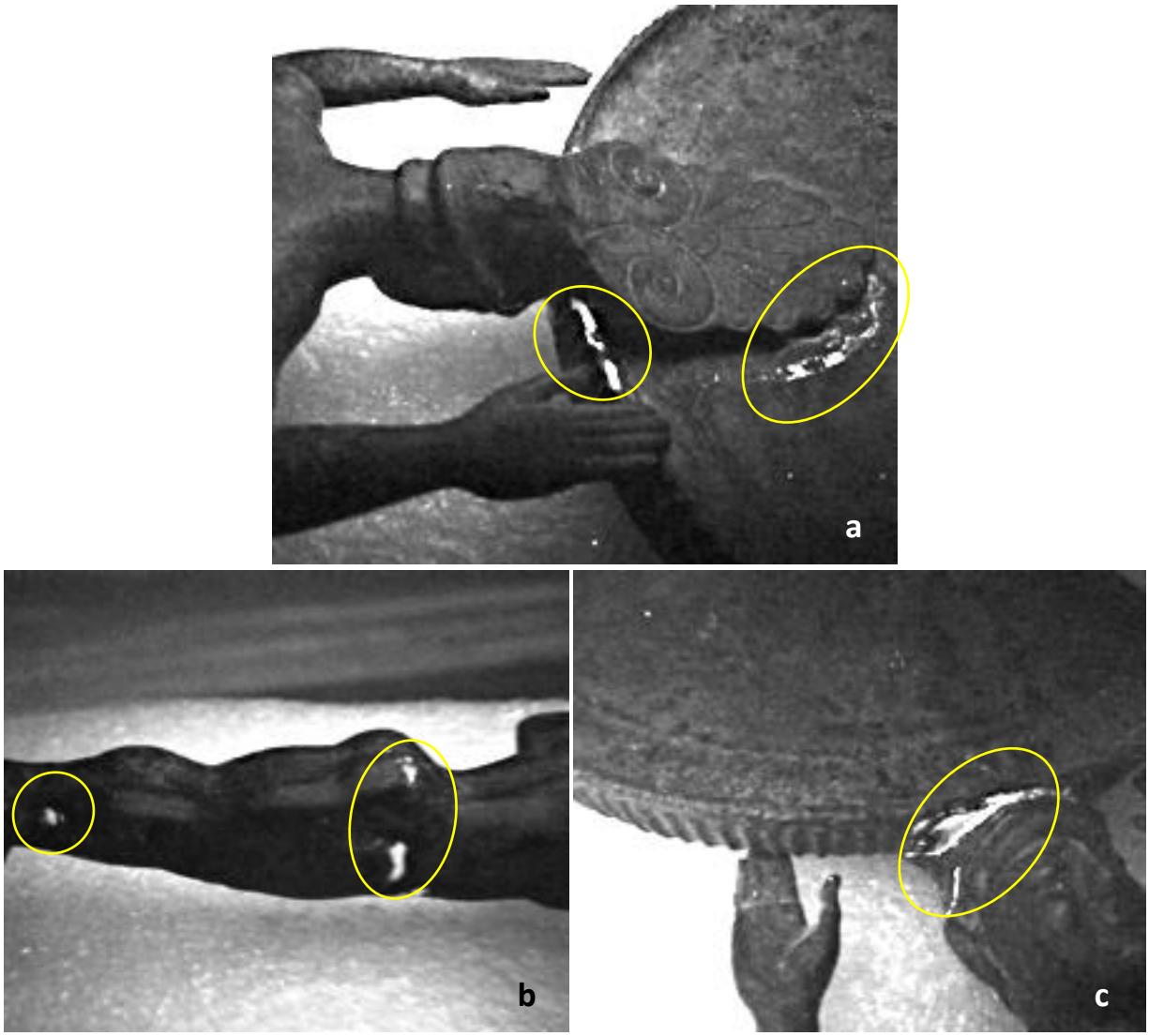

Figure 4.5.14: Back (a and b) and front (c) of the n.916 bronze mirror under UV light. Are visible a series of fluorescent areas due to glue used in the restoration work (yellow circles).

4.5.3. X-ray fluorescence spectroscopy

The XRF chemical investigation was performed to detect the different chemical nature between the finds. The experimental setup is shown in table 4.5.1, it is the same for all samples.

Energy	50 keV
Voltage	50 kV
Current	700 µA
Collimator	0.65 mm
Exposition time	300 s

Table 4.5.1: XRF experimental setup

Three measuring points were selected on each mirror surface, so they were averaged between them. Six measurements were carried out on the 142050 surface: three near a green surface and three near a black layer which is present in some areas of the surface of the mirror. The measurements points carried out on n.918, n.688, n.685, n.877, n.916, n.871 and n.919 mirrors are relative to the bronze circular disc, while the measurements points carried out on n.912, n.911, n.142050, n.915 and n.1765 mirrors are relative to bronze support.

In table 4.5.2 the atomic concentration values related to the mean of the spectra values acquired on mirrors surface are reported and compared.

Table 4.5.2 shown the percentage values of the chemical elements present in bronze mirrors. The figures 4.5.15 and 4.5.16 show two histograms of the percentage atomic concentration values of the chemical major and secondary elements respectively.

	ELEMENTS (CONC. %)														
	Cu kα	**Sn** kα	**Pb** Lα	**Fe** kα	**Co** kα	**Ni** kα	**Zn** kα	**Ga** kα	**As** kα	**Ag** kα	**Cd** kα	**Sb** kα	**Bi** Lα	**Cl** kα	**Ca** kα
871	75.66 (±4.50)	23.43 (±4.46)	0.40 (±0.14)	0.09 (±0.02)	0.08 (±0.02)	0.07 (±0.01)	0.21 (±0.11)	/	0.04 (±0.01)	/	/	/	/	/	/
685	85.00 (±1.28)	12.40 (±1.80)	0.17 (±0.03)	0.05 (±0.02)	0.03 (±0.02)	0.06 (±0.01)	0.19 (±0.05)	/	0.02 (±0.01)	/	/	/	/	2.08 (±0.71)	/
918	97.04 (±0.37)	2.19 (±0.39)	0.19 (±0.01)	0.21 (±0.03)	0.08 (±0.01)	0.06 (±0.01)	0.17 (±0.01)	/	<0.01	/	/	/	/	0.07 (±0.06)	/
877	83.03 (±5.17)	15.08 (±5.04)	0.30 (±0.17)	0.03 (±0.02)	/	0.15 (±0.01)	/	/	0.02 (±0.01)	/	/	/	/	1.38 (±0.36)	/
912	35.30 (±2.87)	30.42 (±0.82)	33.25 (±3.08)	0.23 (±0.01)	/	0.09 (±0.01)	0.06 (±0.01)	/	0.25 (±0.07)	0.27 (±0.01)	/	/	0.13 (±0.01)	/	/
1765	82.11 (±0.70)	6.94 (±0.44)	5.70 (±0.39)	0.61 (±0.04)	/	/	0.22 (±0.02)	/	0.06 (±0.01)	/	/	/	/	/	4.35 (±0.58)
911	61.03 (±3.39)	10.20 (±1.21)	27.22 (±3.05)	0.03 (±0.02)	0.04 (±0.01)	0.05 (±0.01)	0.08 (±0.01)	/	0.06 (±0.02)	/	/	/	0.01 (±0.01)	1.27 (±1.05)	/
915	83.30 (±0.59)	10.02 (±0.92)	4.54 (±0.05)	0.14 (±0.11)	/	/	0.30 (±0.12)	/	/	/	/	/	0.01 (±0.01)	/	1.55 (±0.62)
919	69.75 (±3.79)	26.20 (±2.52)	1.23 (±0.92)	0.44 (±0.10)	0.11 (±0.02)	0.05 (±0.01)	0.13 (±0.01)	/	0.01 (±0.01)	0.19 (±0.05)	/	/	/	/	1.87 (±0.54)

142050 green surface	49.06 (±10.97)	4.65 (±1.34)	45.11 (±12.09)	0.07 (±0.04)	0.04 (±0.02)	0.05 (±0.02)	0.07 (±0.02)	<0.01	/	0.10 (±0.04)	<0.01	0.08 (±0.03)	0.05 (±0.02)	/	0.74 (±0.51)
142050 black surface	81.81 (±5.66)	5.46 (±2.15)	8.25 (±1.59)	0.18 (±0.13)	/	/	0.75 (±0.94)	/	0.02 (±0.02)	/	/	0.19 (±0.05)	0.01 (±0.01)	1.56 (±1.44)	1.25 (±0.63)
916	81.01 (±11.27)	17.41 (±10.32)	0.15 (±0.10)	0.16 (±0.16)	0.16 (±0.12)	0.08 (±0.02)	0.23 (±0.01)	/	0.02 (±0.01)	0.10 (±0.05)	/	/	/	/	0.68 (±0.01)
688	88.13 (±2.22)	9.31 (±2.22)	0.19 (±0.09)	0.16 (±0.07)	/	/	0.27 (±0.15)	/	0.01 (±0.01)	0.04 (±0.04)	/	0.02 (±0.02)	/	1.04 (±0.25)	0.80 (±0.30)

Table 4.5.2: percentage values of the chemical elements present in bronze mirrors (/ is not present element)

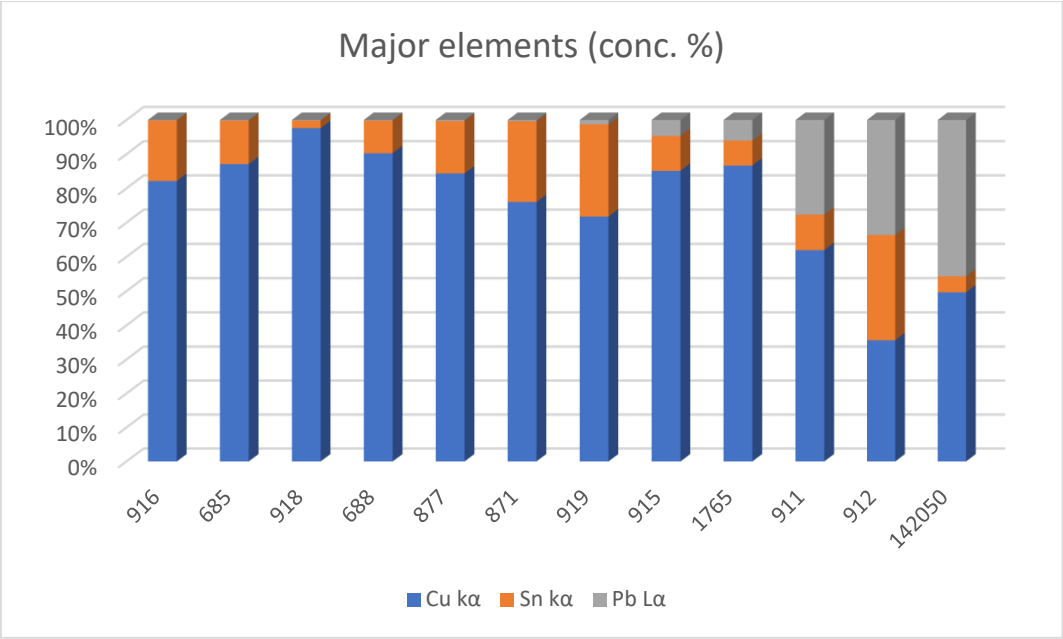

Figure 4.5.15: Histogram of the percentage atomic concentration values of the major chemical elements

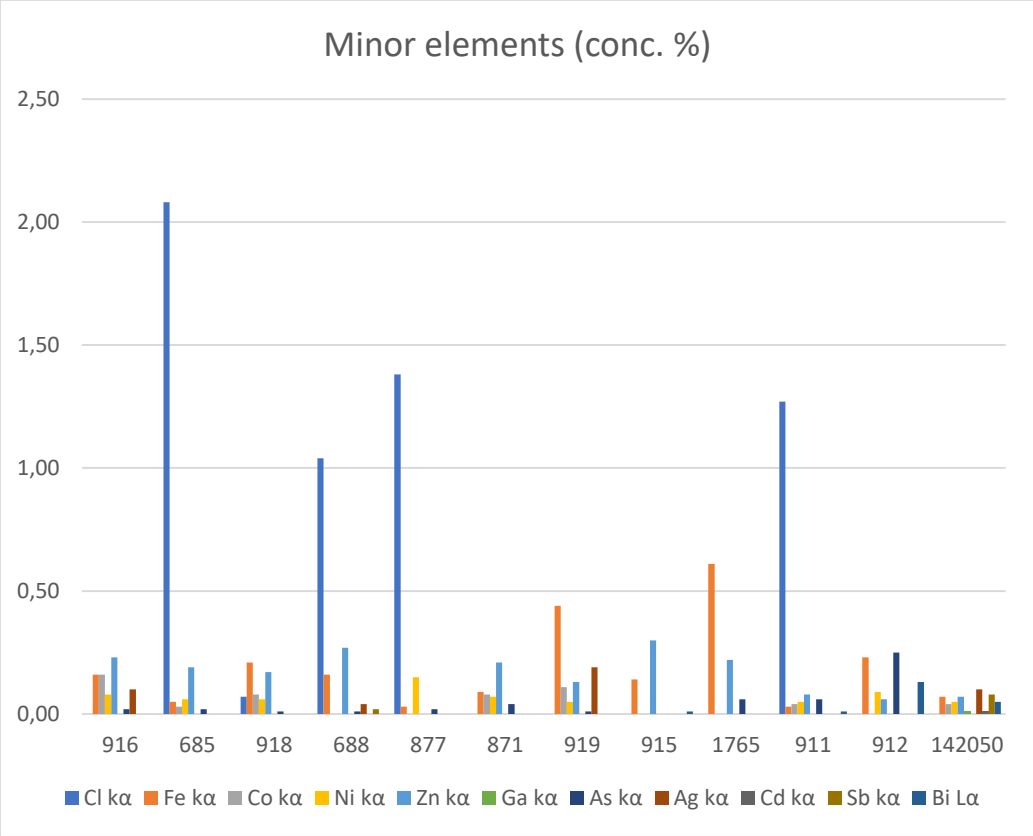

Figure 4.5.15: Histogram of the percentage atomic concentration values of the minor chemical elements

The major elements as Cu, Sn and Pb being plotted on a ternary diagram, are shown in figure 4.5.16. The diagram revealed three groups of mirrors whit similar chemical composition. In the first group (red circle) n.912, n.911 and n.142050 finds are present, in second group (blue circle) n.915 and n.1765 finds are present, therefore in the group in green circle n.918, n.688, n.685, n.877, n.916, n.871 and n.919 mirrors are present.

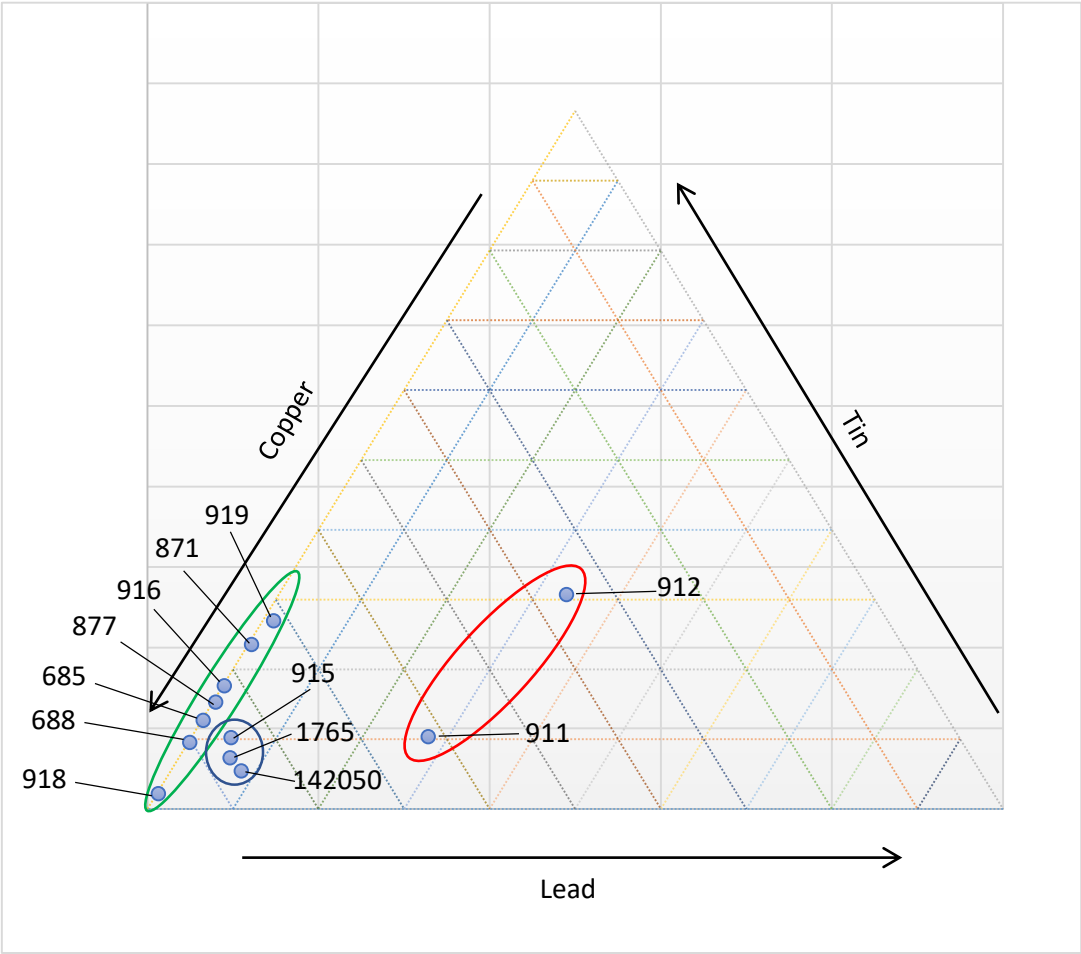

Figure 4.5.16: Ternary diagram of the major elements as Cu, Sn and Pb

From histograms and ternary diagram we can see that the circular bronze discs are made by a binary Cu-Sn bronze alloy (with different percentage concentration values

of tin between 2.19% and 26.20%), while the bronze supports are made by a ternary Cu-Sn-Pb bronze alloy (with different percentage concentration values of lead between 4.54% and 33.25%). When lead is added to tin-bronze, the resulting leaded bronze alloy is rendered softer and more malleable, which simplifies and facilitates chisel work on fine details. [100]

A leaded copper alloy with high percentages of lead was not suitable for extensive cold-working because the metal cracked and fragmented upon continuous hammering. The same brittleness occurs when a high amount of lead is added to bronze, because lead is soluble in tin bronze only to a limited extent. [101] Lead is soluble only up to a certain degree in tin bronze, which limits the homogeneity of the liquid. As an example, bronze that contains 10% by weight of tin can dissolve up to 17% by weight of lead. Lead tends to collect along the grain boundaries of the copper/tin crystals and actually acts as a lubricant that improves the fluidity of the metal. The lubricating property of leaded bronze enables the liquid metal to fill complex moulds more completely than a tin/copper mixture. [102] So, in n. 911 and n. 912 the increase in lead quantities could be due to the superficial decuprification phenomenon [82]–[84], which consist in superficial migration of copper ion as a result of leaching of corrosion products (run-off). The result is a relative enrichment on the surface of the other alloying elements. This phenomenon is well present both on underground bronzes and exposed to the outside. [85], [86]

The presence of chlorine, associated with the presence of patinas, suggests that there is a process of formation of oxidation products such as Nantochite, Atacamite, Paratacamite or Bollachite. [66], [82], [91], [83]–[90]

4.5.4. X-ray radiography

The X-ray radiography carried out on n.919, n. 142050, n. 916 and n. 688 mirrors allowed to acquire information about their state of preservation.

The measurements parameters are shown in table 4.5.3.

Voltage	150 KV
Current	180 µA
Focal spot	Middle
Exposure time for each radiograph	1.5 s
Filter	50 µm Mo
Magnification	2
Pixel size	25 µm
Number of projections	1800
Step	0.2°

Table 4.5.3: X-ray microtomography measurements parameters

Figure 4.5.17 shown X-ray radiography of n. 142050 mirror in which the red arrows point to a less compact sample area, below which the feet of Europa goddess are clearly visible.

Figure 4.5.16: X-ray radiography of n. 142050 mirror in which the red arrows points to a less compact sample area

The n.919, n. 916 and n. 688 mirrors size are greater than detector, so X-ray radiography was acquired in six parts for each mirror. Later, the radiographs were combined by *"stitching"* tool of Imagej software.

Figure 4.5.17a shows a radiography of n. 919 mirror. Figure 4.5.17b and figure 4.5.17c are two magnifications of the previous image: in the first one the corrosion phenomenon as called pitting is visible, [103]–[106] while the second figure shows a circular hole at the centre of the bronze disc, it was made probably by the craftsman.

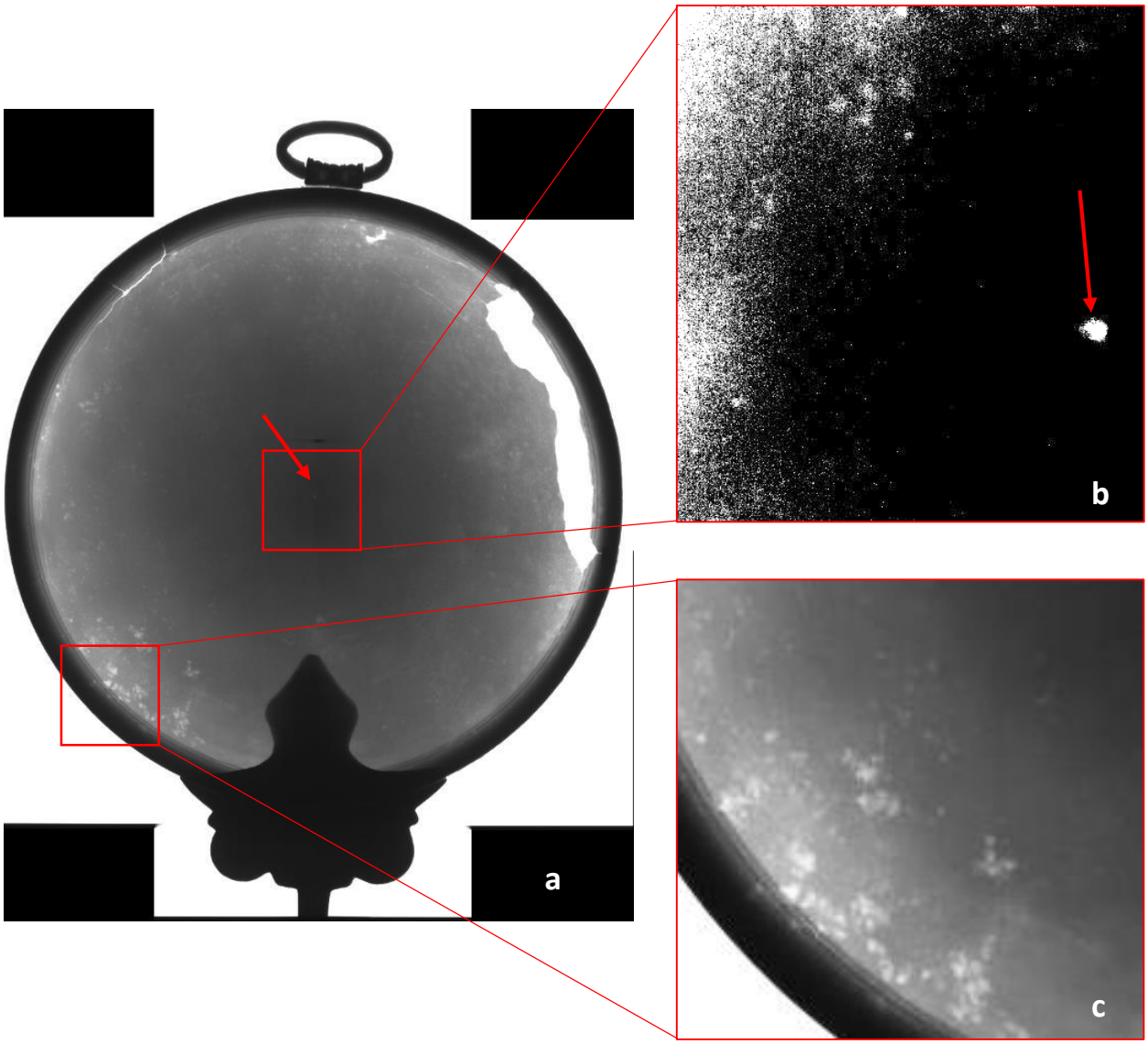

Figure 4.5.17: X-ray radiography of n. 919 mirror (a); magnification of previous radiography image in which is visible the pitting phenomenon (b); magnification of previous radiography image in which a circular hole at the center of the bronze disc is visible (c).

Figure 4.5.18 shows the radiography of the top of n. 919 mirror, near the point of the suspension ring attack. The red arrow shows a highly X-ray transparent area. It is a resin used to bond suspension ring to circle disc. The red circle in the same figure shows a peculiarity of the bronze spool. It is not a hollow cylinder but it has one hole in each end.

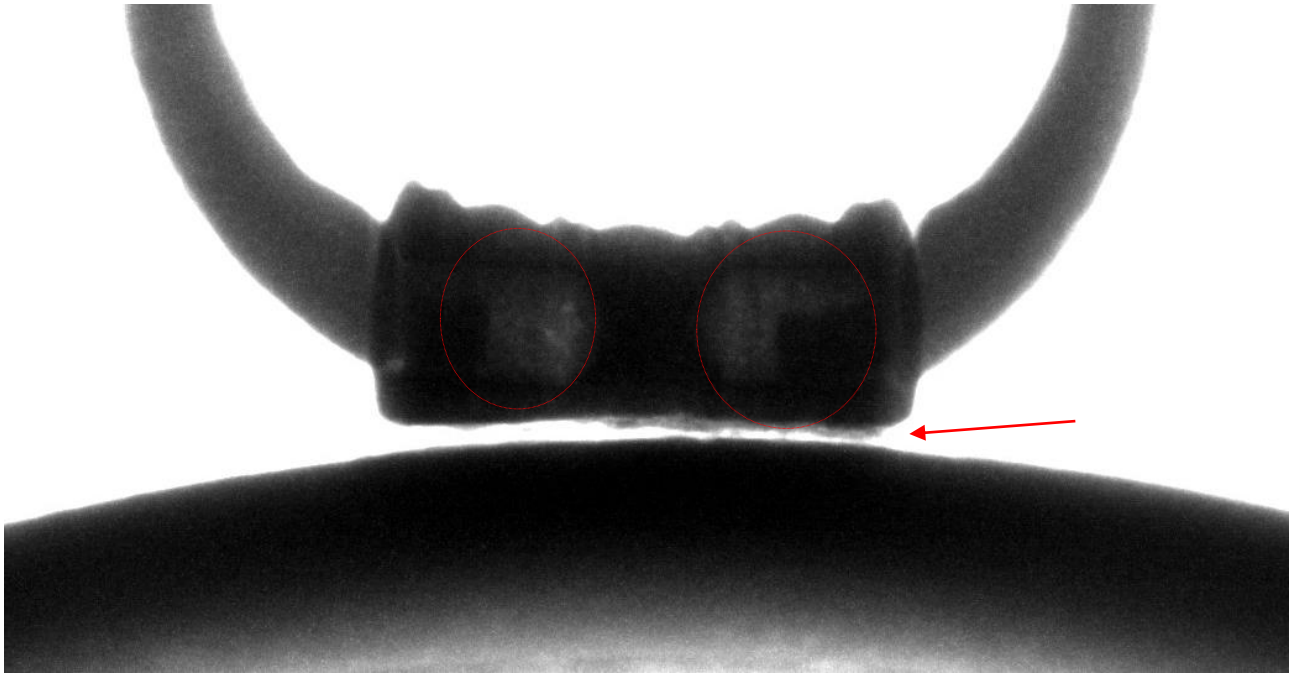

Figure 4.5.18: radiography of the top of n. 919 mirror

Figure 4.5.19b shows a greyscale histogram acquired along the yellow line in radiography of n. 919 mirror in figure 4.2.11a. The histogram shown how the X-ray absorb is max on the centre and is min on the edge of the bronze disc. Therefore, the disc thickness is maximum on the centre and is minimum on the edge.

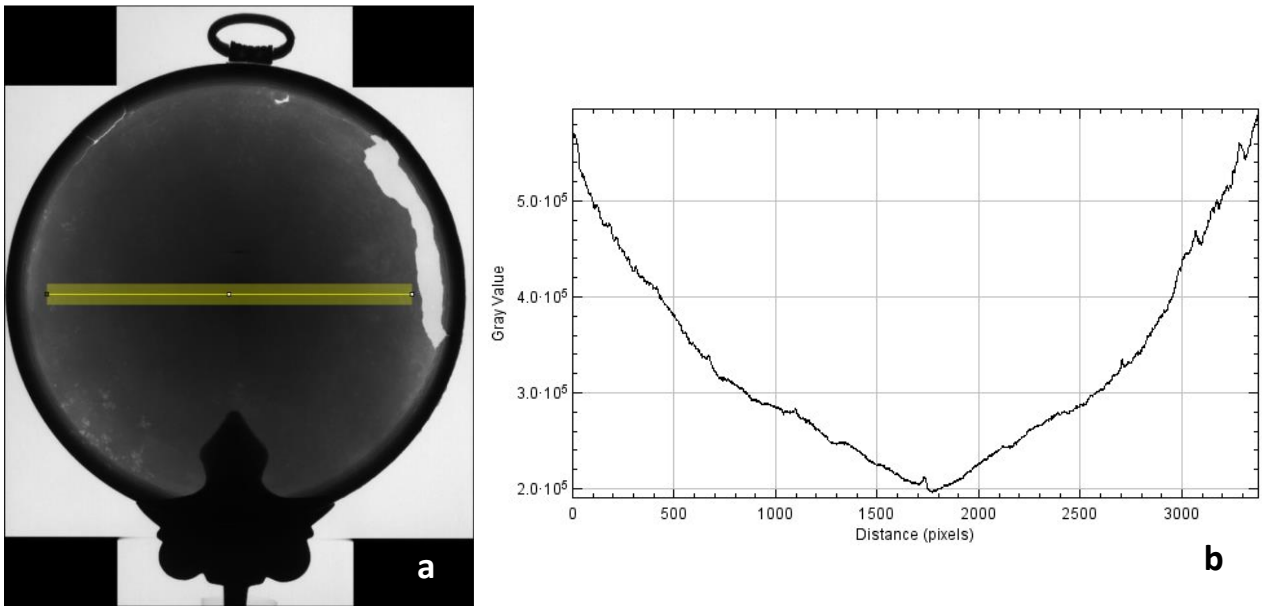

Figure 4.5.19: Greyscale histogram (b) acquired along the yellow line in radiography (a) of n. 919 mirror

Figure 4.5.20a shows a radiography of n. 916 mirror, while figure 4.5.20b shows a magnification of previous image in which the corrosion phenomenon as called pitting is visible. [103]–[106]

Figure 4.5.21b shows a greyscale histogram acquired along the yellow line in radiography of n. 916 mirror in figure 4.2.21a. The histogram shows how the X-ray absorb is max on the centre and is min on the edge of the bronze disc. Therefore, the disc thickness is maximum on the centre, and is minimum on the edge.

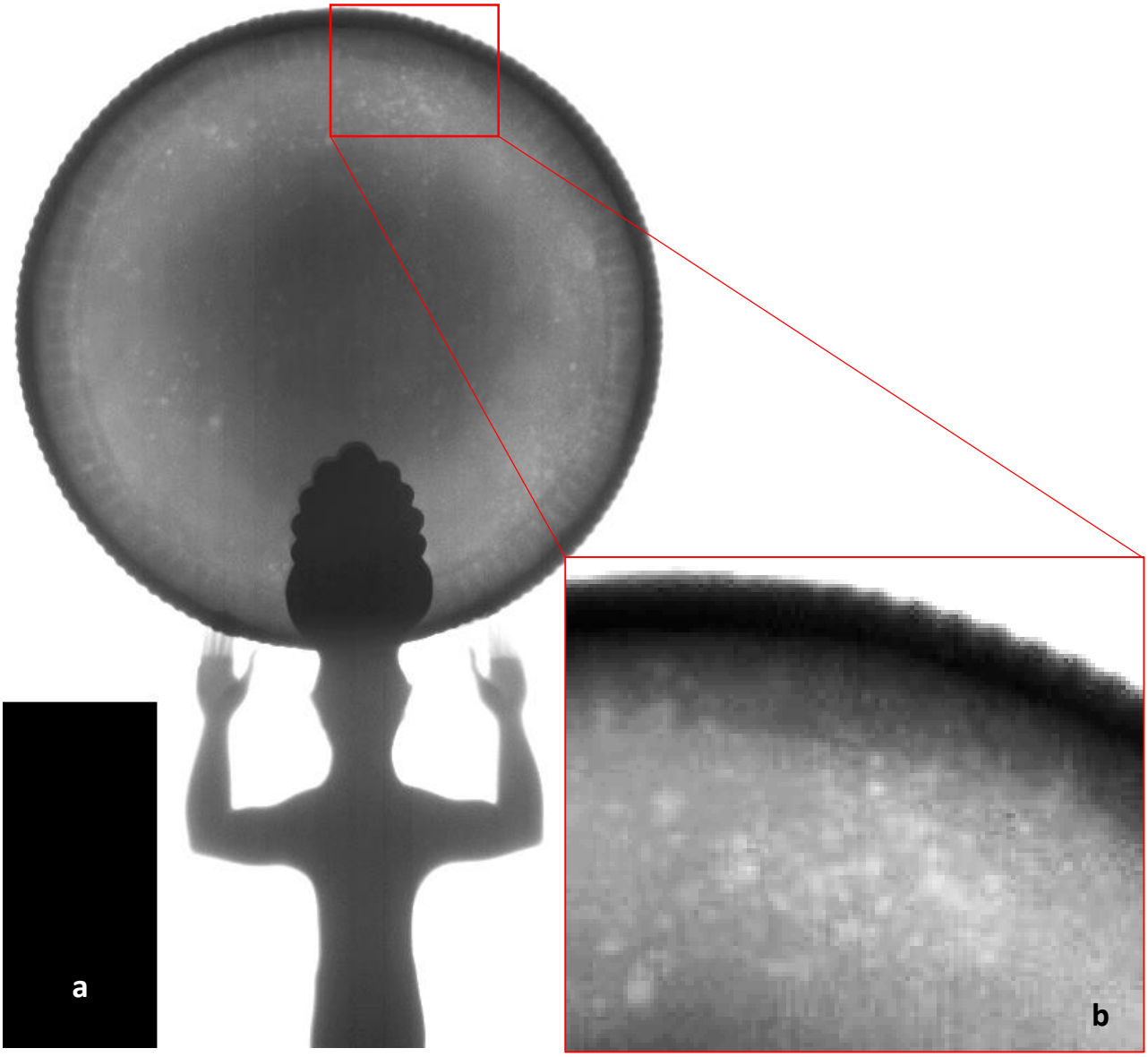

Figure 4.5.20: X-ray radiography of n. 916 mirror (a); magnification of previous radiography image in which the pitting phenomenon is visible (b)

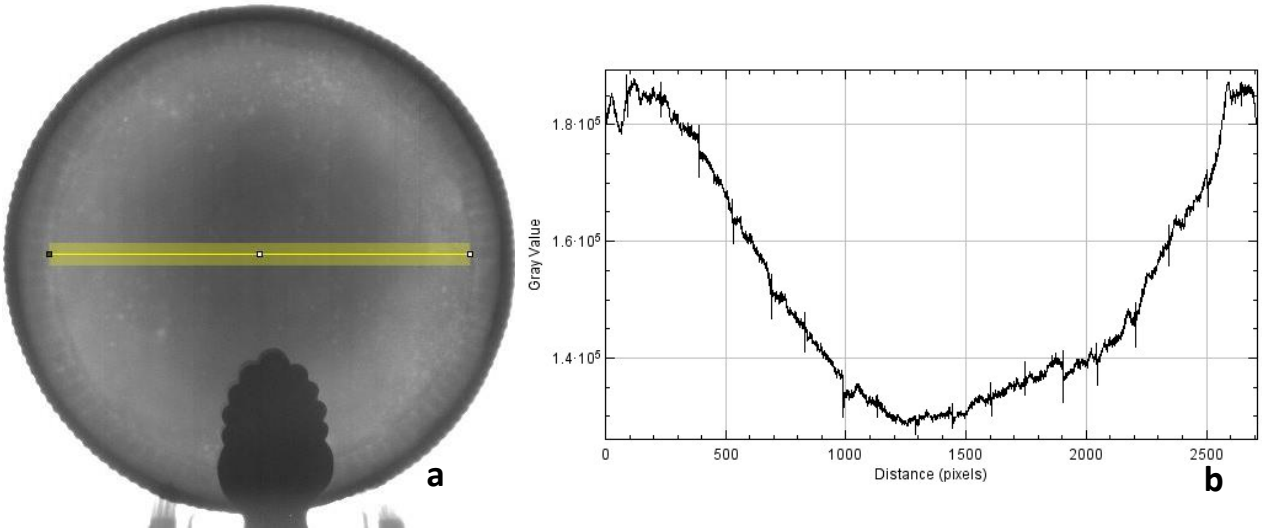

Figure 4.5.21: Greyscale histogram (b) acquired along the yellow line in radiography (a) of n. 916 mirror

Figure 4.5.22 shows a radiography of n. 916 mirror in which a corrosion phenomenon also called pitting is visible [113-116]. In the same figure we can see many gaps and many fragments glued together, while the red circle shows a lead filling.

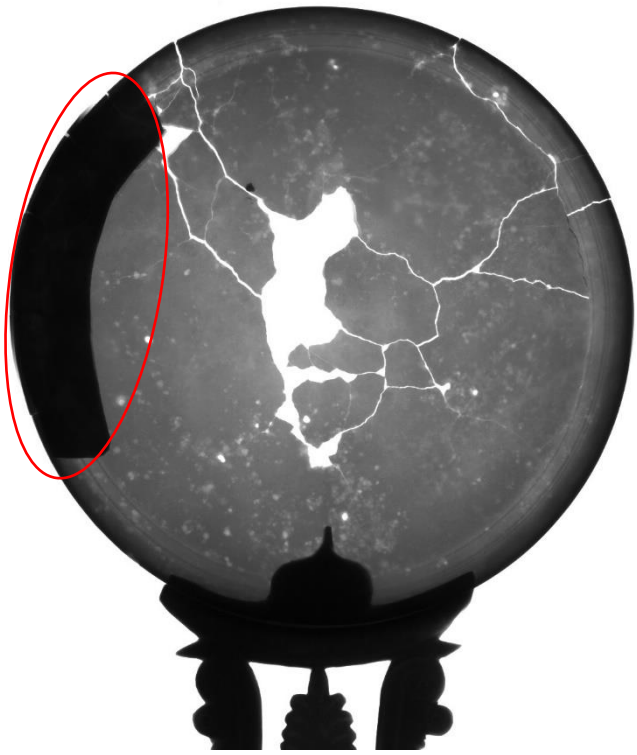

Figure 4.5.22: Radiography of n. 916 mirror in which is visible the pitting phenomenon, many gaps and many fragments glued together and a lead filling in the red circle

4.5.5. Conclusion

The 12 Magno-Greeck bronze mirrors conserved at the National Archaeological Museum of Locri Epizefiri have been studied by completely non-invasive and non-destructive complementary physical methodologies means, as X-ray microtomography, XRF portable spectroscopy and photographic investigation under UV light. In addition, 3D reconstructions by automated photogrammetry were carried out on each bronze mirror.

These methodologies have allowed to characterize the constituent materials, to investigate their preservation status and to have useful information to understand their construction methods.

All circular bronze discs are made by a binary Cu-Sn bronze alloy, which percentage concentration values are described below:

- n. 918: Cu 97.04% and Sn 2.19%;
- n. 688 Cu 88.13% and Sn 9.31%;
- n. 685 Cu 85.00% and Sn 12.40%;
- n. 877 Cu 83.03% and Sn 15.08%;
- n. 916 Cu 81.01% and Sn 17.41%;
- n. 871 Cu 75.66% and Sn 23.43%;
- n. 919 Cu 69.75% and Sn 26.20%.

The bronze supports are made by a ternary Cu-Sn-Pb alloy, which percentage concentration values are described below:

- n. 915: Cu 83.30%, Sn 10.02% and Pb 4.54;
- n. 1765: Cu 82.11%, Sn 6.94% and Pb 5.70%;
- n. 142050 (black surface): Cu 81.8%; Sn 5.46% and Pb 8.25%;
- n. 911: Cu 61.03%, Sn 10.20% and Pb 27.22;
- n. 912: Cu 35.30%, Sn 30.42% and Pb 33.25%.

The last two analysis present the highest percentage of lead content, it is due probably to superficial decuprification phenomenon. [82]–[84] The bronze discs analysed by X-ray microtomography displayed pitting corrosion phenomenon and their shape is concave with max thickness in the centre. Moreover, they have residue and trace of older restoration.

REFERENCES

[1] E. C. Wells, “Archaeometry: Definition,” in *Encyclopedia of Global Archaeology*, New York, NY: Springer New York, 2014, pp. 468–470.

[2] B. J. Louis, *The Modern Museum, in D. Bradley and D. Creagh, Physical techniques in the study of art, archaeology and cultural heritage*. 2006.

[3] N. Bohr, “I. On the constitution of atoms and molecules,” *London, Edinburgh, Dublin Philos. Mag. J. Sci.*, vol. 26, no. 151, pp. 1–25, Jul. 1913, doi: 10.1080/14786441308634955.

[4] J. A. Seibert, “Part 1: Basic principles of x-ray production,” *J Nucl Med Technol*, vol. 32, no. 3, pp. 139–47, 2004.

[5] E. M. A. Hussen, *Radiation Mechanics. Principles and Practice*, First. Elsevier, 2007.

[6] R. Hanke, T. Fuchs, M. Salamon, and S. Zabler, *X-ray Microtomography for Materials Characterization*. Elsevier Ltd, 2016.

[7] A. S. David Attwood, *X-rays and extreme ultraviolet radiation.Principles and applications*, Second. Cambridge: Cambridge University Press, 2017.

[8] VV.AA., *Computed tomography: Instrumentation*. Vienna: International Atomic Energy Agency, 2014.

[9] M.-G. Barthés-Labrousse, “The Auger Effect,” *Microsc. Microanal. Microstruct.*, vol. 6, no. 3, pp. 253–262, 1995, doi: 10.1051/mmm:1995122.

[10] G. N. Hounsfield, “Computerized transverse axial scanning (tomography): Part 1. Description of system,” *Br. J. Radiol.*, vol. 46, no. 552, pp. 1016–1022, Dec. 1973, doi: 10.1259/0007-1285-46-552-1016.

[11] R. Hanke, T. Fuchs, and N. Uhlmann, “X-ray based methods for non-destructive testing and material characterization,” *Nucl. Instruments Methods Phys. Res. Sect. A Accel. Spectrometers, Detect. Assoc. Equip.*, vol. 591, no. 1, pp. 14–18, Jun. 2008, doi: 10.1016/j.nima.2008.03.016.

[12] N. Applbaum and Y. H. Applbaum, “The Use of Medical Computed Tomography (CT) Imaging in the Study of Ceramic and Clay Archaeological Artifacts from the Ancient Near East,” in *X-rays for Archaeology*, Berlin/Heidelberg: Springer-Verlag, 2005, pp. 231–245.

[13] F. Casali, “Chapter 2 X-ray and neutron digital radiography and computed tomography for cultural heritage,” *Phys. Tech. Study Art, Archaeol. Cult. Herit.*, vol. 1, no. C, pp. 41–123, Jan. 2006, doi: 10.1016/S1871-1731(06)80003-5.

[14] R. G. Agostino *et al.*, “Microtomographic studies as a tool in the identification of a new ceramic class: The metal-imitating pottery as grave goods among Brettians and Lucanians,” *Microchem. J.*, vol. 126, pp. 138–148, May 2016, doi: 10.1016/j.microc.2015.12.007.

[15] M. P. Morigi, F. Casali, M. Bettuzzi, R. Brancaccio, and V. D’Errico, “Application of X-ray Computed Tomography to Cultural Heritage diagnostics,” *Appl. Phys. A*, vol. 100, no. 3, pp. 653–661, Sep. 2010, doi: 10.1007/s00339-010-5648-6.

[16] M. S. A.C. Kak, *Principles of Computerized Tomographic Imaging*. New York, NY: IEEE Press, 1988.

[17] S. R. Stock, *MicroComputed Tomography*. Florida: CRC Press, 2008.

[18] E. N. Landis and D. T. Keane, “X-ray microtomography,” *Mater. Charact.*, vol. 61, no. 12, pp. 1305–1316, Dec. 2010, doi: 10.1016/j.matchar.2010.09.012.

[19] J. Baruchel, J.-Y. Buffière, and E. Maire, *X-Ray tomography in material science*. Hermès Science Publications, 2000.

[20] B. S. A. Tatone and G. Grasselli, “Characterization of the effect of normal load on the discontinuity morphology in direct shear specimens using X-ray micro-CT,” *Acta Geotech.*, vol. 10, no. 1, pp. 31–54, 2015, doi: 10.1007/s11440-014-0320-5.

[21] S. Pacilè and G. Tromba, “Introduction to X-Ray Micro-tomography,” Elsevier, 2018, pp. 19–39.

[22] F. Kharfi, “Mathematics and Physics of Computed Tomography (CT): Demonstrations and Practical Examples,” in *Imaging and Radioanalytical Techniques in Interdisciplinary Research - Fundamentals and Cutting Edge Applications*, InTech, 2013.

[23] S. C. Mayo, A. W. Stevenson, and S. W. Wilkins, “In-Line Phase-Contrast X-ray Imaging and Tomography for Materials Science,” *Materials (Basel).*, vol. 5, no. 12, pp. 937–965, May 2012, doi: 10.3390/ma5050937.

[24] T. Weitkamp, D. Haas, D. Wegrzynek, and A. Rack, “ANKAphase : software for single-distance phase retrieval from inline X-ray phase-contrast radiographs,” *J. Synchrotron Radiat.*, vol. 18, no. 4, pp. 617–629, Jul. 2011, doi: 10.1107/S0909049511002895.

[25] P. Pietsch and V. Wood, “X-Ray Tomography for Lithium Ion Battery Research: A Practical Guide,” *Annu. Rev. Mater. Res.*, vol. 47, no. 1, pp. 451–479, Jul. 2017, doi: 10.1146/annurev-matsci-070616-123957.

[26] C. A. Carlsson, G. R. Davis, and F. S. L. Wong, “Physics in Medicine & Biology Related content Cone-beam X-ray microtomography of small specimens,” 1994.

[27] H. Turbell, “Cone-Beam Reconstruction Using Filtered Backproject,” Linkopings, 2001.

[28] K. Yang, A. L. C. Kwan, D. F. Miller, and J. M. Boone, “A geometric calibration method for cone beam CT systems,” *Med. Phys.*, vol. 33, no. 6Part1, pp. 1695–1706, May 2006, doi: 10.1118/1.2198187.

[29] R. Chityala, K. R. Hoffmann, S. Rudin, and D. R. Bednarek, “Region of interest (ROI) computed tomography (CT): comparison with full field of view (FFOV) and truncated CT for a human head phantom,” *Soc. Photo-Optical Instrum. Eng.*, vol. 5745, no. 1, pp. 583–590, 2005, doi: 10.1117/12.595430.

[30] W. R. Hendee, *Cone Beam Computed Tomography*. Florida: CRC Press, 2014.

[31] J. G. Kim, S. O. Jin, M. H. Cho, and S. Y. Lee, “Inter-plane artifact suppression in tomosynthesis using 3D CT image data,” *Biomed. Eng. Online*, vol. 10, no. 1, p. 106, 2011, doi: 10.1186/1475-925X-10-106.

[32] F. E. Boas and D. Fleischmann, “CT artifacts: Causes and reduction techniques,” *Imaging Med.*, vol. 4, no. 2, pp. 229–240, 2012, doi: 10.2217/iim.12.13.

[33] S. Krimmel, “Limited view angle tomography for single material objects in non-destructive testing with X-rays,” Technischen Universitat Munchen, 2006.

[34] W. Zhao and J. A. Rowlands, “Digital radiology using active matrix readout of amorphous selenium: Theoretical analysis of detective quantum efficiency,” *Med. Phys.*, vol. 24, no. 12, pp. 1819–1833, Dec. 1997, doi: 10.1118/1.598097.

[35] W. Zhao, D. C. Hunt, K. Tanioka, and J. A. Rowlands, “Amorphous selenium flat panel detectors for medical applications,” *Nucl. Instruments Methods Phys. Res. Sect. A Accel. Spectrometers, Detect. Assoc. Equip.*, vol. 549, no. 1–3, pp. 205–209, Sep. 2005, doi: 10.1016/j.nima.2005.04.053.

[36] K. Kump, P. Grantors, F. Pla, and P. Gobert, “Digital X-ray detector technology,” *RBM-News*, vol. 20, no. 9, pp. 221–226, Dec. 1998, doi: 10.1016/S0222-0776(99)80006-6.

[37] E. Kotter and M. Langer, “Digital radiography with large-area flat-panel detectors,” *Eur. Radiol.*, vol. 12, no. 10, pp. 2562–2570, Oct. 2002, doi: 10.1007/s00330-002-1350-1.

[38] G. C. O.W.E. Morrish, S.J. Yates, F.I. McKiddie, P.H. Jarritt, K.E. Goldstone, A.C. Fairhead, T.A. Whittingham, E.A. Moore, *Physics for diagnostic radiology*. Florida: CRC Press, 2012.

[39] V. Veikutis *et al.*, “Artifacts in computer tomography imaging: How it can really affect diagnostic image quality and confuse clinical diagnosis?,” *J. Vibroengineering*, vol. 17, no. 2, pp. 995–1003, 2015.

[40] Y.-W. Chen, G. Duan, A. Fujita, K. Hirooka, and Y. Ueno, “Ring artifacts reduction in cone-beam CT images based on independent component analysis,” in *2009 IEEE Intrumentation and Measurement Technology Conference*, May 2009, pp. 1734–1737, doi: 10.1109/IMTC.2009.5168737.

[41] T. M. Buzug, *Computed Tomography: from Photon Statistics to Modern Cone-Beam CT*. Berlin: Springer, 2008.

[42] R. Schulze *et al.*, “Artefacts in CBCT: a review,” *Dentomaxillofacial Radiol.*, vol. 40, no. 5, pp. 265–273, Jul.

2011, doi: 10.1259/dmfr/30642039.

[43] M. 1986- Krenkel and Universitätsverlag Göttingen, *Cone-beam x-ray phase-contrast tomography for the observation of single cells in whole organs*. .

[44] G. L. Zeng, *Medical Image Reconstruction*. Berlin, Heidelberg: Springer Berlin Heidelberg, 2010.

[45] VV.AA., *Handbook of X-Ray Spectrometry*, Second. New York: Marcel Dekker, 2002.

[46] H. W. Burkhard Beckhoff, Birgit Kanngießer, Norbert Langhoff, Reiner Wedell, *Handbook of Practical X-Ray Fluorescence Analysis*. Springer Science & Business Media, 2007.

[47] K. Janssens *et al.*, "Use of microscopic XRF for non-destructive analysis in art and archaeometry," *X-Ray Spectrom.*, vol. 29, no. 1, pp. 73–91, Jan. 2000, doi: 10.1002/(SICI)1097-4539(200001/02)29:1<73::AID-XRS416>3.0.CO;2-M.

[48] A. Longoni *et al.*, "A portable XRF spectrometer for non-destructive analyses in archaeometry," *Nucl. Instruments Methods Phys. Res. Sect. A Accel. Spectrometers, Detect. Assoc. Equip.*, vol. 409, no. 1–3, pp. 407–409, May 1998, doi: 10.1016/S0168-9002(98)00113-2.

[49] T. P. A.G. Karydas, X. Brecoulaki, Th. Pantazis, E. Aloupi, V. Argyropoulos, D. Kotzamani, R. Bernard, Ch. Zarkadas, "Importance of in-situ EDXRF Measurements in the Preservation and Conservation of Materiale Culture," in *X-rays for Archaeology*, M. Uda, G. Demortier, and I. Nakai, Eds. Berlin/Heidelberg: Springer-Verlag, 2005, pp. 27–53.

[50] VV.AA., *In situ applications of x-ray fluorescence techniques*, no. September. Vienna, 2005.

[51] D. S. M. G. Gauglitz, *Handbook of Spectroscopy*. John Wiley & Sons, 2014.

[52] R. Cesareo, G. Ettore Gigante, and A. Castellano, "Thermoelectrically cooled semiconductor detectors for non-destructive analysis of works of art by means of energy dispersive X-ray fluorescence," *Nucl. Instruments Methods Phys. Res. Sect. A Accel. Spectrometers, Detect. Assoc. Equip.*, vol. 428, no. 1, pp. 171–181, Jun. 1999, doi: 10.1016/S0168-9002(99)00004-2.

[53] N. Grassi, "Rivelatori a deriva di silicio per spettroscopia X: studio del possibile utilizzo in misure PIXE con fascio esterno," University of Firenze, 2002.

[54] E. Gatti and P. Rehak, "Semiconductor drift chamber - An application of a novel charge transport scheme," *Nucl. Instruments Methods Phys. Res.*, vol. 225, no. 3, pp. 608–614, Sep. 1984, doi: 10.1016/0167-5087(84)90113-3.

[55] P. Lechner *et al.*, "Silicon Drift Detectors for high count rate X-ray spectroscopy at room temperature," *Nucl. Instruments Methods Phys. Res. Sect. A Accel. Spectrometers, Detect. Assoc. Equip.*, vol. 458, no. 1–2, pp. 281–287, Feb. 2001, doi: 10.1016/S0168-9002(00)00872-X.

[56] C. and G. R. L. Fernard, *Quantitative X-Ray fluorescence analysis*. Wiley, 1995.

[57] G. R. Lachance, "Correction procedures using influence coefficients in X-ray fluorescence spectrometry," *Spectrochimica Acta Part B: Atomic Spectroscopy*, vol. 48, no. 3. Elsevier, pp. 343–357, Feb. 01, 1993, doi: 10.1016/0584-8547(93)80040-2.

[58] A. Markowicz, "An overview of quantification methods in energy-dispersive X-ray fluorescence analysis," 2011.

[59] P. Brouwer, *Theory of XRF*. Almelo: PANalytical, 2010.

[60] K. Danzer, *Analytical Chemistry: Theoretical and Metrological Fundamentals*. Springer Science & Business Media, 2007.

[61] B. A. R. V. Johan L. de Vries, "Quantification of Infinitely Thick Specimens by XRF Analysis," in *Handbook of X-Ray Spectrometry*, A. M. Rene Van Grieken, Ed. CRC Press, 2001, p. 1016.

[62] R. M. Rousseau, "Concept of the influence coefficient," *Rigaku J.*, vol. 18, no. 1, pp. 8–21, 2001, doi: 10.1007/978-1-4757-9110-5.

[63] J. W. Criss and L. S. Birks, "Calculation Methods for Fluorescent X-Ray Spectrometry: Empirical Coefficients vs. Fundamental Parameters," *Anal. Chem.*, vol. 40, no. 7, pp. 1080–1086, 1968, doi: 10.1021/ac60263a023.

[64] J. Schindelin *et al.*, “Fiji: An open-source platform for biological-image analysis,” *Nat. Methods*, vol. 9, no. 7, pp. 676–682, 2012, doi: 10.1038/nmeth.2019.

[65] B. E., “Nummi Pelliculati-Considerazioni sull’argento suberato della repubblica romana,” *Riv. Ital. di Numis. e Sci. Affin.*, vol. XIII, pp. 5–31, 1965.

[66] G. M. Ingo, S. Balbi, T. De Caro, I. Fragalà, C. Riccucci, and G. Bultrini, “Microchemical investigation of Greek and Roman silver and gold plated coins: Coating techniques and corrosion mechanisms,” *Appl. Phys. A Mater. Sci. Process.*, vol. 83, no. 4, pp. 623–629, 2006, doi: 10.1007/s00339-006-3536-x.

[67] L.H. Hope, “Surface-Silvered Ancient Coins,” in *Methods of chemical and metallurgical investigation of ancient coinage*, E. T. & Hall and D. M. Metcalf, Eds. London: Royal Numismatic Society, 1972, pp. 261–278.

[68] L. H. Hope, “THE ARGENTIFEROUS BRONZE ALLOYS OF THE LARGE TETRARCHIC FOLLES OF A . D .,” *Numis. Chron.*, vol. 8, pp. 115–149, 1968.

[69] K. Anheuser and J. P. Northover, “Silver plating on Roman and Celtic coins from Britain: a technical study,” *Br. Numis. journal, Incl. Proc. Br. Numis. Soc.*, vol. 64, pp. 22–32, 1994.

[70] S. La Niece, “Silvering,” in *Metal plating and patination: cultural, technical and historical developments*, S. L. N. & P. Craddock, Ed. Oxford: Butterworth-Heinemann, 1993, pp. 201–210.

[71] E. P. Campbell, W. & Robinson, “Greek and Roman Plated Coins,” *Am. Numis. Soc.*, 1993.

[72] A. Deraisme, L. Beck, F. Pilon, and J.-N. Barrandon, “A STUDY OF THE SILVERING PROCESS OF THE GALLO-ROMAN COINS FORGED DURING THE THIRD CENTURY AD*,” 2006.

[73] P. T. Keyser, “Greco-Roman alchemy and coins of imitation silver,” *Am. J. Numis.*, vol. 7, pp. 209–234, 1995.

[74] C. Vlachou, J. G. McDonnell, and R. C. Janaway, “Experimental investigation of silvering in late Roman coinage,” *MRS Proc.*, vol. 712, p. II9.2, Mar. 2002, doi: 10.1557/PROC-712-II9.2.

[75] P. A., “Le monete,” in *Museo dei Bretti e degli Enotri - Catalogo dell’esposizione*, C. M. & V. A., Ed. Soveria Mannelli: Rubbettino, 2014, pp. 649–669.

[76] U. Zwicker, A. Oddy, and S. La Niece, “Roman techniques of manufacturing silver-plated coins,” in *Metal Plating and Patination*, Elsevier, 1993, pp. 223–246.

[77] B. L. Henke, E. M. Gullikson, and J. C. Davis, “X-ray interactions: Photoabsorption, scattering, transmission, and reflection at E = 50-30, 000 eV, Z = 1-92,” *At. Data Nucl. Data Tables*, vol. 54, no. 2, pp. 181–342, Jul. 1993, doi: 10.1006/adnd.1993.1013.

[78] W. H. Carter, G. F. & Carter, “Chemical Analysis of a Plautia Denarius,” *Seaby Coin Medal Bull.*, pp. 58–60, 1965.

[79] A. W. Pense, “The decline and fall of the roman denarius,” *Mater. Charact.*, vol. 29, no. 2, pp. 213–222, Sep. 1992, doi: 10.1016/1044-5803(92)90116-Y.

[80] N. Mittica, G. & Perrone, “Espressioni votive e rituali nel Santuario arcaico di Timpone della Motta,” in *Francavilla Marittima un patrimonio ricontestualizzato*, G. Mittica, Ed. Vibo Valentia: Adhoc Edizioni, 2019, pp. 237–263.

[81] A. J. Nijboer, “From household production to workshops Workshops. Archaeological Evidence for Economic Transformation, Pre-monetary Exchange and Urbanisation in Central Italy from 800 to 400 BC.,” University of Groningen, 1998.

[82] L. Robbiola, J. M. Blengino, and C. Fiaud, “Morphology and mechanisms of formation of natural patinas on archaeological Cu-Sn alloys,” *Corros. Sci.*, vol. 40, no. 12, pp. 2083–2111, Dec. 1998, doi: 10.1016/S0010-938X(98)00096-1.

[83] E. Figueiredo, P. Valério, M. F. Araújo, and J. C. Senna-Martinez, “Micro-EDXRF surface analyses of a bronze spear head: Lead content in metal and corrosion layers,” *Nucl. Instruments Methods Phys. Res. Sect. A Accel. Spectrometers, Detect. Assoc. Equip.*, vol. 580, no. 1 SPEC. ISS., pp. 725–727, Sep. 2007, doi: 10.1016/j.nima.2007.05.135.

[84] M. Matteini, M., Moles, A., & Nepoti, “Caratterizzazione dei prodotti di alterazione di superficie mediante spettrofotometria IR,” *OPD Restauro*, vol. 3, pp. 36–39, 1991.

[85] L. Robbiola *et al.*, “New insight into the nature and properties of pale green surfaces of outdoor bronze monuments,” *Appl. Phys. A Mater. Sci. Process.*, vol. 92, no. 1, pp. 161–169, 2008, doi: 10.1007/s00339-008-4468-4.

[86] M. C. Bernard and S. Joiret, “Understanding corrosion of ancient metals for the conservation of cultural heritage,” *Electrochim. Acta*, vol. 54, no. 22, pp. 5199–5205, Sep. 2009, doi: 10.1016/j.electacta.2009.01.036.

[87] L. Robbiola and R. Portier, “A global approach to the authentication of ancient bronzes based on the characterization of the alloy-patina-environment system,” *J. Cult. Herit.*, vol. 7, no. 1, pp. 1–12, Jan. 2006, doi: 10.1016/j.culher.2005.11.001.

[88] G. M. Ingo, T. de Caro, C. Riccucci, and S. Khosroff, “Uncommon corrosion phenomena of archaeological bronze alloys,” *Appl. Phys. A*, vol. 83, no. 4, pp. 581–588, Jun. 2006, doi: 10.1007/s00339-006-3534-z.

[89] L. Campanella, O. C. Alessandri, M. Ferretti, and S. H. Plattner, “The effect of tin on dezincification of archaeological copper alloys,” *Corros. Sci.*, vol. 51, no. 9, pp. 2183–2191, Sep. 2009, doi: 10.1016/j.corsci.2009.05.047.

[90] I. Constantinides, A. Adriaens, and F. Adams, “Surface characterization of artificial corrosion layers on copper alloy reference materials,” *Appl. Surf. Sci.*, vol. 189, no. 1–2, pp. 90–101, Apr. 2002, doi: 10.1016/S0169-4332(02)00005-3.

[91] M. Serghini-Idrissi *et al.*, “Electrochemical and spectroscopic characterizations of patinas formed on an archaeological bronze coin,” *Electrochim. Acta*, vol. 50, no. 24, pp. 4699–4709, Aug. 2005, doi: 10.1016/j.electacta.2005.01.050.

[92] J. Boardman, “Sources and Models,” in *Greek Sculpture. Function, Materials and Techniques in the Archaic and Classical Periods*, Olga Palagia, Ed. Cambridge: University Press, 2006, pp. 1–31.

[93] C. Mattusch, “Archaic and Classical Bronzes,” in *Greek Sculpture. Function, Materials and Techniques in the Archaic and Classical Periods*, Olga Palagia, Ed. Cambridge: University Press, 2006, pp. 208–242.

[94] S. S. & M. Miccio, “La tecnica esecutiva,” *Minerva*, pp. 175–190, 2008.

[95] M. Sannibale, “Tra età classica ed ellenismo: la tecnica dei grandi bronzi e i suoi riflessi nella produzione minore,” in *I Grandi Bronzi Antichi. Le fonderie e le tecniche di lavorazione dall’età arcaica al Rinascimento*, E. Formigli, Ed. Siena: NIE, 1999, pp. 113–146.

[96] A. P., *Le leghe bronzee e le loro applicazioni*. Trento, 2003.

[97] J. Henderson, “A. MARK POLLARD & CARL HERON. Archaeological chemistry. xvi+375 pages, 105 illustrations, 19 tables. 1996. Cambridge: The Royal Society of Chemistry; 0-85404-523-6 paperback £22.50 & $39.,” *Antiquity*, vol. 71, no. 272, pp. 497–498, Jun. 1997, doi: 10.1017/S0003598X00085239.

[98] M. M. & M. Arcangelo, *La Chimica nel Restauro*. Firenze: Nardini Editore, 1989.

[99] J. B. Lambert, *Traces Of The Past: Unraveling The Secrets Of Archaeology Through Chemistry*. Helix Books, 1997.

[100] J. P. RAMA, *Le bronze d’art et ses technique*. Dourdan: Edition Vial, 1995.

[101] T. K. Andrews, *Bronzecasting at Geometric period Olympia and early Greek metals sources*. Brandeis University, 1994.

[102] S. Klein and A. Hauptmann, “Iron Age leaded tin bronzes from Khirbet edh-Dharih, Jordan,” *J. Archaeol. Sci.*, vol. 26, no. 8, pp. 1075–1082, Aug. 1999, doi: 10.1006/jasc.1999.0412.

[103] F. M. G. Bianchi, “Corrosione e protezione dei metalli,” *Assoc. Ital. di Metall.*, pp. 10–12, 2005.

[104] P. Pedeferri, *Corrosione e Protezione dei Materiali Metallici*. Milano: Clup, 1978.

[105] R. W. Uhlig, H H, & Revie, *Corrosion and corrosion control. Third edition*. United States.

[106] T. K. Ross, “Introduction to corrosion prevention and control for engineers,” *Corros. Sci.*, vol. 17, no. 10, pp. 857–858, Jan. 1977, doi: 10.1016/0010-938X(77)90088-9.